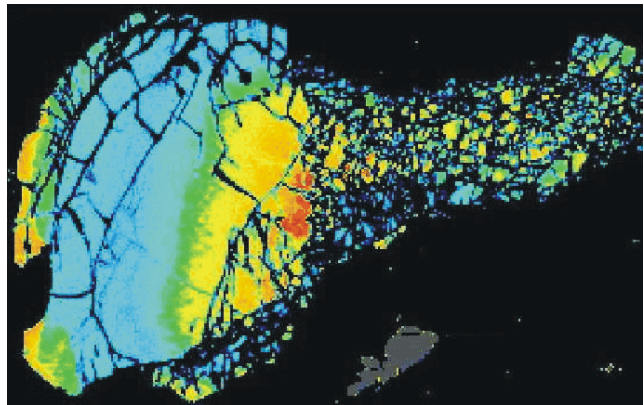


Microstructural Criteria for Synseismic Loading and Postseismic Creep in the Uppermost Plastosphere

An Example From the Sesia Zone, Western Alps



Thesis accepted by the faculty of Geoscience at the Ruhr-University Bochum, Germany, in fulfilment of the requirements for the degree of a Dr. rer. nat.

Claudia A. Trepmann

Bochum, May 2002

Microstructural Criteria for Synseismic Loading and Postseismic Creep in the Uppermost Plastosphere

An Example From the Sesia Zone, Western Alps

Thesis accepted by the faculty of
Geoscience at the Ruhr-University
Bochum, Germany, in fulfilment of the
requirements for the degree of a
Dr. rer. nat.

Claudia A. Trepmann

Day of examination:

7th of May 2002

Examination committee:

Prof. Dr. B. Stöckhert

Prof. Dr. J. Renner

Prof. Dr. S. Chakraborty

Table of contents

Abstract	1
1. Introduction	3
1.1. Problem definition and scope	3
1.2. Theoretical background	3
1.2.1. The brittle-plastic transition (BPT)	3
1.2.2. The effect of seismic activity on the BPT	5
1.3 Present aims	7
1.4 Organisation of the thesis	8
2. Methods	9
2.1. Introduction	9
2.2. Sampling	9
2.3. Optical microscopy and universal stage	9
2.4. Scanning electron microscopy (SEM)	9
2.4.1. Secondary electron (SE)-imaging	10
2.4.2. Orientation contrast (OC) -imaging and electron backscatter diffraction (EBSD)	10
2.4.3. Energy dispersive x-ray (EDX)- analysis	11
2.5. Electron microprobe (EMP)	11
2.6. Cathodoluminescence microscopy	12
2.7. Transmission electron microscopy (TEM)	12
2.8. Fourier transformed infrared (FTIR) spectroscopy	13
3. Geological setting	14
3.1. Introduction	14
3.2. Geological overview	14
3.3. Geological setting of the investigated areas	15
4. High-strain zones	16
4.1. Introduction	16
4.2. Mylonites	17
4.3. Ultramylonites	19
4.4. Pseudotachylytes	21
4.5. Discussion and conclusion	23
5. Mechanical twinning of jadeite	25
5.1. Introduction	25
5.2. Mechanical twinning of clinopyroxene	25
5.3. Sample description	27
5.4. Analytical results	30
5.4.1. Orientation distribution of jadeite crystals	30
5.4.2. Orientation of the principal stress directions	31
5.4.3. Paleopiezometry	32
5.5. Discussion	33
5.6. Conclusions	34
6. Cataclastic deformation of garnet	36
6.1. Introduction	36
6.2. Sample description	37

6.3. Garnet microstructure	37
6.3.1. Fracture pattern and geometry of fragmented garnet	39
6.3.2. Crystallographic orientation	41
6.4. Discussion	44
6.4.1. Implications of the microstructural record	44
6.4.2. Conditions at initial fragmentation	45
6.4.3. Tectonic environment and inferred boundary conditions	46
6.5. Conclusions	47
7. Plasticity and creep of quartz	49
7.1. Introduction	49
7.2. Sampling	49
7.3. Microstructural record of quartz	50
7.3.1. Type A microstructure	50
7.3.2. Type B microstructure	52
7.3.3. Type C microstructure	55
7.3.4. Type D microstructure	57
7.3.5. Type and concentration of water and water-related defects	60
7.4. Discussion	60
7.4.1. Microstructures indicative of microcracking	60
7.4.2. Microstructures indicative of low-temperature plasticity	61
7.4.3. Microstructures indicative of recovery and recrystallisation	63
7.4.4. Crystallographic preferred orientation	64
7.4.5. Microstructures indicative of grain growth	64
7.4.6. Paleopiezometers	65
7.4.7. Progressive evolution of the quartz microfabrics during post-seismic stress relaxation	67
7.5. Conclusions	70
8. Branching quartz veins	71
8.1. Introduction	71
8.2. Mesoscopic structures	71
8.3. Microstructures	73
8.4. Discussion and conclusion	73
9. General discussion and conclusions	74
9.1. Introduction	74
9.2. Microstructural criteria for syn- and postseismic deformation	74
9.3. Time and length scales during deformation	75
9.4. Tectonic boundary conditions	76
9.5. Earthquake recurrence	76
9.6. Conclusions	77
10. References	78
Appendix A: List of samples	88
Appendix B: EMP analyses	89
Acknowledgements	92
Curriculum vitae	93

Abstract

Major earthquakes in the brittle upper crust are expected to cause rapid non steady-state plastic flow at high differential stress and strain rate beneath the brittle-plastic transition with fluctuations of pore fluid pressure. The exhumed metamorphic rocks from the Sesia Zone, Western Alps, provide an example of a prominent microstructural record which is used in the present thesis to gain insight into synseismic loading and postseismic creep in the uppermost plastosphere related to earthquakes in the overlying schizosphere.

The microstructures suggest a complex interplay of different deformation processes in the rock-forming minerals. Jadeite crystals reveal mechanical twinning. The microstructural record of quartz is highly heterogeneous. Sub-basal deformation lamellae, arrays of elongate subgrains on the TEM-scale and healed microcracks indicate an early stage of glide-controlled deformation at high stresses accompanied by distributed brittle failure. Very fine-grained recrystallised aggregates with a pronounced crystallographic preferred orientation reflect intense plastic flow by dislocation creep. Locally, a foam microstructure indicates a final stage of static grain growth at low differential stress. The high-strength mineral garnet, which is embedded in a quartz matrix, underwent cataclastic deformation by initial fragmentation. Subsequent displacement of the fragments by sliding along the cracks is caused by the flow of the surrounding quartz matrix. Garnet fragments were finally slightly pulled apart with quartz and feldspar precipitated from the fluid phase in the open cracks.

The peak magnitude of differential stress achieved during synseismic loading probably exceeds 0.5 GPa, as indicated by the orientation distribution of mechanically twinned jadeite and the critical resolved shear stress for twinning. For this inferred peak stresses and given temperatures of about 300 to 350°C, initial strain rates on the order of 10^{-10}s^{-1} are predicted by available flow laws for dislocation creep of quartz. During subsequent relaxation the flow stress and the strain rates are rapidly decaying.

Branching quartz veins developed from open fissures reflect brittle failure, with subsequent plastic deformation and recrystallisation of the precipitated quartz. These fractures are interpreted to have propagated into the uppermost plastosphere during synseismic loading. Dilation and enhanced permeability are assumed to have caused a drop in pore fluid pressure to markedly sublithostatic values, which is a prerequisite for plastic deformation at extreme differential stress. Restoration of a near-lithostatic pore fluid pressure in the final stage of postseismic creep is reflected by opening and sealing of cracks in garnet.

The mesoscopic structures reflect a highly inhomogeneous strain field. Strain is concentrated in centimetre- to metre-scale zones (mylonites, ultramylonites, pseudotachylytes) and is remarkably low in the intervening rocks. The rather low amount of accumulated strain in most rocks during deformation at the inferred high differential stress and strain rate suggests a short duration of deformation with a very high rate of loading and relaxation.

These findings are consistent with short-term deformation by plastic and brittle mechanisms at temperatures of 300-350°C under high stresses and strain rates, with fluctuations of pore fluid pressure. The microstructures are thus proposed to reflect rapid, non steady-state plastic flow in the uppermost plastosphere caused by a major earthquake in the overlying schizosphere, comprising the following stages:

- (1) Fractures propagating downwards, causing a drop in pore fluid pressure.
- (2) Very high peak stress exceeding 0.5 GPa during synseismic loading;
at this stage deformation of quartz is glide-controlled and accompanied by micro-cracking. Fragmentation of garnet and mechanical twinning of jadeite take place simultaneously.
- (3) Stress relaxation, primarily controlled by power law creep of quartz.
- (4) Eventual restoration of a near-lithostatic pore fluid pressure.

The present study demonstrates the importance of non steady-state deformation, with significant fluctuations in stress and pore fluid pressure, contrary to conventional ideas of predominantly steady-state flow of rocks beneath the brittle-plastic transition.

1. Introduction

1.1. Problem definition and scope

The mechanical behaviour of the tectonically active Earth's crust in association with seismic activity is a matter of great interest in geoscience (e.g. Sibson, 1977, 1986; Scholz, 1990; Engelder, 1993; Yeats et al., 1997). Episodic aseismic creep following a major earthquake is assumed to accommodate a large part of tectonic plate motion, as recorded by Global Positioning System (GPS) (Heki et al., 1997; DeMets, 1997; Vergnolle et al., 2001; Pollitz et al., 2001). This is considered to be caused by postseismic slip at seismogenic depths and/or by flow in the uppermost plastic lower crust (e.g. Cohen, 1981; Rice and Gu, 1983; Sabadini et al., 1984; Tse and Rice, 1986; Ivins, 1996; Li and Rice, 1987; Schaff et al., 1998) due to short-term deformation at very high differential stress, high strain rate and fluctuations of pore fluid pressure (e.g. McCaig, 1988). Syn- and postseismic deformation in the upper plastosphere are poorly understood due to the lack of direct access and to insufficient resolution provided by geophysical techniques. However, specific microstructures formed under these conditions millions of years ago can be studied in rocks exposed today at the Earth's surface. Thus, the microstructural record of exhumed metamorphic rocks can reflect the presence or absence of ancient seismicity and provide insight into the processes within the uppermost plastosphere during and after present-day earthquakes. However, the only structures which have been considered so far to be diagnostic of paleoseismic zones are pseudotachylytes (e.g. Sibson, 1975) and only few studies in the geological literature emphasise the potential of the microstructural record of natural rocks in relation to seismic activity (O'Hara, 1990; Küster and Stöckhert, 1999; Daquan et al., 2000).

The peculiar microstructures of the exhumed metamorphic rocks from the Sesia Zone are assumed to reflect syn- and postseismic deformation in the uppermost plastosphere (Küster and Stöckhert, 1999). A detailed investigation of the microstructures provides further insight into the processes of loading and relaxation. The activated deformation mechanisms, the magnitudes of differential stress, the orientation of the stress field, and spatial heterogeneity are evaluated. The time scales of loading and relaxation are discussed.

1.2. Theoretical background

1.2.1. *The brittle-plastic transition*

Deformation in the brittle upper crust usually takes place by sudden displacement along faults during earthquakes (e.g. Yeats et al., 1997), whereas at greater depth, the lower crust deforms slowly by dislocation creep or diffusion creep at strain rates on the order of 10^{-14} - 10^{-16} s⁻¹. Therefore, the strength of the Earth's continental crust is described by two different models (e.g. Goetze and Evans, 1979; Brace and Kohlstedt, 1980; Scholz, 1990; Evans and Kohlstedt, 1995; Kohlstedt et al., 1995). The strength of the brittle upper crust, where the temperatures and lithostatic pressure are relatively low, is modelled by a failure criterion for frictional sliding on pre-existing faults based on Byerlee's law (Byerlee, 1978; Kohlstedt et al., 1995). The strength of the lower continental crust, where temperature and pressure are higher, is generally described by a power law rheology of quartz. Feldspar, which is the most common mineral in crustal rocks, reveals a higher flow strength than quartz and deforms by

brittle mechanisms at temperature below 500°C (Tullis and Yund, 1987; Hirth and Tullis, 1989; Tullis, 1990). The change between these distinct rheological regimes is not abrupt, but involves a gradual transition through a semibrittle regime, where both brittle and plastic mechanisms can act simultaneously.

The transition from brittle to plastic behaviour occurs in two stages (Fig.1.1): An initial change from the pressure-dependent, localised brittle failure to the distributed brittle and local plastic deformation is called the brittle-semibrittle transition (BST) (Scholz, 1990), or the brittle-ductile transition (Kohlstedt et al. 1995). The second change from semibrittle to purely plastic, pressure-independent flow is called the semibrittle-plastic transition (SPT) (Scholz, 1990), or the brittle-plastic transition (Kohlstedt et al. 1995). In the present study the terms after Scholz are used, who denoted the entire transition from purely brittle to purely plastic behaviour as brittle-plastic transition (BPT). Qualitatively, the BST is marked by the onset of plastic processes.

Empirically it has been found that the SPT is reached when the effective confining pressure exceeds the differential stress (Goetze's criterion, Kohlstedt et al., 1995). The effective confining pressure is defined as the lithostatic pressure minus the pore fluid pressure. The pore fluid pressure in the metamorphic upper crust, down to a depth close to the BST, is found to follow a hydrostatic gradient (Huenges et al., 1997; Grawinkel and Stöckhert, 1997). For the crust beneath the SPT the pore fluid pressure is generally expected to be close to the mean stress with $p_f \approx (\sigma_1 + \sigma_2 + \sigma_3)/3$. Plastic deformation at high differential stress requires sub-lithostatic pore fluid pressures (O'Hara, 1990; White, 1996; Küster and Stöckhert, 1999).

Experimental data for frictional sliding (e.g. Byerlee, 1978) and for dislocation creep of quartz (e.g. Paterson and Luan, 1990) can be used to estimate the BPT for typical continental crustal rocks. At geologically relevant strain rates of $d\epsilon/dt = 10^{-14}$ to 10^{-16} s^{-1} , the BPT is predicted at a temperature of $300 \pm 50^\circ\text{C}$. This prediction is consistent with the microstructural record of quartz in exhumed metamorphic rocks (e.g. Voll, 1976; Stöckhert et al., 1999; Hirth et al., 2001) and with the depth distribution of intracontinental earthquakes in relation to heat flow (e.g. Sibson, 1977; Scholz, 1990). The lower boundary of the seismogenic zone where earthquakes can nucleate is thought to occur at approximately the temperature of the onset of quartz plasticity at a depth of about 13-15 km, depending on the geothermal gradient (e.g. Chen and Molnar, 1983; Sibson, 1984; Tse and Rice, 1986; Yeats, 1997). Scholz (1990) proposed the term schizosphere for the brittle seismogenic upper layer where earthquakes can nucleate and the term plastosphere for the slowly creeping lower layer. These terms are adopted in the present study.

The essential character of the simplified model of the strength of the Earth's continental crust in Fig.1.1 is that the rock strength increases with depth until temperature gets sufficiently

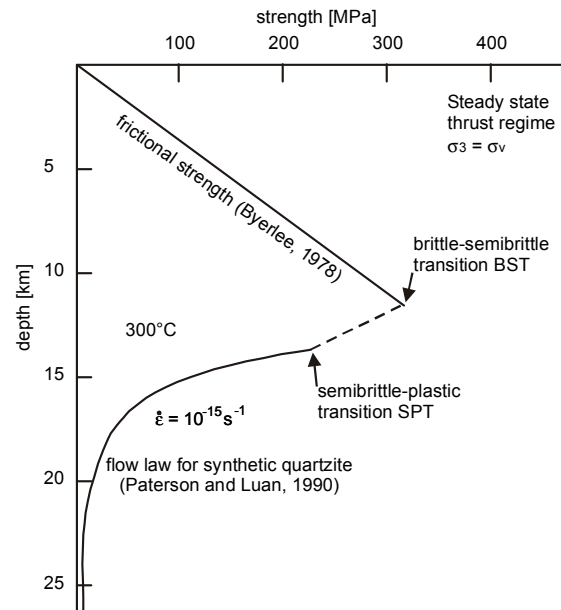


Fig. 1.1: Schematic and simplified illustration of the strength of the continental lithosphere as a function of depth.

high to allow plastic flow. Thus, the maximum strength of the continental crust is reached just beneath the BST.

The dependence of the maximum differential stresses in the lithosphere on the different tectonic regimes is described in Fig. 1.2. The stress required for thrust faulting ($\sigma_3 = \sigma_v$) is much greater than that for normal faulting ($\sigma_1 = \sigma_v$). The stress for strike-slip faulting ($\sigma_2 = \sigma_v$) lies in between (Scholz, 1990). Thus, the maximum differential stress to occur in the Earth's continental crust is expected in the thrust regime, just beneath the BST, with magnitudes of up to 0.1-0.3 GPa (Solomon et al., 1980; Engelder, 1993).

During uplift and erosion metamorphic rocks have to pass through the BPT, where the differential stress can reach these high values. Any microstructures developed at that stage can then remain recorded (Dresen et al., 1997), because during further exhumation temperatures are too low to allow recovery and microstructural changes apart from brittle failure. Thus, the microstructural record of exhumed metamorphic rocks reflects the conditions prevailing when the rock rose above the BPT-zone.

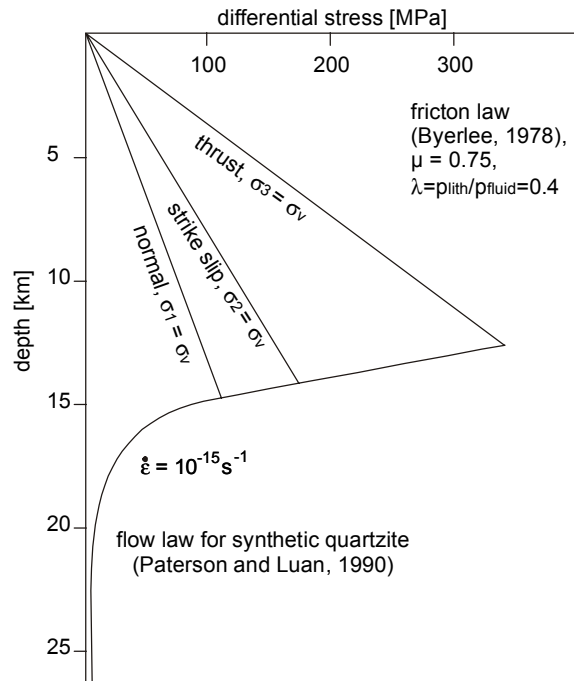


Fig. 1.2: Simplified model of the strength of the continental lithosphere in the different tectonic regimes (after Scholz, 1990).

1.2.2. The effect of seismic activity on the BPT

Abrupt stress and energy release accompanying seismic activity in the upper crust (e.g. Sibson, 1986) involves complex deformation processes within a large part of the Earth's crust. The present study deals with the effect of *major* earthquakes as defined by Scholz (1990), whereby failure occurs throughout the whole schizosphere. For continental crust with a schizosphere of about 15 km thickness the magnitude of such a major earthquake will be about $M = 6-6.5$ and greater.

As the depth of the BPT depends on temperature, strain rate and pore fluid pressure, it is not a stationary horizon but can be displaced by a change in any of these factors (Fig. 1.3). Major earthquakes in the schizosphere are expected to cause a widespread effect on pore fluid pressure and on the strain rate beneath the BPT (e.g. Cohen, 1981; Tse and Rice, 1986; McCaig, 1988; Ivins, 1996).

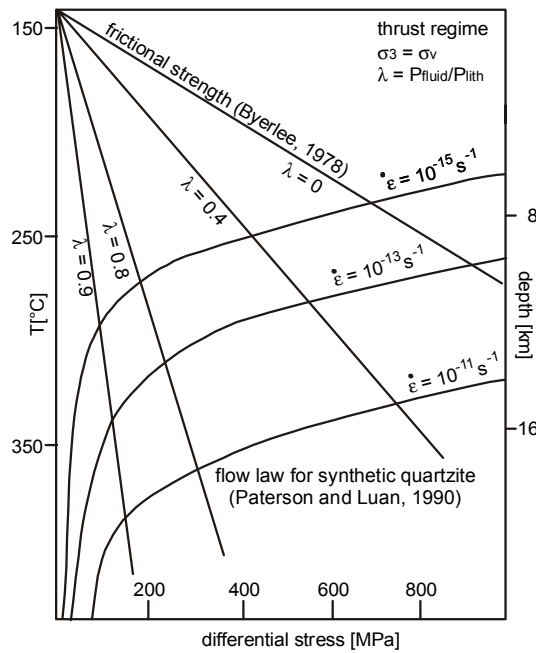


Fig. 1.3: Dependence of frictional strength (Byerlee, 1978) and flow law for synthetic quartzite (Paterson and Luan, 1990) on pore fluid pressure and strain rate, respectively (a geotherm of $22^\circ\text{C}/\text{km}$ is applied).

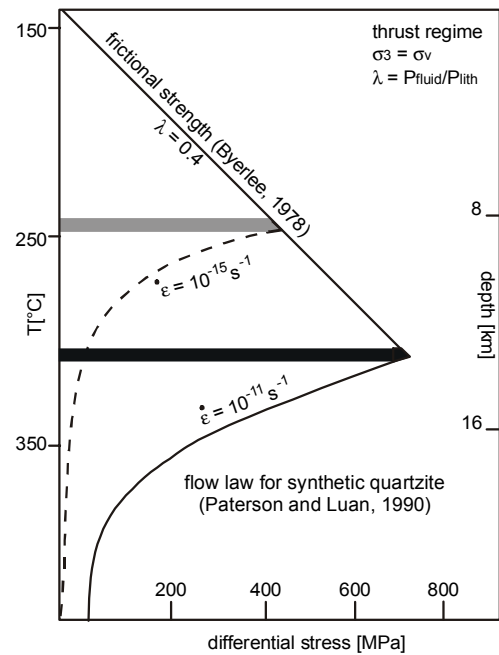


Fig. 1.4: Schematic displacement of the BPT to greater depth, caused by a major seismic event (a geotherm of $22^\circ\text{C}/\text{km}$ is applied).

Rupture along seismogenic fault zones in the schizosphere is expected to load the uppermost plastosphere (e.g. Li and Rice, 1987) causing transient extraordinarily high stresses. The higher strain rates imply a higher flow strength of quartz and thus can be expected to cause a displacement of the BPT to greater depth (Fig. 1.4). As a result of major earthquakes, ruptures are predicted to propagate into the uppermost plastosphere (e.g. Sibson, 1980; Scholz, 1988; Yeats, 1997).

Fracturing in the rupture zone can also lead to dilation and a high local permeability (e.g. McCaig, 1988). Influx of fluid into the fractures can be suspected to result in an abrupt release of pore fluid pressure (Küster and Stöckhert, 1999). Both an increase in strain rate and a drop of pore fluid pressure can cause a strengthening of the affected rocks (Figs. 1.3 and 1.4).

Because of the positive pressure dependence of silica solubility (e.g. Manning, 1994), reduction in the pore fluid pressure can also be expected to cause quartz precipitation along fractures (O'Hara, 1990). Fluid-filled cracks are predicted to have geologically short lifetimes at temperatures above 200°C (Smith and Evans, 1994). Therefore, sealing of synseismically induced fissures and cracks by precipitation from the pore fluid is expected to be rapid in the uppermost plastosphere.

Temporal and local changes of seismic scattering properties related to the Loma Prieta earthquake (1989, magnitude 6.9) were proposed by Baisch (2000) and Baisch and Bokermann (2001) to reflect synseismic creation of cracks, with a progressive restoration after about 5 years, following a power-law dependence, which is reconciled with crack healing, fluid diffusion and/or postseismic deformation.

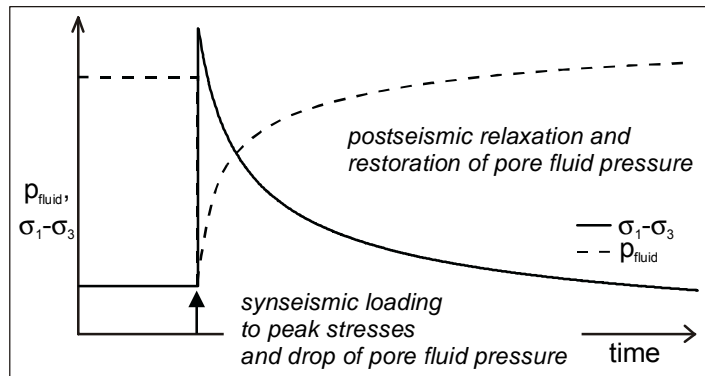


Fig. 1.5: Model for the processes of synseismic loading and post-seismic creep in the uppermost plastosphere.

It is convenient to distinguish between two different transient stages in the uppermost plastosphere related to major earthquakes in the overlying schizosphere (Fig. 1.5): (1) a stage of synseismic loading with an instantaneous increase in differential stress and a simultaneous drop in pore fluid pressure to sublithostatic values due to dilation and downward propagation of faults and (2) a subsequent stage of postseismic creep during progressive relaxation, with rapidly decaying differential stress and restoration of pore fluid pressure by sealing of the synseismic fissures and cracks.

1.3. Present aims

Syn- and postseismic deformation in the uppermost plastosphere, as envisaged above, should be recorded by characteristic microstructures of the affected rocks. The rocks of the Sesia Zone in the Western Alps provide an example of microstructures developed during rapid, non steady-state deformation within the uppermost plastosphere. The aims of the present study can be specified as follows:

- To examine potential microstructural criteria for synseismic loading and postseismic creep.
- To investigate the activated deformation mechanisms in the different rock-forming minerals.
- To reconstruct the magnitude of peak differential stress and the orientation of the stress field.
- To draw conclusions on the tectonic/geodynamic conditions.
- To gain information about the time and length scales relevant for loading and relaxation.

1.4. Organisation of the thesis

Following this introduction including a brief review of the concepts and theoretical background, a description of the analytical techniques used in the present study is provided in Chapter 2. The geology of the investigated areas in the Sesia Zone is briefly outlined in Chapter 3, while the occurrence of high-strain zones (mylonite, ultramylonite and pseudotachylyte) is covered in Chapter 4. Subsequent Chapters 5 to 7 focus on the specific microstructural criteria for synseismic loading and postseismic creep. Chapter 5 is dedicated to mechanical twinning of jadeite. Chapter 6 is concerned with the cataclastic deformation of garnet, and Chapter 7 deals with the low-temperature plasticity and creep of quartz. The results presented in Chapters 5 and 6 are published in Trepmann and Stöckhert (2001)* and in Trepmann and Stöckhert (2002)*, respectively. Also, the research presented in Chapter 7 has been submitted as an individual paper*. Chapter 8 is concerned with branching veins sealed with plastically deformed and recrystallised quartz. A general discussion and concluding remarks are given in Chapter 9.

* Trepmann C.A., Stöckhert B. (2001) Mechanical twinning of jadeite - an indication of synseismic loading beneath the brittle-ductile transition. *Intern. J. Earth Sci.* 90: 4-13.

Trepmann C.A., Stöckhert B. (2002) Cataclastic deformation of garnet: A record of synseismic loading and postseismic creep. *J. Struct. Geol.* 24: 1845-1856.

Trepmann C.A., Stöckhert B. (submitted to *J. Struct. Geol.*) Quartz microstructures developed during non-steady state plastic flow at rapidly decaying stress and strain rate.

2. Methods

2.1. Introduction

The different aspects of the meso- to submicroscopic structures that have been investigated in the present study require specific imaging, chemical and crystallographic analysis techniques. In this chapter the basic characteristics and applications of each method are outlined, with attention focused on the specific application in this study.

2.2. Sampling

A thorough microstructural analysis relies on conscientious sampling and field work. Oriented hand samples were collected and mesostructural features were studied in the field during 4 weeks in May and September 1998, two weeks in September 1999, and two weeks September 2000. Thin sections (ca. 25 μm thick) were produced from the samples in two different orientations: the first normal to foliation and parallel to lineation (xz section) and the second normal to both, foliation and lineation (yz section).

2.3. Optical microscopy and universal stage

Microstructures were studied in standard thin sections using a polarising microscope (Olympus BH-2 POL) with a 12.5x ocular and different objective lenses (2x; 10x; 25x; 40x). Most imaging was carried out with crossed polarisers, and some with the compensator plate (552 nm) inserted. Crystallographic orientation of crystals were measured with a Leitz universal stage (U-stage) mounted to a Leitz Orthoplan microscope.

2.4. Scanning electron microscopy (SEM)

The main advantage of scanning electron microscopy (SEM) in comparison to optical microscopy is its greater resolution of down to a few micron, allowing fine-scale microstructural analysis. SEM analyses were performed on a LEO 1530 electron microscope. The SEM is equipped with a field emission gun, energy dispersive X-ray (EDX), and electron backscatter diffraction (EBSD) facilities.

A field emission gun produces electrons that are accelerated by a high voltage (5-25 kV) through a condenser lens and focused by the objective lens onto the sample. Images are produced by scanning the beam in a raster pattern and displaying the signal from an electron detector on a screen. The electron beam interacts with the atoms in the sample, producing secondary electrons, backscattered electrons and characteristic X-rays, that can be detected by the SEM. For some of these techniques further preparation of polished thin sections and specific SEM conditions are required. These are described in the corresponding sections.

2.4.1. Secondary electron-imaging

Standard SEM secondary electron imaging was performed for the fine-scaled microstructural analysis of polished and carbon coated thin sections. The SEM was operated at acceleration voltages between 10 kV and 25 kV with a working distance of between 10 mm and 25 mm. Secondary electrons (SE), are ejected from the sample as a result of electron bombardment and are distinguished by their characteristic low energy of a few electronvolts. Only those electrons originating within a few nanometres of the surface are able to escape. The SE-signal contains therefore useful surface information.

2.4.2. Orientation contrast (OC)-imaging and Electron backscatter diffraction (EBSD)

Forward scattered orientation contrast (OC)-imaging and electron backscatter diffraction (EBSD)-techniques were performed for the investigation of grain and subgrain structure and crystallographic orientation analysis. Mechanically polished thin sections were chemically polished with a colloidal silica suspension (SYTON®) to reduce the surface damage. A thin layer of carbon was then deposited to reduce the influence of surface charging. The SEM was operated at an acceleration voltage of 25 kV, a working distance of 25 mm and a tilt angle of 70°.

Elastic interaction between the bombarding electrons and the nuclei of the atoms in the sample involves a large deflection with low energy loss. The so-called back-scattered electrons (BSE), which can be distinguished from SE electrons by their higher energy are detected with a BSE-detector. The BSE-signal is particularly sensitive to chemical differences, since the angular deflection is a function of atomic number.

The BSE-signal can also be used to provide an OC-image (Lloyd, 1987). The deflection of the back scattered electrons depends on the orientation of the deflecting crystal lattice plane in the sample. Under normal conditions, the atomic number contrast covers the OC-signal. This can be avoided using a tilted sample (Prior et al. 1996) and a BSE detector at a high angle to the electron beam, a so-called forescatter detector (Fig. 2.1).

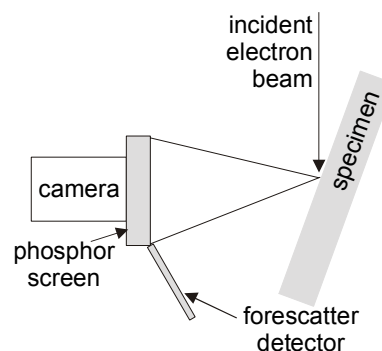


Fig. 2.1: Typical EBSD set-up in a SEM.

The OC provides a qualitative image of the crystallographic orientation (e.g. Prior et al. 1999). Regions of different crystallographic orientation appear as different grey shades (Lloyd, 1985), permitting the grain and subgrain structure of the sample to be imaged.

The forescatter configuration with a stationary electron beam is used for the generation of the EBSD-pattern. EBSD patterns are the backscattered equivalent of the classical Kikuchi bands observed in a transmission electron microscope. The patterns consist of a series of bands, each corresponding to a certain crystallographic plane. The width of the bands is inversely proportional to the lattice plane spacing. The EBSD-pattern is generated at one point on the sample, and is detected with a phosphor screen mounted in front of a low-light-level camera (Fig. 2.1). The diffraction bands are indexed and the full crystallographic orientation is calculated using the HKL software CHANNEL 4.0 (Schmidt and Olesen, 1989). The

data from manual EBSD measurements are presented in stereographic pole figures generated with the computer program StereoNett 2.0 (Duyster, 1996). All stereographic diagrams are presented in the lower hemisphere. For EBSD orientation mapping, where the stage is moved automatically in a grid wise fashion underneath the focused electron beam, automated acquisition and analysis was carried out using CHANNEL software. The resulting orientation map contains the full crystallographic orientation at each point, where each different crystallographic orientation is assigned to a defined colour.

The EBSD-technique allows the determination of the crystallographic misorientation between two points, which is given by the lowest misorientation angle and the related rotation axis (Wheeler et al., 2001). This can be calculated from measurements on pairs of neighbour grains or for randomly selected pairs and can be displayed in misorientation distribution histograms (Wheeler et al., 2001).

2.4.3. Energy dispersive X-ray (EDX)-analysis

The EDX technique at the SEM is used to get qualitative information on the chemical composition. The bombarding electrons interact with the electrons in the shells causing the emission of characteristic X-rays. An EDX spectrometer (Oxford) measures the energy and intensity of the emitted X-rays, allowing the chemistry of the sample to be determined. For this technique polished and carbon coated thin sections were used. The SEM was operated at acceleration voltages of 10 kV and a working distance of 10 mm.

2.5. Electron microprobe (EMP)

For the determination of quantitative mineral composition, a CAMECA SX 50 electron microprobe (EMP) was available. Element distribution mapping was done on a CAMEBAX microprobe from CAMECA. Carbon-coated polished thin sections were used.

Wavelength-dispersive spectrometers (WDS) in the EMP enable the quantitative measurements of the characteristic X-rays at defined wavelengths. The CAMEBAX has three detectors, while the SX 50 has four. Both microprobes have an EDX-spectrometer for qualitative measurements of the whole X-ray spectrum. As WDS crystals LiF-, PET-, TAP- and a PCO-crystal were used. The quantitative data were automatically corrected by the computer-system of the EMP.

Element distribution maps of Mg, Ca and Fe were recorded by measuring the intensity of the characteristic X-rays at any point of a defined area, with the stage moved automatically in a grid wise fashion underneath the focused electron beam. A two dimensional map is produced after processing of the data using the computer program XMAP of H.-J. Bernhardt.

2.6. Cathodoluminescence (CL)

Cathodoluminescence (CL) can reveal growth zones, healed cracks, and veins which are not visible optically (Marshall, 1988; Shimamoto et al., 1991). A CL microscope (HC1-LM) designed by U. Zinkernagel and modified by R. Neuser (Neuser, 1995) at the Ruhr-University, Bochum was used for the visualisation of microcracks and veins in fine grained matrices of pseudotachylytes and (ultra-)mylonites. An electron beam is focused on a polished thin section coated with gold or carbon. The incident electrons raise bound electrons to higher energy levels; when these return to their original state, the surplus energy is emitted as light quanta. Some minerals are inherently cathodoluminescent, but the intensity and colour of the light are often strongly influenced by defects in the crystal structure and by impurity atoms which behave as “activators” because they give rise to additional energy levels. In terms of these causative factors it is difficult to interpret CL spectra quantitatively (Marshall, 1988; Shimamoto et al., 1991).

2.7. Transmission electron microscopy (TEM)

Transmission electron microscopy (TEM) allows the analysis of submicroscopic structure, with a resolution below one micron. The arrangement and densities of dislocations and the (sub-)grain-structure in quartz were analysed using a TEM (Philips EM301, 100 kV) located in the material science department at the Ruhr-University of Bochum.

Because of the very strong interaction of electrons within the crystals, the rock slice must be less than about 200 nm thick to be sufficiently transparent to 100 kV electrons. A polished thin section (~ 25 µm) is first removed from the glass and broken into fragments. The rock slices are thinned by Ar-ion bombardment until small holes are visible. Observation in the TEM is only possible adjacent to these holes, where the sample is sufficiently thin.

Electrons are generated in a heated filament and are accelerated at voltages of 100 kV and focused by two condenser lenses onto a sample suspended in a high vacuum. The objective lens, immediately below the sample, collects and focuses the diffraction pattern. In order to form a highly magnified image the beam is then passed through electromagnetic lenses. By changing the strength of these lenses (altering the lens current) either a diffraction pattern of the sample or a transmitted image can be focused onto a fluorescent screen. The area of sample from which a diffraction pattern is derived can be selected by choosing an appropriate aperture in the image plane (selected area diffraction).

Diffraction contrast images were produced using bright-field (BF) conditions, with only the undiffracted (transmitted) beam is allowed to pass through the objective aperture in the back focal plane. Areas which diffract strongly cause an intensity loss of the transmitted beam and appear dark. A fully intact crystal is transparent, whereas crystal defects strongly diffract the electron beam. Thus dislocations, twins, subgrain- and grain-boundaries are observed as dark lines.

2.8. Fourier transform infrared (FTIR)-spectroscopy

Fourier transform infrared (FTIR)-spectroscopy enables the identification of various water-related defects (Paterson, 1989). For FTIR-spectroscopy, electromagnetic radiation in the infra-red range (wavelengths from 2-25 μm) is transmitted through a polished thick section. The radiation induces the vibration of atoms, and is absorbed at the frequency corresponding to the vibration modes in the sample. The transmission spectrum reveals information about the atomic bonding mode and about the concentration of the vibrating molecules.

The type and concentration of water and water-related defects in quartz was studied by Fourier-Transform-Infrared-Microspectrometry (FTIR) (e.g. Kronenberg and Wolf, 1990), using an infrared (IR) spectrometer (Bruker IFS 48) with an attached IR-microscope. The IR microscope allows spectrometric analysis with a spatial resolution of ca. 0.1 mm, using polished sections of 0.1 to 0.2 mm thickness. FTIR measurements were performed both at room temperature ($\sim 295\text{K}$) and at a temperature of about 100 K in order to discriminate freezable water and to enhance the signal of point defects. The OH-concentration in quartz was calculated from the absorption spectra in the wave-number range of $3000 - 4000 \text{ cm}^{-1}$ following the method proposed by Paterson (1982).

3. Geological setting

3.1. Introduction

In the present study the microstructural record of rocks has been investigated from four localities of the Sesia Zone in the Western Alps, N-Italy: Val Chuisella, the lower Aosta valley, Mt. Mucrone and Bard (Fig. 3.1). In this chapter the geological setting of the Sesia Zone and of the investigated areas is outlined briefly. For comprehensive petrographic and geological details of the Sesia Zone the reader is referred to Compagnoni (1977) and Venturini (1995). For detailed description of the geology and deformation structures of the lower Aosta valley, see Richter (1984).

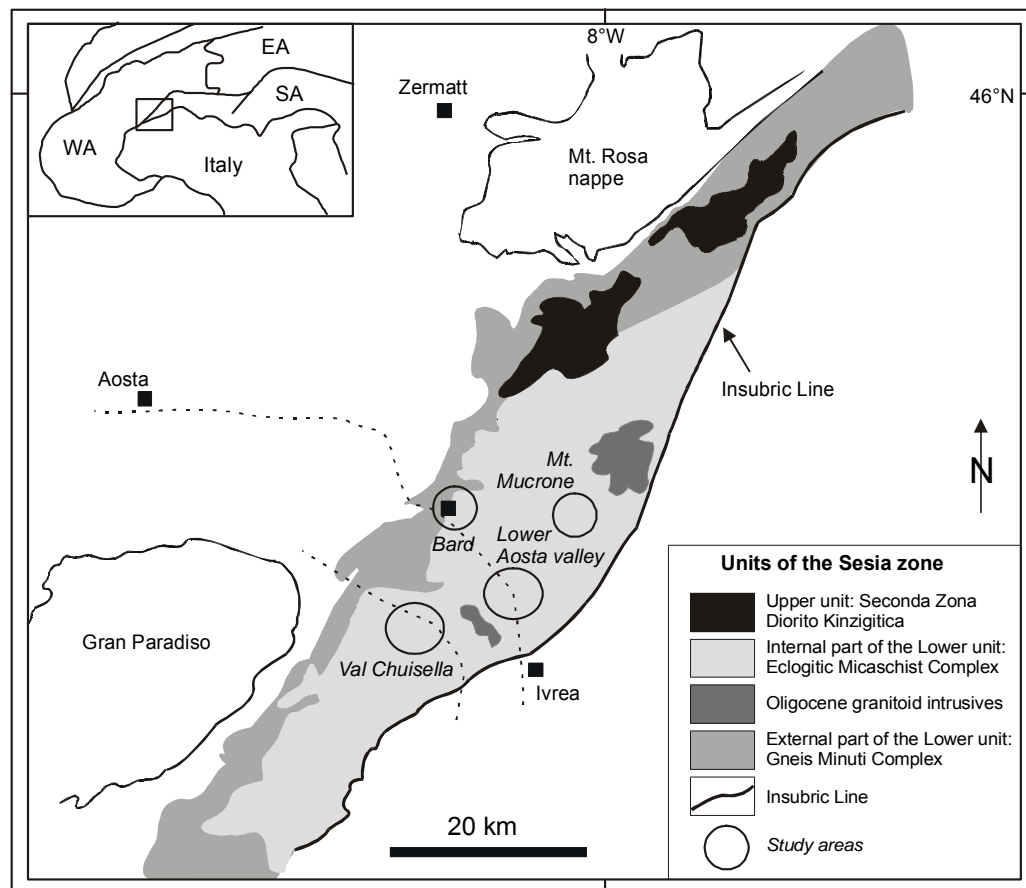


Fig. 3.1: Sketch map of the tectonic units of the Sesia Zone with study areas.

3.2. Geological overview

The Sesia Zone (Fig. 3.1) is an Austroalpine unit in the Western Alps extending over about 125 km from Locarno in the NE to Turin in the SW. It represents the uppermost element of the Europe-vergent Alpine nappe pile derived from the basement of the southern overriding continent in the Alpine collision zone (Compagnoni et al., 1977).

The rocks underwent an amphibolite or granulite facies metamorphism during the Variscan orogeny (Venturini, 1995). During Alpine subduction and collision they were buried to about 60 km depth and underwent an eclogite facies high pressure metamorphism at $T =$

550±50°C and $P = 1.8 \pm 0.3$ GPa (Compagnoni, 1977; Pognante, 1989; Avigad, 1996) in the late Cretaceous/early Tertiary at ≈ 65 Ma (Inger et al., 1996; Rubatto et al., 1999; Liermann et al., 2002). Fission track ages from zircon and apatite, indicate cooling to below 280±30°C at ca. 35 Ma and below 120°C at ca. 25 Ma, respectively (Hurford et al., 1991). In the Oligocene and Miocene the Sesia Zone has been displaced upwards by several tens of kilometres with respect to the adjacent South Alpine basement (Ivrea Zone) along the Insubric Line, the western segment of the Periadriatic lineament (Schmid et al., 1989).

3.3. Geological setting of the investigated areas

The Sesia Zone (Fig. 3.1) is subdivided into an upper and a lower tectonic unit (Compagnoni, 1977). The upper unit consists of a polymetamorphic complex known as the Second Dioritic-Kinzigitic Zone (IIDK), which is lithologically similar to the kinzigite series of the Ivrea Zone. The lower unit of the Sesia Zone is composed of a polymetamorphic basement complex (Venturini, 1995), which is derived from pre-Alpine HT-metamorphic paragneisses, granulites and amphibolites that underwent further Alpine high pressure metamorphism. The lower unit of the Sesia Zone has been further subdivided into an external and an internal part (Fig. 3.1), based on different Alpine metamorphic overprint:

- the internal part is known as the Eclogitic Micaschist Complex (EMC), where the high pressure assemblages are well preserved;
- the external part, the Gneiss Minuti Complex (GMC), high pressure mineral assemblages are replaced by greenschist facies minerals, which define the main foliation.

The three investigated areas of Val Chuisella, the lower Aosta valley, and Mt. Mucrone are located in the EMC (Fig. 3.1). Reddish omphacite and garnet bearing micaschist are the predominant lithologies, crosscut by veins of metaaplite and metapegmatite. Eclogites and impure marbles are embedded as layers and boudins in the eclogitic micaschists and gneisses. Kilometre-sized bodies of Permian jadeite-bearing metagranites and metagranodiorites are exposed in the Mt. Mucrone area (Compagnoni and Maffeo, 1973; Oberhänsli et al., 1985) and the lower Aosta valley. The investigated area around the old roman village Bard is located at the contact between the GMC and the EMC (Williams and Compagnoni, 1983). In the GMC a greenschist assemblage overprints the earlier high pressure signature, and medium-grained albite-epidote-two-mica gneisses are the dominant lithology.

In the lower Aosta valley a late stage of intense inhomogeneous ductile deformation is described by Richter (1984). Küster and Stöckhert (1999) attributed this high stress deformation at the crustal level just beneath the brittle-plastic transition (300-350°C, 16-20 km) to postseismic creep in the uppermost plastosphere caused by a major earthquake in the overlying schizosphere. These authors concluded that the seismic event must have occurred after high pressure metamorphism but before cooling to below 280±30°C, thus between 65 and 35 Ma along a precursor of the prominent Insubric fault zone. The microstructural record related to this deformational stage is the subject of the present thesis.

4. High-strain zones

4.1. Introduction

Some fault zones may pass through the entire schizosphere and continue in the uppermost plastosphere as ductile shear zones (e.g. Tse and Rice, 1986; Scholz, 1990). Fault rocks are generally divided into (1) brittle fault rocks, including cataclasite and pseudotachylyte, and (2) ductile fault rocks, including mylonites and ultramylonites. The ductile fault rocks are thought to deform primarily by plastic mechanisms, with brittle deformation playing a subordinate role. On the contrary, brittle fault rocks are the product of comminution (cataclasite) and frictional melting (pseudotachylyte) in the brittle regime. The presence of pseudotachylyte is generally accepted to represent direct evidence of seismic activity of a fault zone, as it is thought to form by local melting of the rock due to heat generated by rapid frictional sliding (e.g. Sibson 1975; Spray, 1987; Spray, 1992).

The widely accepted Sibson-Scholz conceptual model for major seismic fault zones (Fig. 4.1) describes the occurrence of brittle fault rocks in the seismogenic layer and ductile fault rocks at greater depth (e.g. Sibson, 1977; Scholz, 1988, 1990). Mylonitisation and pseudotachylyte formation can overlap in a transitional regime below the onset of quartz plasticity, due to the downward propagation of faults (see Chapter 1.2.2; Sibson, 1980; Passchier, 1982; Scholz, 1988; Koch and Masch, 1992).

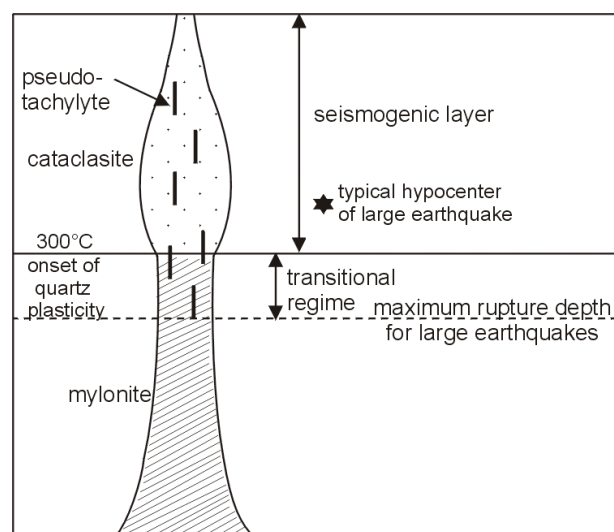


Fig. 4.1: Simplified model of a continental fault zone, after Scholz, 1990.

Alternative explanations for the association of pseudotachylyte and ductile fault rocks include:

- Synkinematic generation of pseudotachylytes and mylonites by transient plastic instabilities in the ductile regime (White, 1996; Hobbs et al., 1986).
- Cyclic generation of pseudotachylyte, cataclasite and mylonite by alternating seismic and aseismic slip behaviour at the base of the seismogenic zone (Stel, 1986; McNulty, 1995).
- Mylonite development followed by the generation of pseudotachylyte during gradual exhumation of an active seismic fault zone (Swanson, 1992).

Strain accumulated during the late stage deformation in the studied part of the Sesia Zone is concentrated in small scale high-strain zones. In contrast, contemporaneous strain is remarkably low in the intervening rocks, generally not exceeding some tens of percent. The high-strain zones can be developed as mylonites (at Val Chuisella, lower Aosta valley, and Mt. Mucrone), ultramylonites (at Val Chuisella, lower Aosta valley) and pseudotachylytes (at

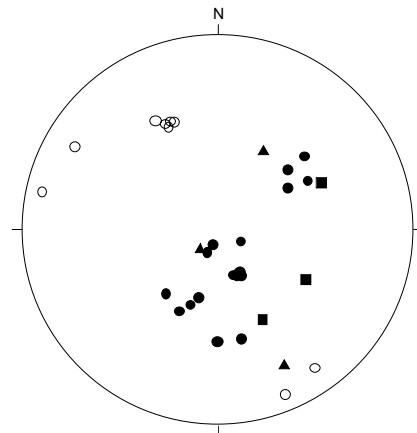
Mt. Mucrone) in metagranites, eclogites, eclogitic micaschists and gneisses. They are described in the following sections.

4.2. Mylonites

Mylonites are exposed as centimetre to decimetre wide zones in the eclogitic micaschists and gneisses at Val Chuisella, lower Aosta valley, and at Mt. Mucrone. They are characterised by a prominent, strong foliation and a weak to marked lineation. The orientation of the mylonitic foliation is variable, mostly subparallel to the foliation of the host rock - with a dip of 15-75° to the NW, SSE and SSW (Fig. 4.2). The small-scale mylonites are macroscopically difficult to recognise as the host rocks themselves have undergone a complex deformation history (Richter, 1984).

Fig. 4.2: Stereographic projection of mylonitic foliation and corresponding lineation.

- poles of mylonitic foliation in rocks from the lower Aosta valley.
- lineation in mylonites from the lower Aosta valley.
- poles of mylonitic foliation in rocks from Val Chuisella.
- ▲ poles of mylonitic foliation in rocks from Mt. Mucrone.



The penetrative foliation (Fig. 4.3a, b) is defined by alternating quartz-rich and phengite-rich layers. Phengite crystals were deformed - depending on their orientation - by intense basal shear or by kink band formation (Fig. 4.3a, b, Richter, 1984). Along kink band boundaries they can be recrystallised. Garnet porphyroclasts (Fig. 4.3c) are isolated in the quartz and mica matrix and can be deformed by cataclastic flow (Küster and Stöckhert, 1999), which is treated in detail in Chapter 6. Favourably oriented jadeite (see Chapter 5), omphacite, titanite, and calcite crystals (Küster and Stöckhert, 1999) were deformed by mechanical twinning. K-feldspar, epidote, albite, glaucophane, rutile and apatite form rigid porphyroclasts, or are fragmented in a manner similar to garnet (Fig. 4.3c, d). The quartz microstructure (Fig. 4.3d) indicates complex non-steady state ductile deformation as described in detail in Chapter 7.

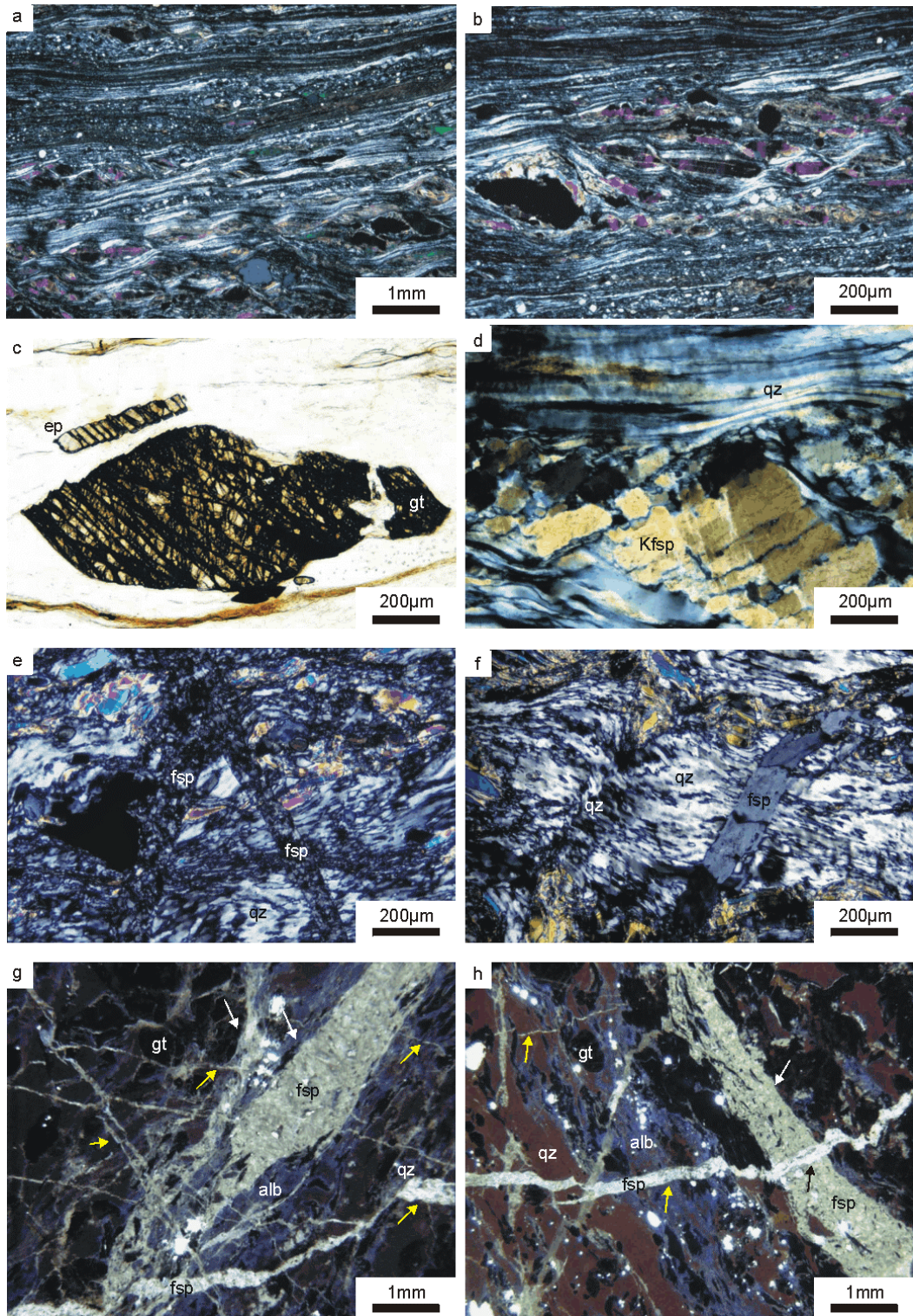


Fig. 4.3a, b: Microstructure of a mylonite from the lower Aosta valley (St12), optical micrograph taken with crossed polars. **Fig. 4.3c:** Optical micrograph of a fragmented garnet (bottom) and epidote (top), in sample CT183 from the lower Aosta valley. **Fig. 4.3d:** Optical micrograph showing heterogeneous ductile deformation of quartz and cataclastic deformation of feldspar in a mylonite sample from the Val Chuisella (CT177), crossed polars. **Fig. 4.3e:** Feldspar veins in sample CT82 from the Mt. Mucrone, optical micrograph taken with crossed polars. **Fig. 4.3f:** Optical micrograph, showing a small scale, ductile quartz shear zone (left) parallel to a feldspar vein (right) in sample CT82, crossed polars. **Fig. 4.3g, h:** CL micrograph of sample CT82. Albite veins show grey to bluish luminescence, whereas the matrix albite reveals a violet luminescence colour. Apatite appears bright and quartz dark red, mica and garnet are not luminescent. Feldspar veins parallel to foliation are indicated by white arrows, smaller veins in high angle to foliation by yellow arrows.

The microstructures of the mylonites from Mt. Mucrone are somewhat different from those of the lower Aosta valley and Val Chuisella. Irregular and sometimes branching feldspar filled fractures (Fig. 4.3e, f) are observed exclusively in the mylonites from the Mt. Mucrone area. They are particularly conspicuous in the CL-microscope (Fig. 4.3g, h) with a grey to bluish luminescence colour. The feldspar composition has been determined by microprobe (see Appendix B, Table 1) and comprises predominantly albite: $\text{alb}_{90-96}\text{Or}_{0-2}\text{An}_{2-7}$ and oligoclase: $\text{alb}_{84-87}\text{Or}_{0-2}\text{An}_{11-15}$ with minor K-feldspar: $\text{alb}_{2-3}\text{Or}_{96}\text{An}_{0-1}$. The feldspar veins can occur as a few hundred micron wide zones parallel to foliation (Fig. 4.3g, h; white arrows) or following small fractures oriented at a high angle to the foliation (Fig. 4.3g, h; yellow arrows). Where both types of veins intersect, the lack of offset of the smaller fractures oriented at a high angle to foliation indicates that they developed at a late stage (black arrow in Fig. 4.3h). Sometimes a small shear component can be recognised by minor offset of garnet crystals. Feldspar in the veins consists of either coarse-grained albite or a fine-grained aggregate of albite, K-feldspar, plagioclase and quartz. Coarse-grained feldspar veins can occur parallel to small scale ductile shear zones in quartz layers (Fig. 4.3f). The relationship between feldspar veins and the very heterogeneously ductile deformed quartz matrix indicate that these brittle features were generated simultaneously, or at least alternating with plastic deformation of quartz.

4.3. Ultramylonites

Ultramylonites, characterised by a very fine grained matrix with isolated, rounded porphyroclasts, are observed in the metagranites and micaschists at the lower Aosta valley and at Val Chuisella. Macroscopically they are characterised by centimetre wide, sharply-bounded bands with a dark, aphanitic appearance, cutting through the light host rock (Fig. 4.5a-c). Mostly they show no abrupt changes in thickness, although they are sometimes branching (Fig. 4.5a-c). In one metagranite outcrop about twenty parallel ultramylonite zones (Fig. 4.5a) are observed in a section of 40 m length. In one metagranite outcrop about twenty parallel ultramylonite zones (Fig. 4.5a) are observed in a section of 40 m length.

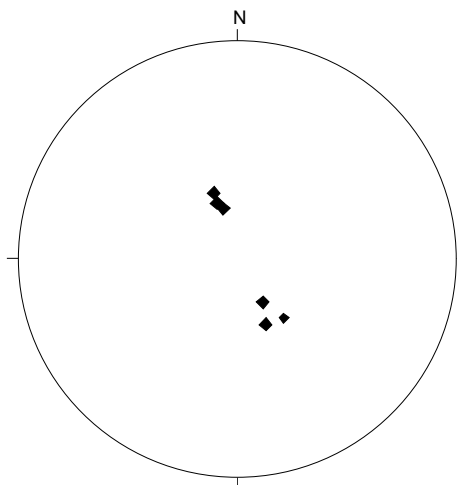


Fig. 4.4: Stereographic projection of poles of ultramylonites from the lower Aosta valley.

The ultramylonites are mostly oriented parallel to the Alpine foliation, dipping at a low angle (Fig. 4.4) to the SE or to the NW (Richter, 1984). However, some are developed oblique to foliation (Fig. 4.5d). Rarely, they reveal irregular margins, which intrude into the mylonitic matrix (Fig. 4.5e).

The fine-grained (2-6 μm) matrix is made up of albite, quartz, K-feldspar and mica, as identified by CL, EDX and EMP analysis (Figs. 4.5d, 4.5g-j and 4.6).

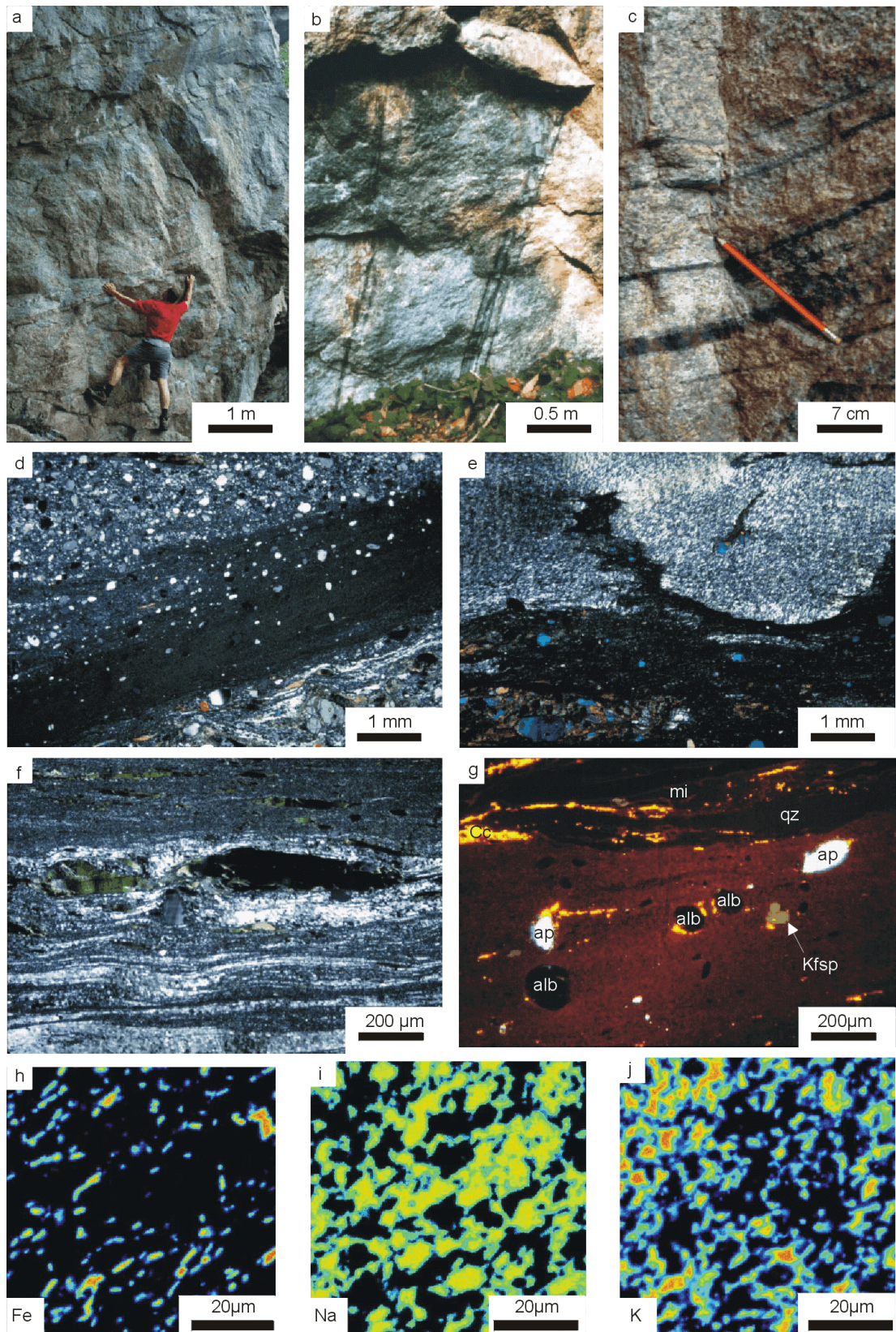


Fig. 4.5a-c: Ultramylonites exposed in metagranite from the lower Aosta valley. **Fig. 4.5d:** Ultramylonite (CT134) oriented oblique to the foliation of the host metagranite (left, top), optical micrograph, crossed polars. A gradual decrease in grain size and amount of porphyroclasts towards the ultramylonitic band is conspicuous (right, bottom). **Fig. 4.5e:** Micrograph of an ultramylonite (HB9) in an eclogitic micaschist extending into an adjacent quartz-rich mylonite, crossed polars. **Fig. 4.5f:** Micrograph of an ultramylonite (CT152) showing a gradual transition into a mylonite, crossed polars. **Fig. 4.5g:** CL micrograph of an ultramylonite (CT32) in a metagranite. Luminescence colours of the minerals present

are: matrix albite - red, calcite - bright orange, K-feldspar - green, apatite - bright white, quartz - dark red, albite porphyroclasts and mica reveal no luminescence colour. **Fig. 4.5h-j**: EMP element distribution maps of the matrix from an ultramylonite (CT32). Mapped elements are iron - representing phenigite -, sodium - representing albite - and potassium - representing K-feldspar -, respectively.

A weak compositional layering defined by alternating quartz and mica rich layers (Fig. 4.5d-f) is developed with a weak shape-preferred orientation of the matrix minerals (Fig. 4.6) parallel to the margins of the band.

The shape of the porphyroclasts with a diameter of 80-500 μm is conspicuously rounded or elongated. In the latter case the long axes are mostly oriented parallel to the layering (Figs. 4.5.d, g and 4.6). The porphyroclasts in the order of decreasing abundance are: albite, mica, apatite, K-feldspar, titanite and zircon (Fig. 4.5g). The albite porphyroclasts reveal no luminescence and are composed of 99% albite-component. In contrast, albite in the matrix, which is red luminescent (Fig. 4.5g), comprises 95-97% albite- and 3-5% K-feldspar component (see Appendix B, Table 1). Asymmetric strain shadows can occur at the porphyroclasts, and are commonly filled with K-feldspar or calcite (Figs. 4.5g and 4.6). The microstructures of the ultramylonites suggest deformation by grain-boundary sliding, with minor dislocation glide (e.g. Stünitz and FitzGerald, 1993).

In some cases ultramylonitic zones adjacent to mylonitic zones with margins oblique to the foliation of the host rock are observed (Fig. 4.5d). Certain samples show a gradual decrease of grain size towards the ultramylonitic zone (Fig. 4.5d, f), revealing a gradual transition from mylonitic to ultramylonitic microstructure. Fig. 4.5e shows an ultramylonite, which propagates into a mylonitic quartz matrix. The microstructural relationship between ultramylonites and mylonites implies that they formed simultaneously.

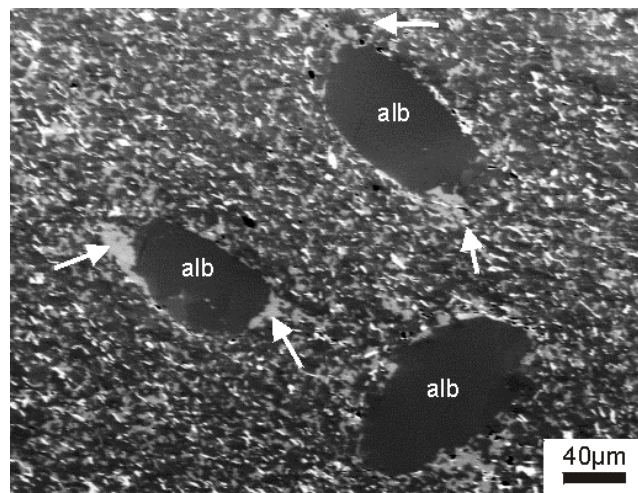


Fig. 4.6: SEM-image of an ultramylonitic zone, showing albite porphyroclasts with asymmetric strain shadows (arrows), filled predominantly with K-feldspar.

4.4. Pseudotachylytes

In the well exposed eclogites and garnet-gneisses from Mt. Mucrone, randomly oriented, cm-scale, light green pseudotachylytes are observed, forming characteristically branching injection veins (Fig. 4.7a, b).

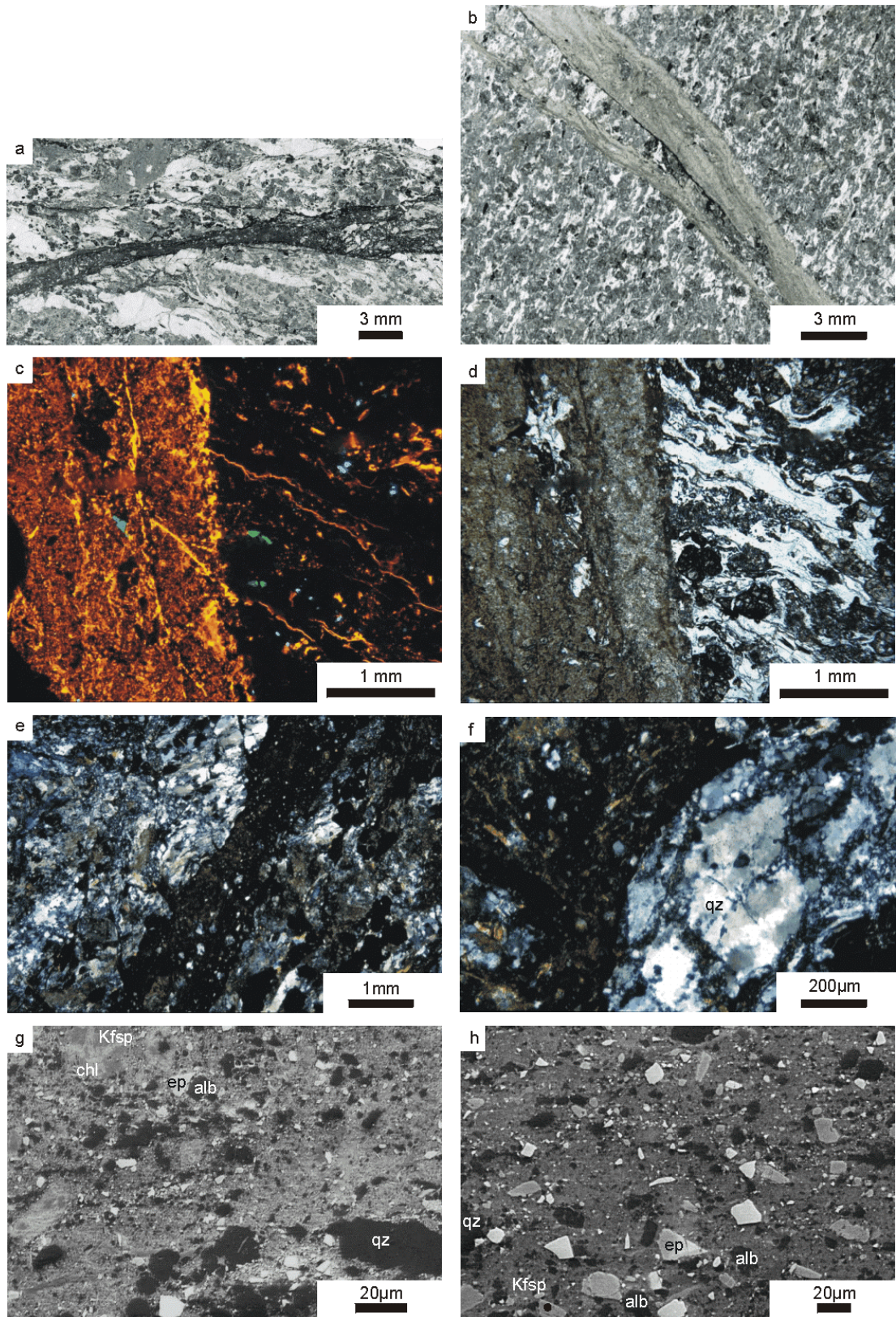


Fig. 4.7a, b: Thin sections of garnet gneisses from Mt. Mucrone (CT207 and CT208) with branching injection-veins of pseudotachylyte. **Fig. 4.7c:** CL micrograph of pseudotachylyte in a garnet gneiss (CT207), revealing a high amount of calcite (orange luminescent) and albite (light red), titanite is blue-green luminescent, apatite is white. Quartz, garnet and mica reveal no luminescence colour. **Fig. 4.7d:** Optical micrograph of the same area as in (c). **Fig. 4.7e, f:** Optical micrographs (crossed polars) from pseudotachylytes in a garnet gneiss (CT209), showing undulatory extinction and subgrains in quartz. **Fig. 4.7g, h:** SEM images of a pseudotachylyte (CT208) with fine-grained, heterogeneous matrix and fragments of mainly epidote, albite, quartz and chlorite.

Microscopically the pseudotachylytes consist of a dark brown to green matrix (Fig. 4.7 a, b) with many crystal fragments enclosed. The fragments are composed of epidote, quartz, albite, K-feldspar, garnet, and titanite as revealed by CL, EDX and EMP techniques (Fig. 4.7c, d, g, h). They have an irregular shape with a typical particle size of about 10 to 20 μm (Fig. 4.7g, h), but up to 100 μm in places. The barely resolvable fine-grained (grain size < 4 μm), heterogeneous and unfoliated matrix is composed of albite, quartz, chlorite, phlogopite and calcite, as identified by EDX analyses at the SEM.

The quartz matrix of the host rock, as well as quartz fragments enclosed in the pseudotachylytes reveal undulatory extinction, subgrains and sutured high angle grain boundaries with a wavelength of a few μm (Fig. 4.7e, f), suggesting that strain-induced grain boundary migration was active. The optical observations of the relationship between quartz microstructure and injection veins suggest that the pseudotachylytes formed simultaneously or intermittently with ductile deformation of quartz.

4.5. Discussion and conclusions

The temperatures during the late stage deformation in the lower Aosta valley were estimated by Küster and Stöckhert (1999) at approximately 300-350°C. These temperatures are thought to hold true for mylonite and ultramylonite generation, as well.

Pseudotachylytes have been observed exclusively in the Mt. Mucrone area. It is possible that some ultramylonites from the lower Aosta valley, which sometimes occur oblique to foliation of the host rock and locally propagate into the mylonitic matrix (Fig. 4.5e), represent crystallised pseudotachylytes. However, most ultramylonitic zones are parallel to the foliation of the host rock and sometimes show a gradual transition to a mylonitic microstructure. These observations would suggest their generation as ductile shear zones.

Both possibilities, either the exclusive generation of pseudotachylytes in the area of Mt. Mucrone, or the crystallisation of original pseudotachylytes, now appearing as ultramylonites, in the lower Aosta valley (but not in the Mt. Mucrone area) may mean that temperature was lower during deformation in the Mt. Mucrone area, compared to the lower Aosta valley and Val Chuisella. Additionally, frequent microcracks sealed with feldspar in mylonites from the Mt. Mucrone area imply more intense brittle behaviour, which also suggests somewhat lower temperatures during deformation in comparison to the other two regions. Although temperatures during mylonitisation and pseudotachylyte generation must still have been sufficiently high to allow ductile deformation of quartz. This requires temperatures of at least approximately 300°C as indicated by experimental flow laws (e.g. Paterson and Luan, 1990) and by the microstructural record of naturally deformed rocks (e.g. Voll, 1976; Stöckhert et al., 1999; Hirth et al., 2001).

These differences in microstructure can be interpreted in two ways:

- the (ultra-)mylonitisation in the lower Aosta valley and Val Chuisella and the mylonitisation concomitant with pseudotachylyte generation at the Mt. Mucrone is related to the same deformation event. The formation of pseudotachylyte at the Mt. Mucrone at about 300°C would suggest that the rocks were located in the transitional regime (see Fig. 4.1) according to the Sibson-Scholz conceptual fault model. Rocks from the lower Aosta valley and Val Chuisella would be located at a somewhat lower crustal level.

- the generation of the pseudotachylyte at the Mt. Mucrone is attributed to seismic activity after mylonitisation in Val Chuisella and lower Aosta valley, when the rocks were exhumed to a shallower crustal level. The pseudotachylytes could thus reflect a later stage.

Overall, the (ultra-)mylonitisation in the investigated area can be attributed to the late-stage high-stress deformation, reported by Küster and Stöckhert (1999). The occurrence of pseudotachylytes concomitant (or intermittent) with plastic deformation of quartz in the Mt. Mucrone area supports the proposed relation to seismic activity in the overlying schizosphere.

5. Mechanical twinning of jadeite*

5.1. Introduction

The metagranite from the Sesia Zone contain jadeite crystals which commonly reveal mechanical twins. Mechanical twinning is a widespread deformation mechanism in minerals of low symmetry, including carbonate minerals, plagioclase and clinopyroxene. In calcite twinning is ubiquitous because a low resolved shear stress of less than 10 MPa is required for twinning (e.g. Tullis, 1980). In calcite aggregates, the orientation distribution of such twinned crystals has been used to derive the orientation of the local stress field (Turner, 1953; Spang, 1972, 1974; Tullis, 1980, Rowe and Rutter, 1989). Also, calcite twin morphology has been used to gain information on thermal history (e.g. Burkhard, 1993). In contrast to calcite, mechanical twinning of clinopyroxenes is not common and is suggested to be a deformation mechanism restricted to low temperature and very high strain rates (Raleigh and Talbot, 1967; Carter and Raleigh, 1969; Wenk, 1970; Kirby and Christie, 1977; Avé Lallement, 1978; Kollé and Blacic, 1982; Godard and van Roermund, 1995). Raleigh and Talbot (1967) have shown that the method developed by Turner (1953) to derive the principal stress directions from the orientation distribution of twinned calcite crystals can also be applied to naturally deformed clinopyroxene aggregates. In accordance with theory (e.g. Tullis, 1980), Kollé and Blacic (1982) demonstrated that the twinning stress does not depend on temperature or strain rate. If the critical resolved shear stress (CRSS) is known, the differential stress can be derived from the analysis of the orientation distribution of twinned crystals in a deformed rock (Kollé and Blacic, 1982).

In this chapter, the method of dynamic analysis (Raleigh and Talbot, 1967) is applied to mechanically twinned jadeite to derive the orientation of the maximum principal stress. The orientation of individual twinned jadeite crystals is then used to estimate the magnitude of differential stress at the time of twinning, assuming that the CRSS found for other clinopyroxene compositions also holds approximately for jadeite.

5.2. Mechanical twinning of clinopyroxene

Mechanical twinning can be described as a homogeneous simple shear, with the shear strain and shear sense fixed for a given twin law. A sphere inscribed within a crystal is deformed into a triaxial ellipsoid (Fig. 5.1b). The circular section K_1 of this ellipsoid remains undistorted and is denoted as the twin or composition plane. The second circular section K_2 rotates while twinning into the K_2' position, but also remains undistorted. By definition, the shear plane is normal to K_1 and contains the shear direction η_1 . The direction η_2 parallels the intersection of the shear plane and K_2 . The angle ψ between K_2 and K_2' , and therefore the amount of shear $s = 2 \tan(\psi/2)$, are defined by crystallography, with $\psi/2 = \beta - 90^\circ$.

*The results presented in this chapter are published in:

Trepmann C.A., Stöckhert B. (2001) Mechanical twinning of jadeite - an indication of synseismic loading beneath the brittle-ductile transition. *International Journal of Earth Science* 90: 4-13.

For the angle $2\phi = (180^\circ - \beta)$ between the two circular sections the amount of shear is given by $s = 2\cot(2\phi)$. The plane oriented perpendicular to η_1 before mechanical twinning is rotated by the angle ψ' , and $s = \tan\psi'$. Specification of the elements K_1 and K_2 is sufficient to define a twin, but usually the four elements K_1 , η_1 , K_2 and η_2 are cited. The twin glide elements of two reciprocal mechanical twins in clinopyroxenes were determined by Raleigh and Talbot (1969) as: lamellar twins parallel to (100): composition plane $K_1 = (100)$; $K_2 = (001)$; shear direction $\eta_1 = [001]$; $\eta_2 = [100]$ and basal twins parallel to (001): composition plane $K_1 = (001)$; $K_2 = (100)$; shear direction $\eta_1 = [100]$; $\eta_2 = [001]$.

Because all four indices are rational, the twins are labelled compound twins. Jadeite is monoclinic with the space group $C2/c$ (Fig. 5.1a). The idealised clinopyroxene structure can be described as (100) layers containing chains of $[\text{SiO}_4]^{4-}$ tetrahedra, stacked alternately with (100) layers of cations in eight- and six-fold coordination, respectively. Therefore, the main structural change that occurs during mechanical twinning on (100) is the reorientation of the cation coordination polyhedra. The structure of the (100) twin boundary is described by Kirby and Christie (1977) by a displacement of $\frac{1}{2} [001]$ of the tetrahedral-chains. For the host grain and a (100)-twin lamella, only the orientation of the $\langle a \rangle$ axis is different (see Fig. 5.1b,c). The amount of shear related to twinning is determined by the angle $\beta = 107.6^\circ$, where $s = 2\tan(\beta - 90^\circ) = 0.63$.

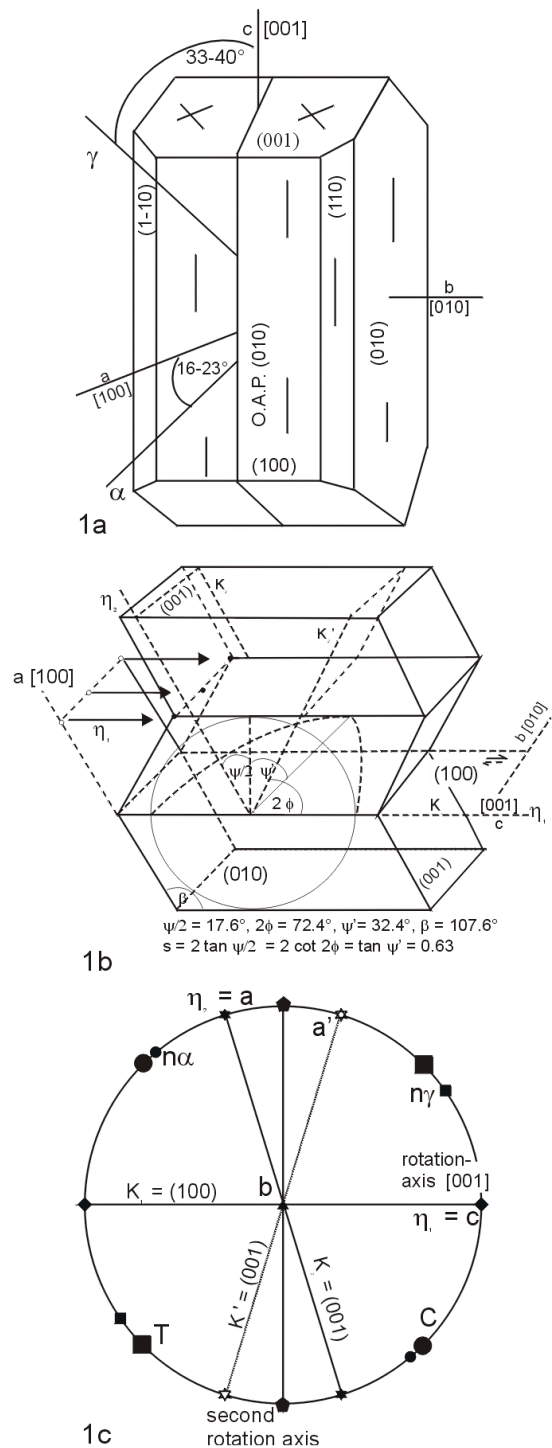


Fig. 5.1a: Crystallographic planes and directions in jadeite. **Fig. 5.1b:** Scheme of (100) twinning in jadeite: The (100) plane is the twin and composition plane. The shear direction is [001]. **Fig. 5.1c:** Stereographic projection of crystallographic planes and directions for a twinned jadeite. The most favourable orientation of the crystal for twinning on (100) is that with the σ_1 direction at 45° to (100) and [001], and at 27.4° to the $\langle a \rangle$ axis, and with the σ_3 direction at 62.6° to the $\langle a \rangle$ axis, all directions being parallel to (010). The σ_1 and σ_3 directions most favourable for twinning are termed C and T, respectively.

The twin orientation can be considered as the result of either a 180° rotation about η_1 (i.e. a reflection on (100)) or a 180° rotation about the normal to K_1 (i.e. a reflection on a plane perpendicular to (100)) (Fig. 5.1c). The latter symmetry operation is mechanically not relevant because the indices of this element are caused by the monoclinic symmetry of jadeite being irrational. If the first rotation axis is the [001] direction, the second one is approximately [201].

Kollé and Blacic (1982) studied (100) twin boundaries in clinopyroxenes by transmission electron microscopy (TEM). In many cases they observed that one boundary of a twin contained dislocations causing a sutured appearance, while the opposite boundary of the same twin lamella was straight. Kirby and Christie (1977) proposed that these twinning dislocations are partial dislocations with a Burgers vector $b = \frac{1}{2}$ [001]. According to these authors, the absence of other dislocations and the restriction to twin boundaries indicates that these partials are necessary for twinning. Furthermore, Kirby and Christie (1977) observed dislocations with curved configurations in twin boundaries in experimentally deformed diopside, suggesting the operation of a pole mechanism. The pole mechanism is a possible source for twinning dislocations, similar to the Frank-Read source for unit dislocations, whereas twin nucleation occurs on a dislocation (referred to as the pole) intersecting the glide plane. Other twin-source mechanisms may also be involved, such as homogenous nucleation of twinning partials, which requires that the local stress at the nucleation site exceeds the theoretical twinning stress (Kollé and Blacic, 1982).

In their experimental study using a Griggs type solid medium apparatus, Kollé and Blacic (1982) have found a critical resolved shear stress (CRSS) of 140 ± 10 MPa for twinning of hedenbergite and of 100 ± 30 MPa for chrome diopside. The authors suspect that numerous mineral inclusions as well as (001) growth twins in their chrome diopside sample account for the lower CRSS value and a larger scatter in the data. They conclude that the CRSS of 140 ± 10 MPa determined for hedenbergite represent a reasonable value for the twinning stress in clinopyroxene and that the composition of pyroxene does not notably affect the CRSS. The absolute values have to be taken with care, as e.g. Hacker and Kirby (1993) have shown that in a Griggs type apparatus with a salt pressure medium about one-half of the apparent sample strength may result from frictional and viscous losses. Thus, the above value for the CRSS may be overestimated. However, no deformation twins have been observed in fine- to medium-grained (ca. 10-20 μm and 200-500 μm) synthetic jadeite aggregates experimentally deformed using the molten salt cell technique at a differential stress of up to 240 MPa (Dorothee Dorner and Jens Orzol, pers. comm.). These preliminary results support a high CRSS for mechanical twinning of jadeite, with a minimum value similar to that proposed by Kollé and Blacic (1982). Thus, 140 ± 10 MPa is taken as an approximate value for the CRSS of jadeite twinning, bearing in mind that the inferred differential stresses can readily be adapted as soon as a more precise determination of the CRSS is available.

5.3. Sample description

The mechanical twinning of jadeite was examined in five samples from the lower Aosta valley: Three metagranites from the quarry of Montestrutto (sample CT25, CT30, CT110), one metagranite ca. 2.5 km from the quarry (CT8) and one metaaplite about 500 m from the quarry (CT20).

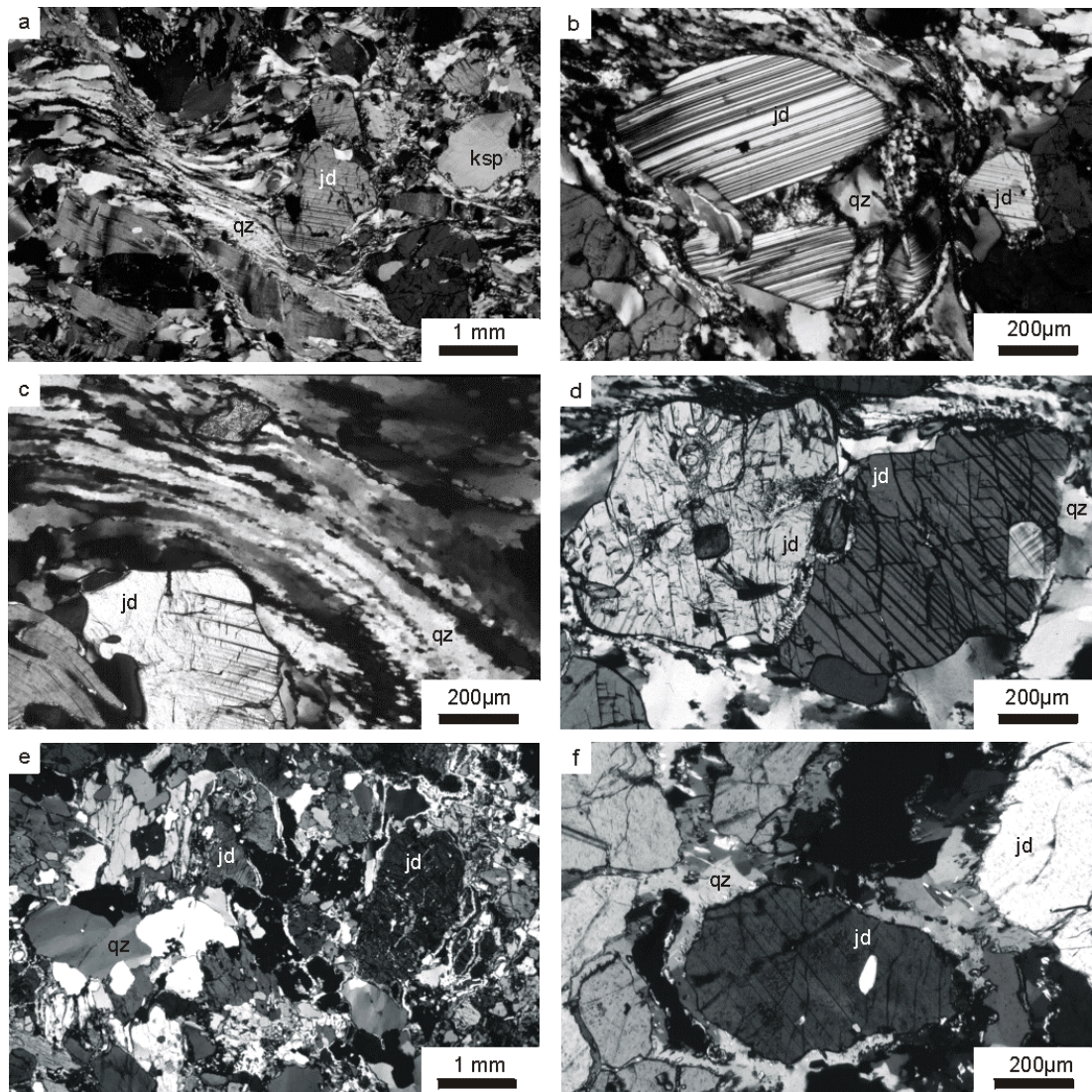


Fig. 5.2: Optical images taken with crossed polars. **Fig. 5.2a:** Microstructure of metagranite (sample CT25). Quartz reveals intense deformation by dislocation creep with variable recrystallised grain size, down to $5\mu\text{m}$ at sites of stress concentration close to rigid K-feldspar or jadeite crystals. **Fig. 5.2b:** Jadeite crystals in a metagranite (sample CT25) reveal fine (100) twin lamellae and undulatory extinction due to inhomogeneous crystal plastic deformation by dislocation glide on (100). **Fig. 5.2c:** Jadeite crystal in recrystallised quartz matrix. The (100) twin lamellae are wedge-shaped and end within the crystal (sample CT25). **Fig. 5.2d:** Jadeite crystals with contrasting twin densities in a mylonitic metagranite (sample CT30). **Fig. 5.2e:** Microstructure of jadeitite (sample CT20). Quartz is only slightly deformed, with jadeite forming a stress supporting framework. **Fig. 5.2f:** Fine (100) twin lamellae in a jadeite crystal of a jadeitite (sample CT20).

The metagranites (samples CT25, CT30, CT110, CT8) are characterised by a prominent foliation and an inconspicuous lineation. The Alpine high pressure paragenesis of these rocks comprises K-feldspar (ca. 20%), quartz (30–40%), phengite (20%) and jadeite (ca. 15%) \pm apatite \pm zircon. The jadeite composition has been determined by microprobe (see Appendix Table 2) and comprises 89 to 95% jadeite, 2 to 4% diopside and 3 to 8 % acmite. The quartz matrix reveals dynamic recrystallisation, with significant gradients in recrystallised grain size down to ca. $5\mu\text{m}$, or even below, at sites of intense deformation between rigid clasts of jadeite and K-feldspar (Fig. 5.2a, c). These gradients are thought to reflect stress concentrations between the rigid clasts. The mylonitic metagranites show a microstructure

characteristic of the "clast-matrix" field in the classification proposed by Handy (1990). Quartz forms the interconnected weak phase, whereas K-feldspar and jadeite are the strong clasts. In terms of material science nomenclature the rocks represent a particulate composite (e.g. Clyne and Withers, 1993) with near-isometric particles of jadeite and K-feldspar, as a first approximation, uniformly distributed in a quartz and phengite matrix.

A large portion of the jadeite crystals (ca. 40 %) reveal lamellar (100) twins (Fig. 5.2a-d), all showing features indicative of a mechanical origin, while (001) twins have not been observed (Table 5.1). The thickness of the lamellae is 2-25 μm (Figs. 5.2b and 5.3), with perfectly planar boundaries on the optical scale. Some are wedge-shaped, with a small angle, and terminate within the crystal (Fig. 5.2c). These crystals are slightly bent and show undulatory extinction.

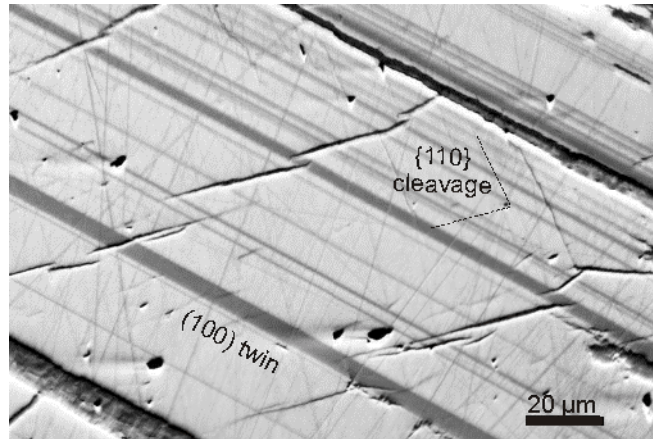


Fig. 5.3: Orientation contrast image (OCI) of a twinned jadeite crystal (sample CT110), revealing (100) lamellae of variable thickness down to ca. one micron and {110} cleavage.

This indicates the presence of geometrically necessary dislocations after inhomogeneous deformation by dislocation glide on (100). The twin density is highly variable (Fig. 5.2d), reaching up to ca. 300 mm^{-1} .

sample	modal % of jadeite	% twinned jadeite	twin lamellae per mm, normal to (100)	magnitude of differential stress
CT20	80%	15%	up to 70 mm^{-1}	0.5 GPa
CT25	15%	45%	up to 250 mm^{-1}	1.1 GPa
CT30	15%	55%	up to 200 mm^{-1}	1.2 GPa
CT110	10%	55%	up to 300 mm^{-1}	1.3 GPa
CT8	15%	60%	up to 170 mm^{-1}	2.0 GPa

Table 5.1: Microstructure and magnitude of differential stress, assuming a homogenous stress field on the sample scale and a CRSS of 140 MPa for twinning (see text for discussion).

The modal composition of the jadeite gneiss (CT20) is ca. 80% jadeite, 10% phengite and 10% quartz. The clinopyroxene composition is 82-90% jadeite, 5-10% diopside and 4-8% acmite (see Appendix B, Table 2). The jadeite is partly transformed into rims of albite, white mica and sodic-calcic amphibole. In contrast to the metagranites, the jadeite gneiss is represented by the polymineralic rock domain 1 of Handy's (1990) classification (see Fig. 5.2e, f). Jadeite forms a load-bearing framework that separates pockets filled with quartz. Accordingly, the interstitial quartz shows no pronounced deformation. In this rock type, only about 15 % of the jadeite crystals are slightly twinned, with a twin density of generally less than 70 mm^{-1} (Table 5.1). The twin lamellae are thin, rarely exceeding a few micrometres, and are of constant thickness (Fig. 5.2f).

5.4. Analytical results

5.4.1. Orientation distribution of jadeite crystals

The crystallographic orientation of twinned and untwinned jadeite crystals was measured in five sample with both universal stage and EBSD (Fig. 5.4).

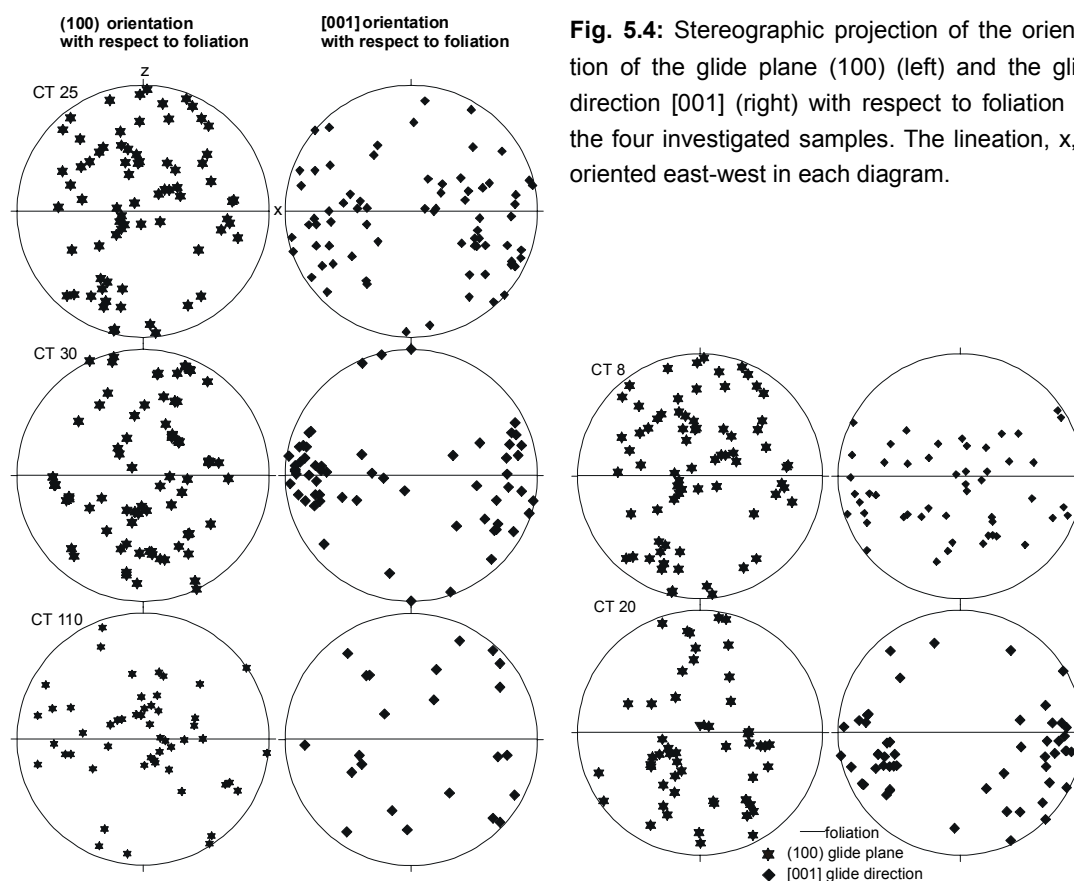


Fig. 5.4: Stereographic projection of the orientation of the glide plane (100) (left) and the glide direction [001] (right) with respect to foliation for the four investigated samples. The lineation, x, is oriented east-west in each diagram.

A weak crystallographic preferred orientation (CPO) is evident, with the normal to (100) defining an ill-defined girdle around the stretching lineation X. The $\langle c \rangle$ axes [001] show a somewhat more conspicuous maximum parallel to X. The [001] maximum is best defined in the granite gneiss sample CT30, whereas the (100) girdle is better developed in the metaaplite sample CT20. Godard and van Roermund (1995) discussed the processes leading to a crystallographic preferred orientation during plastic deformation of clinopyroxenes. They conclude, that the patterns are not easily explained by dislocation glide or twinning alone. The isolated jadeite crystals in the granite gneiss sample examined in this study show no evidence of dislocation glide that could have produced sufficient strain and a related CPO. The same holds true for the metaaplite, although some high temperature plastic flow of the aggregate cannot be excluded. It is possible that the observed jadeite CPO patterns were inherited from the CPO of another phase developed in a preceding metamorphic stage, which may have resulted in the preferred orientation of jadeite during nucleation. The present CPO, which is exclusively measured for the host crystals, is not affected by mechanical twinning. However, the CPO pattern is sufficiently diffuse to allow the determination of stress

field orientation and magnitude of differential stress from the orientation distribution of the twinned crystals.

5.4.2. Orientation of the principal stress directions

Application of the dynamic analysis of Raleigh and Talbot (1967) implies that twinning took place in crystals where the resolved shear stress on the (100) twin glide plane in the η_1 direction exceeded the critical value. Within a given stress field, the most favourable orientation for twinning on (100) is such that the major principal stress direction σ_1 must be at 45° to (100) and [001], with an angle of 27.4° to the $\langle a \rangle$ axis, and the least principal stress direction σ_3 must be at an angle of 62.6° to the $\langle a \rangle$ axis (Fig. 5.1c).

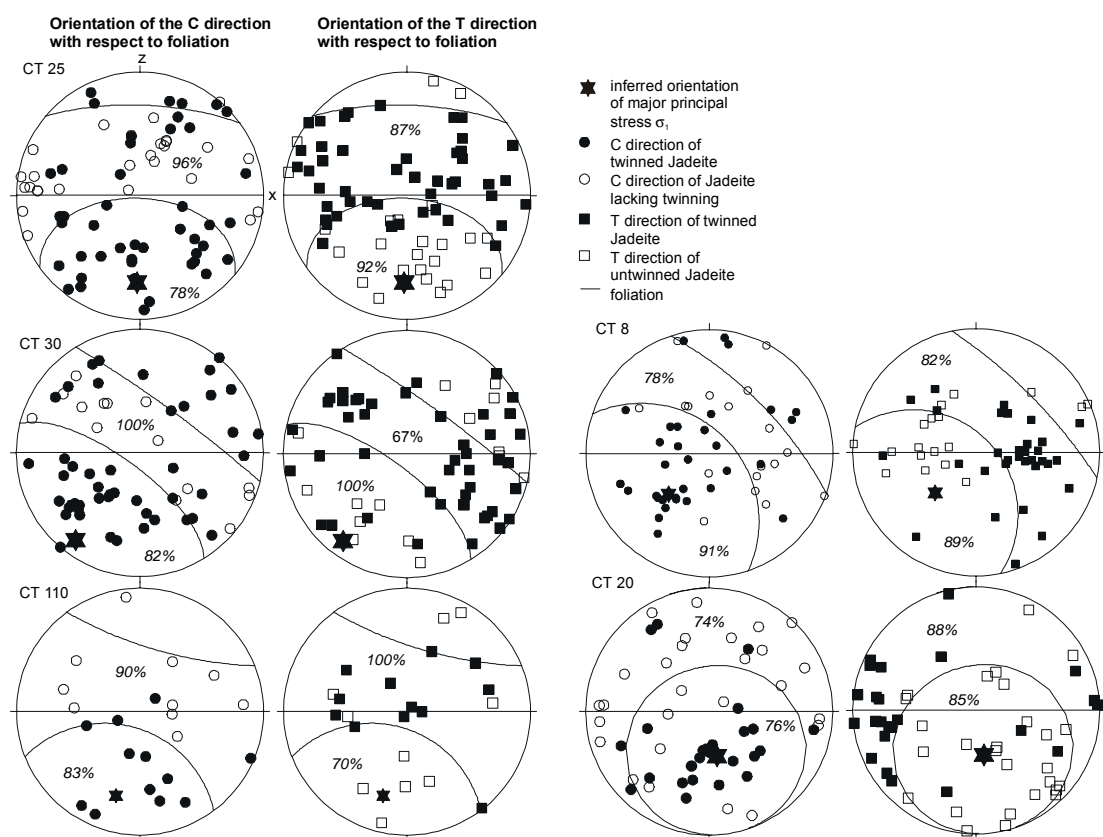


Fig. 5.5: Stereographic projection showing the orientation of twinned and untwinned jadeite crystals, given as C (left) and T (right). The lineation is oriented east-west. The majority of the C orientations of twinned (76-83%, as indicated in the diagrams) and T orientations of untwinned (70-100%) jadeite crystals plot inside a small circle. In contrast, the majority of the C orientations of untwinned (74-100%) and T orientations of twinned (67-100%) jadeite crystals plot outside this small circle. As a first approximation, the centre of this small circle is taken to represent the σ_1 direction at the time of twinning, referred to as σ_1' .

According to Raleigh and Talbot (1967) these orientations are termed C for the direction of compression corresponding to σ_1 , and T for the direction of tension corresponding to σ_3 , respectively. For each crystal, these directions C and T can be constructed and plotted stereographically (Fig. 5.5). Within this diagram, a small circle is visually adapted that circumscribes a maximum of C orientations of twinned and T orientations of untwinned jadeite crystals.

tals. In contrast, the majority of the C orientations of untwinned and T orientations of twinned jadeite crystals plot outside (see Fig. 5.5). In principle, the method corresponds to that proposed by Angelier and Mechler (1977) for the inversion of fault slip data. Choosing any other diameter and position of the small circle enlarges the number of C orientations of untwinned jadeite crystals and the T orientations of twinned jadeite crystals within the small circle, and the other way round outside the small circle. The resulting pattern is similar to that found by Raleigh and Talbot (1967, p. 161) for experimentally and naturally deformed diopside. The centre of the small circle is taken to represent approximately the direction of the major principal stress direction σ_1' at the time of twinning. In Fig. 5.6, the derived σ_1' directions for each sample are displayed with respect to geographic coordinates. It is evident that the orientation is similar in each of the three sample from the quarry of Montestrutto. This finding implies that the sample record the orientation of a stress field, uniform at the scale of hundreds of metres.

5.4.3. Paleopiezometry

Using the inferred σ_1' direction as a reference, the magnitude of differential stress can be derived from the orientation distribution of twinned and untwinned crystals. The Schmid formula yields the resolved shear stress as a function of differential stress and orientation of the glide-plane and glide-direction. For each mechanically twinned jadeite crystal, the resolved shear stress on (100) in direction [001] must have exceeded the CRSS; here the value of 140 ± 10 MPa is used. It follows that the minimum differential stress at the instant of twinning can be derived by the following equation for each individual crystal.

$$\sigma_{\text{res}} = (\sigma_1 - \sigma_3)(\cos\gamma \cdot \cos\theta) \quad (5.1)$$

$$\Leftrightarrow (\sigma_1 - \sigma_3) = 140 \text{ MPa} / (\cos\gamma \cdot \cos\theta) \quad (5.2)$$

where γ is the angle between the inferred σ_1' direction and the normal to the (100) plane and θ the angle between σ_1' and [001].

It is presumed that twinning occurred where the critical shear stress was reached and that untwinned jadeite crystals were not suitably orientated within the stress field to twin. This means that either twinning was not possible because σ_1 was at an obtuse angle between (100) and the $\langle a \rangle$ -axis, or that the resolved shear stress was not sufficient. Using this method, a surprisingly uniform high magnitude of differential stress between 1.1 to 1.3 GPa is derived for the sample CT25, CT30, and CT110 (Table 5.1). The other metagranite (CT 8) records an unrealistic high value for the differential stress of 2 GPa. For the metaaplite, in which jadeite forms a stress-supporting framework and interstitial quartz shows no pronounced deformation and recrystallisation, the derived differential stress is only 0.5 GPa. In all cases, small variations in the position of the small circle do not affect the result.

5.5. Discussion

The orientation distribution plots (Fig. 5.5) show that the boundary between the fields of twinned or untwinned jadeite crystals is not sharp. Also, in all samples a few jadeite crystals are twinned, even though their orientation should not have permitted twinning within the inferred stress field. The same type of scatter was found by Raleigh and Talbot (1967) in experimentally deformed diopside. However, the general pattern is consistent in each sample and the derived σ_1' directions (in geographic coordinates, Fig. 5.6) are similar for each of the three metagranite-sample of the quarry of Montestrutto taken from an area of about 50 m across.

This suggests that a stress field on the mesoscopic-scale (up to 10^2 m) is recorded.

The inferred σ_1' direction for the other metagranite (CT8) taken at a distance of about 2.5 km from the Montestrutto metagranites and the metaaplite sample (CT20), located about 0.5 km from the quarry, deviates significantly from that found in the metagranites.

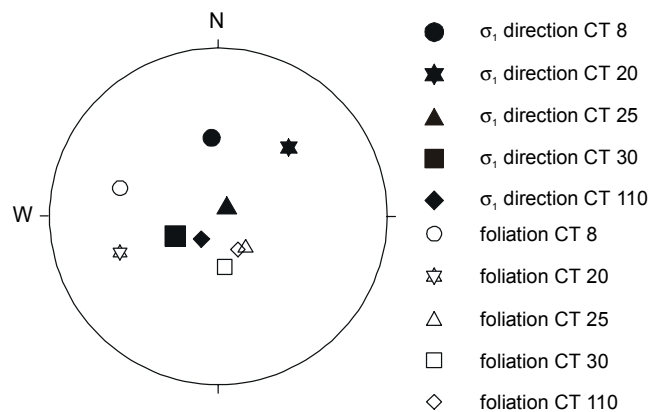


Fig. 5.6: Plot of the inferred σ_1' direction of the four samples with respect to geographic coordinates.

Notwithstanding the low number of data, this indicates an inhomogeneous stress field on the km scale, or rotation following deformation. Such an inhomogeneous stress field may be related to both the inferred mode of loading at the lower termination of a major seismogenic fault zone and to the structural and lithologic heterogeneity within large-scale folds.

The overlap in the orientation distribution of twinned and untwinned jadeite crystals in an individual sample can be attributed to several factors that are discussed below:

- (1) The metagranites constitute a polyphase material with contrasting mechanical properties of the individual phases. Near-isometric strong particles of jadeite are embedded in a weaker matrix of quartz. For such particulate composites (e.g. Clyne and Withers, 1993) external loading induces an inhomogeneous internal stress field (e.g. Brockenbrough et al., 1991; Ji and Zhao, 1994; Handy, 1990; Kenkmann and Dresen, 1998) with curved stress trajectories and sites of stress concentration. The mechanical twinning of each individual crystal is bound to the local state of stress and as such a sharply bounded orientation distribution within a volume comprising a large number of grains cannot be expected.
- (2) Load transfer between the ductile quartz matrix and the rigid jadeite crystals could be expected to lead to stress concentration in the jadeite crystals (e.g. Ji and Zhao, 1994). Even a small amount of matrix plasticity can cause a relatively high misfit, causing significant load transfer to the inclusions (Clyne and Withers, 1993). This effect depends on interface coupling, which in turn is subject to modification during progressive deformation (e.g. Kenkmann and Dresen, 1998). Thus, the local stress field is a complex function of position as well as shape mismatch. The effect may be particularly strong if rapid loading precludes efficient stress relaxation in the matrix and strain hardening.

- (3) Although bulk strain is moderate and grain shape of the jadeite crystals is nearly isometric, minor rotation of the crystals in the flowing matrix (e.g. Fig. 5.2 a-d) may have taken place subsequent to twinning. Such rotation could have affected the orientation distribution.
- (4) Twinning could have been achieved during several increments of variable stress field orientation and/or intermittent reorientation of the crystals in a flowing matrix.

The uniform orientation of the stress field inferred from the orientation distribution of twinned and untwinned jadeite in several separate sample (Fig. 5.6) implies that the uncertainties related to points (1) through (4) outlined above do not pose severe limitations to the reconstruction of the principal stress directions. Also, the symmetry of the orientation distribution rules out effects related to point (4). However, derivation of differential stress from the orientation distribution does not appear to be straightforward for a polyphase material with twinned clasts in a weaker matrix. It is most probable that the extreme values of differential stress $\sigma_1 - \sigma_3$ on the order of 1-2 GPa inferred from the relative orientation of twinned jadeite crystals in the metagranites result from the inhomogeneous stress field, stress concentration, and rotation of crystals subsequent to twinning. Presently there is no realistic approach to assess these effects in a natural material with a complex history. The lack of access to the third dimension in an ordinary thin section poses further constraints, as the effect of the out of plane phase distribution on the local stress field cannot be neglected.

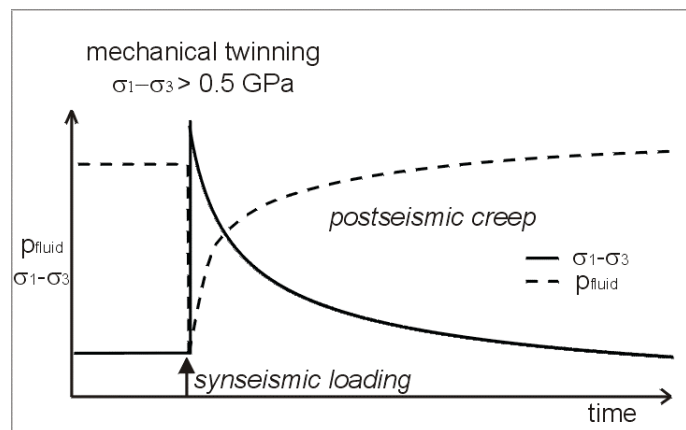
In contrast, the situation appears to be somewhat more promising for the metaaplite (sample CT20). To a first approximation, jadeite forms a load-bearing framework with weak quartz pockets (Handy, 1994). As discussed by Ji and Zhao (1994), such materials can be treated as analogous to a porous medium following a model proposed by Tharp (1983), if the volume fraction of the strong phase exceeds about 75% and the strength contrast is high. In this case, stress concentration around isolated weak pockets and mechanical anisotropy of the load bearing phase are the major causes of an inhomogeneous stress field, with load transfer expected to be insignificant due to low strain. Furthermore, the low bulk strain compared to the metagranites (Fig. 5.2 e-f) precludes rotation of the jadeite crystals subsequent to twinning. Thus, the uncertainties related to point (1) in the above compilation are reduced in comparison to the metagranites, and those related to points (2) and (3) are probably insignificant. In fact, the boundary between the fields of twinned and untwinned jadeite crystals (Fig. 5.5) is better defined in the metaaplite, than in the metagranites. The differential stress derived from the orientation of twinned jadeite crystals with respect to σ_1' amounts to 0.5 GPa, i.e. less than 50 % of the extreme values found for the metagranites. The high stresses recorded by the twinned jadeite crystals may represent peak stresses reached for a short time during synseismic loading. Mechanical twinning is rate-independent, with an instantaneously developing and stable microstructural record. Thus, this mechanism is able to record such stress peaks.

5.6. Conclusions

The results from this chapter confirm that mechanical twinning of pyroxene in a polyphase rock can be used to infer the approximate orientation of the principal stress directions at the instant of deformation. However, it reveals that the use of mechanical twinning to derive the magnitude of a mesoscopic far-field differential stress is anything but straightforward in polyphase rocks. The diffuse boundary between the orientation fields of twinned and untwinned

crystals, and a few twinned crystals in forbidden orientations, are considered to result primarily from an inhomogeneous stress field with curved stress trajectories and from post-twinning rotation. Thus, the derived magnitude of differential stress in the metagranites of up to 2 GPa, assuming a CRSS of 140 MPa to hold for jadeite, is probably unrealistic, although a consistent value of about 1 GPa is obtained for the three individual sample from the quarry of Montestrutto. Remarkably, the sample with 80 vol. % jadeite forming a stress-supporting framework reveals a less diffuse boundary between the orientation fields of twinned and untwinned crystals, and a lower inferred magnitude of differential stress. This value of 0.5 GPa is close to the magnitude of 0.3 ± 0.1 GPa derived from independent paleopiezometers for the same stage of deformation in the same area (Küster and Stöckhert, 1999).

Fig. 5.7: Proposed model relating mechanical twinning of jadeite to synseismic loading and postseismic creep in the uppermost plastosphere, see text for discussion.



Thus, it is proposed that mechanical twinning of jadeite probably records peak stresses achieved during synseismic loading (Fig. 5.7), with an inhomogeneous stress field related to the mode of loading and structural complexity of the crust on the 10^2 to 10^3 m scale. The somewhat lower – but still very high - apparent stresses recorded by the quartz microstructures of the same rocks, with an inhomogeneous, relatively moderate strain, reflect non-steady state postseismic flow by dislocation creep with rapidly decaying strain rate due to stress relaxation (see Chapter 7).

6. Cataclastic deformation of garnet*

6.1. Introduction

In some micaschist, crystals of the high strength mineral garnet embedded in a quartz matrix are intensely fragmented. Their microstructures mainly characterised by closely spaced sub-parallel fractures are markedly different from those of fragmented garnet described elsewhere in the geological literature (e.g. Valentino and Sclar, 1981; Prior, 1993; Ji et al. 1997; Wang and Ji, 1999; Wendt et al., 1993; Whitney, 1996, 2000). In this chapter a detailed optical, EMP and SEM analysis, combined with EBSD techniques of these fragmented garnet crystals is presented. The implications of the microstructural record for synseismic loading, postseismic creep and related changes of pore fluid pressure in the uppermost plastosphere is discussed.

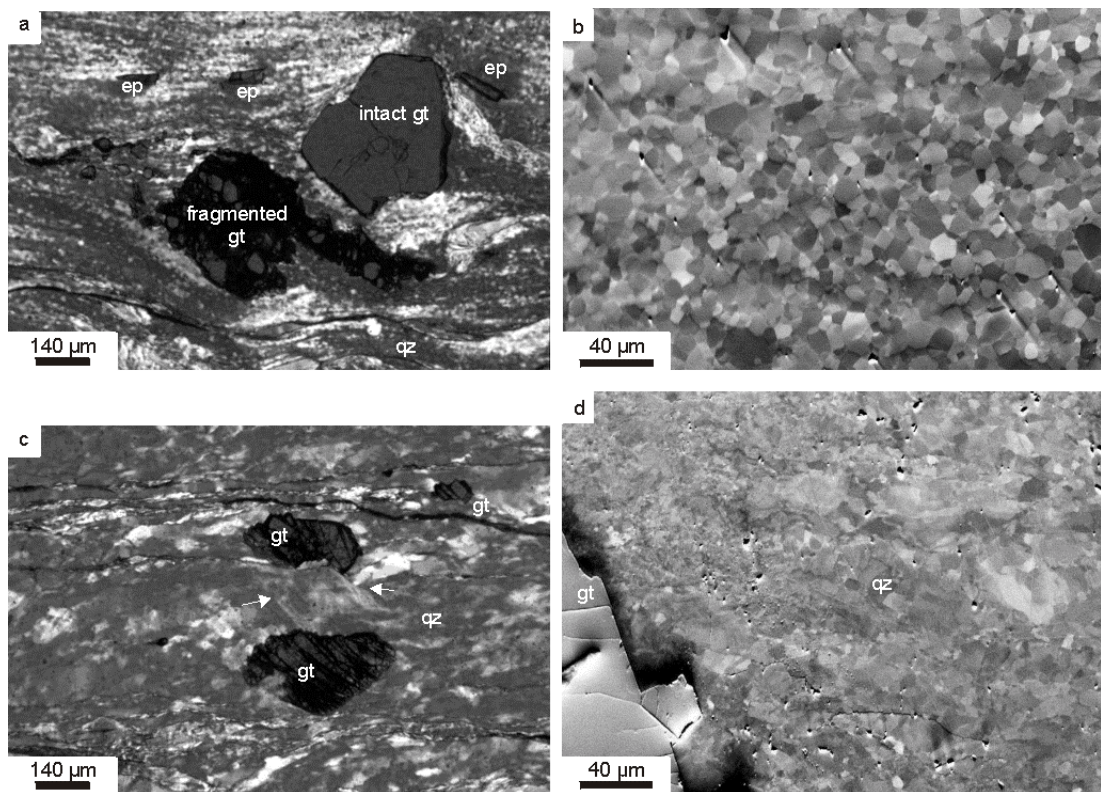


Fig. 6.1a: Optical micrograph showing one fragmented and one intact garnet embedded in a quartz matrix, mylonite sample St12, crossed polars and Red I compensator inserted. Small particles in the quartz matrix are epidote. **Fig. 6.1b:** OC-image of fine-grained quartz matrix, mylonite sample St12. **Fig. 6.1c:** Optical micrograph showing fragmented garnets embedded in a quartz matrix, with deformation lamellae parallel to fractures in garnet (arrows), sample CT183, crossed polars and Red I compensator. **Fig. 6.1d:** OC-image of the inhomogeneous quartz microstructure of sample CT183.

*The results presented in this chapter are published in:

Trepmann C.A., Stöckhert B. (2002) Cataclastic deformation of garnet: A record of synseismic loading and postseismic creep. *J. Struct. Geol.* 24: 1845-1856.

6.2. Sample description

Two samples of mylonitic micaschist from the lower Aosta valley were chosen for detailed analysis (sample CT183 and sample St12), each with a slightly different microstructural record of fragmented garnet. For a general sample description see Chapter 4.2. Sample St12 is from a high strain mylonite zone and shows a prominent foliation and lineation, while sample CT183 is less deformed with no conspicuous lineation. The quartz matrix of the sample St12 reveals pervasive dynamic recrystallisation with a grain size down to about 5 μm (Fig. 6.1a, b), isometric grain shape and plane or simply curved grain boundaries, indicating that grain growth has affected the microstructure (Fig. 6.1b). In contrast, sample CT183 shows a highly heterogeneous quartz microstructure (Fig. 6.1c, d) with marked gradients in the recrystallised grain size, that can be well below 5 μm at sites of stress concentration, but with large grains preserved elsewhere with prominent undulatory extinction and in places abundant deformation lamellae (see Chapter 7).

6.3. Garnet microstructure

The microstructural characteristics of garnet in the two investigated samples (St12, CT183) are described in the following paragraphs. In both samples, the garnet crystals are embedded in a quartz and mica matrix (Figs. 6.1a,c and 6.2a-d). The majority (80-90%) of the garnet crystals show intense fragmentation, although a few crystals remain intact (Fig. 6.1a).

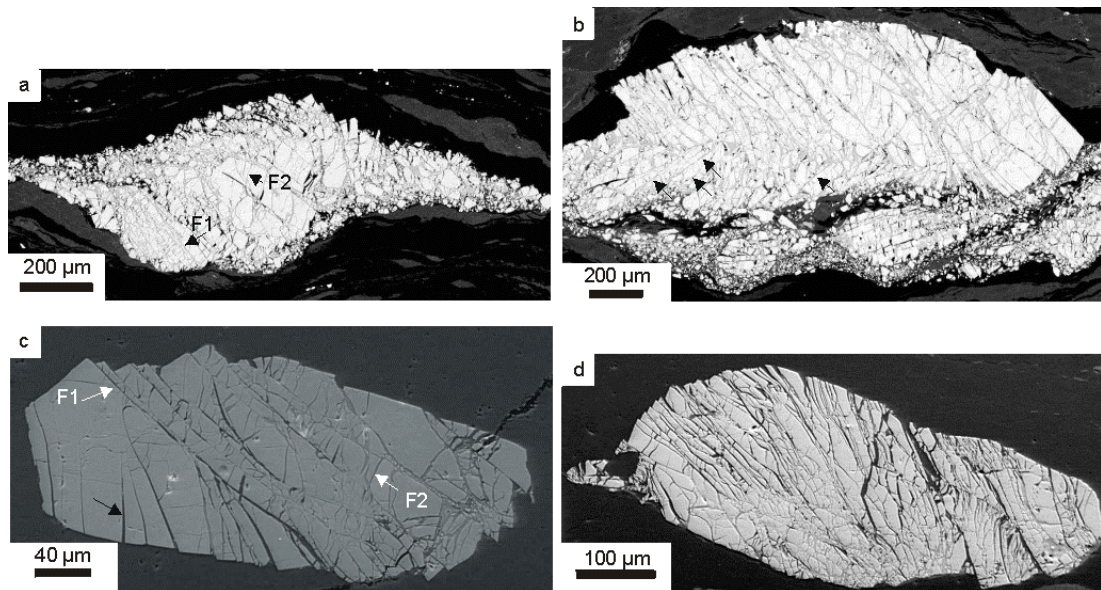


Fig. 6.2a: SE-image of cataclastic garnet with F1 and F2 fractures, mylonite sample St12. **Fig. 6.2b:** SE-image of cataclastic garnet with a second set of F1 fracture (arrows), mylonite sample St12. **Fig. 6.2c:** SE-image of cataclastic garnet showing F1 and F2 fractures (white arrows) and fractures oriented at a low angle to the shortening direction, terminating inside the grain (black arrow), sample CT183. **Fig. 6.2d:** SE-images of cataclastic garnet in sample CT183.

Two sets of microcracks are typically found in the fragmented garnet crystals. The first set, referred to as F1, is made up by pervasive plane or slightly curved, discontinuous, transgranular (Kranz, 1983) cracks (Fig. 6.2a-d). The orientation of F1 cracks is oblique to foliation and the direction of maximum shortening (Fig. 6.2a-d). In rare cases, fractures oriented almost perpendicular to foliation terminate within the grain (Fig. 6.2c). The second set of microcracks, referred to as F2, is made up of shorter fractures oriented at a high angle to the F1 fractures and abutting against them (Fig. 6.2a-d).

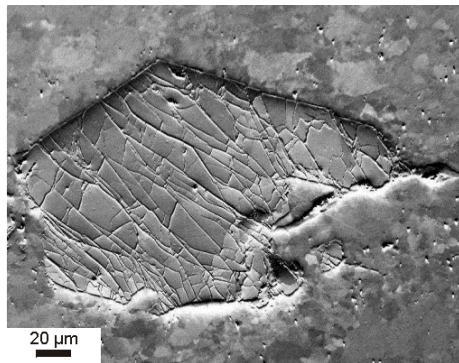


Fig. 6.3: OC-image of a fragmented garnet in sample CT183, showing no displacement parallel to the fracture planes.

This indicates that the F2 fractures developed after the F1 fractures. Typically, the fragments are displaced by some μm predominantly along the F1 fractures (Figs. 6.1a,c and 6.2a-d). Notably, a few intensely cracked garnet crystals remain undistorted (Fig. 6.3). The microcracks are generally restricted to the garnet crystals and a propagation into the surrounding matrix is not evident. In places, transgranular F1 fractures appear to be continuous with shear bands, revealing an apparent offset (possibly healed cracks), or deformation lamellae in the adjacent quartz matrix (Fig. 6.1c).

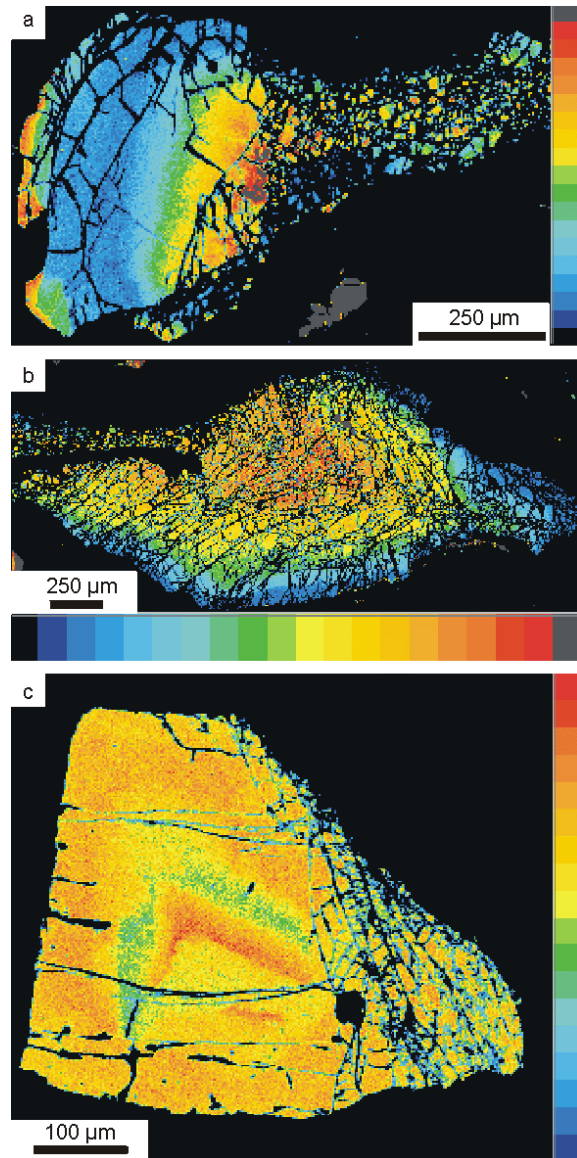


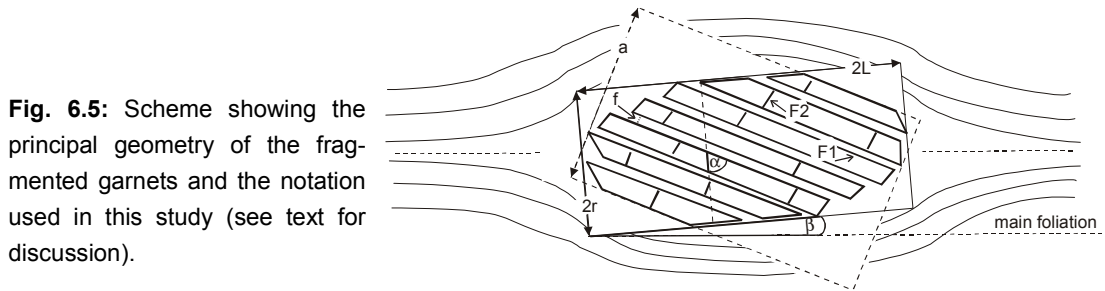
Fig. 6.4: Element distribution patterns (Calcium) of garnet. **Fig. 6.4a:** Partly fragmented garnet in mylonite sample St12. **Fig. 6.4b:** Concentric compositional zoning of a cataclastic garnet in mylonite sample St12. **Fig. 6.4c:** Oscillatory compositional zoning of a partly fragmented garnet in sample CT183.

Electron microprobe data (see Appendix B, Table 3) reveal a concentric, sometimes complex and partly oscillatory zoning (Fig. 6.4) of garnet with compositions in the range of almandine 73-50%, grossular 35-17%, pyrope 8-4%, spessartine 4-3 %. Within the limits of spatial resolution, the chemical composition is not modified along the fractures, indicating that

chemical reactions did not occur during or after fragmentation (Fig. 6.4). Inclusions of apatite, ilmenite, mica, K-feldspar, and quartz in garnet are rare. There appears to be no correlation between fragmentation and garnet composition, compositional zoning or presence of inclusions.

6.3.1. Fracture pattern and geometry of fragmented garnet

The geometric characteristics of fragmented and deformed garnet in sample CT183 are described by the following parameters (Fig. 6.5), determined by optical microscopy.



- (1) The long axis ($2L$), corresponding to the maximum diameter of the garnet.
- (2) The short axis ($2r$), corresponding to the maximum diameter of the garnet normal to the long axis.
- (3) The angle (β) between the long axis of the garnet and the foliation beyond the local perturbation caused by the garnet.
- (4) The orientation of F1 microcracks, described by the mean angle (α) between the fracture plane and the short axis of the garnet.
- (5) The fracture density (n/a), measured as the number of F1 fractures normalised to the length a perpendicular to the F1 fracture
- (6) The typical width of opening of the cracks (f), measured normal to the crack.

From these parameters the aspect ratio s , the grain size d , and the distance a (Fig. 6.5) were calculated as follows:

$$s = L/r \quad (6.1)$$

$$d = 2(L \cdot r)^{1/2} \quad (6.2)$$

$$a = 2L \cdot \cos(\alpha) \quad (6.3)$$

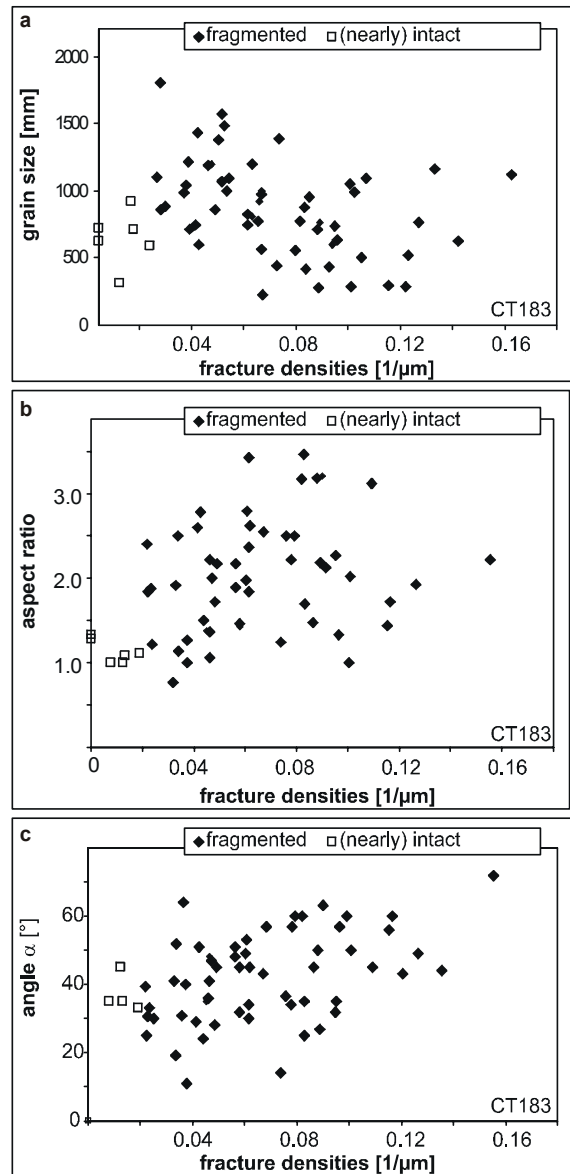
The grain size of garnet ranges from 0.2 mm to 2.4 mm with an average of 0.8 mm and shows no correlation with density of F1 fractures n/a (Fig. 6.6a). Fragmented garnets show a relatively high aspect ratio ($s = 2.0$, on average, with extremes of 1.0 to 3.5, Fig. 6.6b). In contrast, intact garnets reveal a low aspect ratio of 1.3 on average.

The angle β between the long axis of the fragmented garnets and the foliation is typically between 0° and 20° . The angle α (Fig. 6.5) is 42° on average, with extremes of 10° and 72° , respectively (Fig. 6.6c). There appears to be neither a correlation between the fracture density n/a and the grain size, nor to the aspect ratio or to the angle α (Fig. 6.6a, b, c).

However, stereological effects cannot be ruled out, as small garnets with high fracture densities may represent near-rim sections through larger garnets. The fracture-normal displacement along dilatant fractures (f) is about $1.5 \mu\text{m}$ on average, with extremes of 0.2 and $5 \mu\text{m}$ (Figs. 6.2a-d and 6.7b), as seen in the SEM. These opened cracks are filled with quartz and feldspar. In general dilation is small and uniform (cf. Figs. 6.2c,d, 6.3, and 6.7b) and the fragments reveal a high degree of fitting.

In contrast to sample CT183, the garnet fragments in the high strain mylonite St12 are widely separated and have undergone significant rotation, where they form continuous thin layers or streaks parallel to the mylonitic foliation (cf. Figs. 6.2a,b, and 6.4a,b).

Fig. 6.6a: Plot of the grain size of garnet versus F1 fracture density (n/a) (sample CT183). **Fig. 6.6b:** Plot of the aspect ratio of garnet versus F1 fracture density (n/a) (sample CT183). **Fig. 6.6c:** Plot of the angle α versus F1 fracture density (n/a) (sample CT183).



In some of these garnets the F1 fractures form a conjugate system with angles α of between 20 and 70° , and between 100 and 170° , respectively. Some large garnets show two sets of F1 fractures at an angle of about 90° (cf. Figs. 6.2b, 6.4b, 6.7a, and 6.8c).

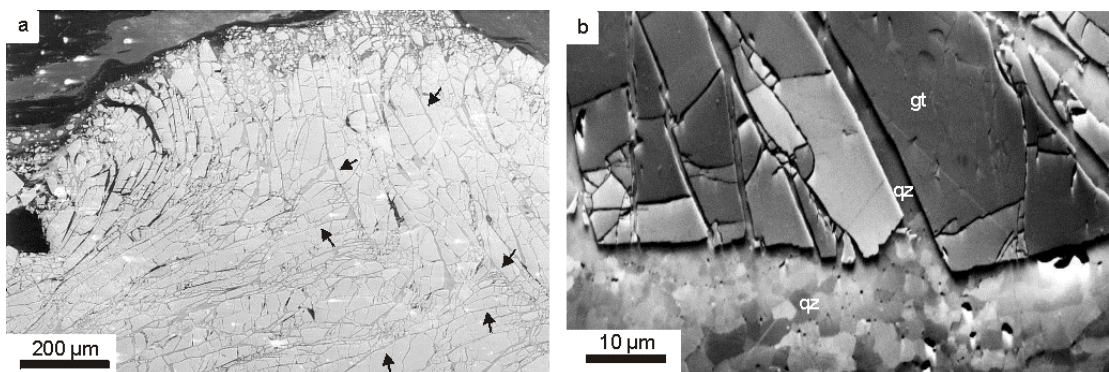


Fig. 6.7a: SE-image of a fragmented garnet in mylonite sample St12, revealing two domains with F1 fractures at a high angle to each other (arrows). **Fig. 6.7b:** OC-image of fragmented garnet in sample CT183; open cracks are sealed with quartz and feldspar.

6.3.2. Crystallographic orientation

The crystallographic orientation of fragmented and disintegrated garnet was studied to examine rotation of fragments during deformation, crystallographic control on crack orientation, the influence of pre-existing low angle grain boundaries (LAGB) on fracture location, and potential effects of crystallographic orientation on brittle strength.

First, the OC-images (Figs. 6.3 and 6.7b) show that a crystallographic misorientation between the individual fragments is common for the fragmented garnets, while the crystallographic orientation is rather uniform within an individual fragment. In a detailed inspection, the crystallographic orientation of 63 garnets of sample CT183 and of 10 garnets of mylonite sample St12 were analysed with the EBSD-technique.

The crystallographic misorientation between neighbouring fragments is typically between 5 and 10°, as shown by the relative frequency of neighbour-pair misorientation angles (Fig. 6.8a-c). However misorientations of up to 30° were found in sample CT183 and of up to 40° in the mylonite sample St12. Some of the higher values obtained by the automatic measurements may be due to misindexing. The misorientation profile in Fig. 6.8b shows that the magnitude of cumulative misorientation increases progressively across the disintegrated grain. Most non-neighbour, randomly selected pairs from garnets in sample CT183 reveal misorientations of typically about 10-15° (Fig. 6.8a, b). In contrast, the relative frequency of misorientation angles of randomly selected pairs from large garnets in the mylonite sample St12, with two sets of F1 fractures (Figs. 6.2b, 6.4b, and 6.7a), reveals a maximum at about 45-50° (Fig. 6.8c). The contrast between the random-pair and the neighbour-pair misorientation distribution, which can be quantified by the Kolmogorov-Smirnov test (Wheeler et al., 2001) is visualised in Fig. 6.9. This shows that the highest degree of fragmentation and disintegration (Fig. 6.8c, compare Fig. 6.4b) correlates with the largest difference between the two misorientation distributions.

In 65% of the investigated cases the crystallographic orientations of the fragments are observed to be dispersed around one axis, as shown in the stereographic plots (Figs. 6.8b,c and 6.10). This dispersion axis is defined by the maximum density of the orientation distribution of the misorientation axes (Fig. 6.10c). Furthermore, for nearly 50 % of the investigated cases the dispersion axis plots within a few degrees of a crystallographic axis: 25% near to <100> (e.g. Fig. 6.10b); 12% near to <110> and 12 % near to <111>. In contrast, the angle between the dispersion axis and the normal to the fracture plane varies from 14 to 90° and averages 63°.

The fractures do not follow rational planes, as can be seen by comparing the crystallographic orientation of the garnet fragments and the orientation of the F1 fracture plane (example in Fig. 6.10), measured with the universal stage on the optical microscope. In only 25% of the investigated cases are the normals to the fracture planes oriented near a crystallographic axis. In view of the high symmetry of garnet, this can be assumed to occur by chance. Also, no direct effect of a specific crystallographic orientation on the degree of fragmentation and disintegration was observed.

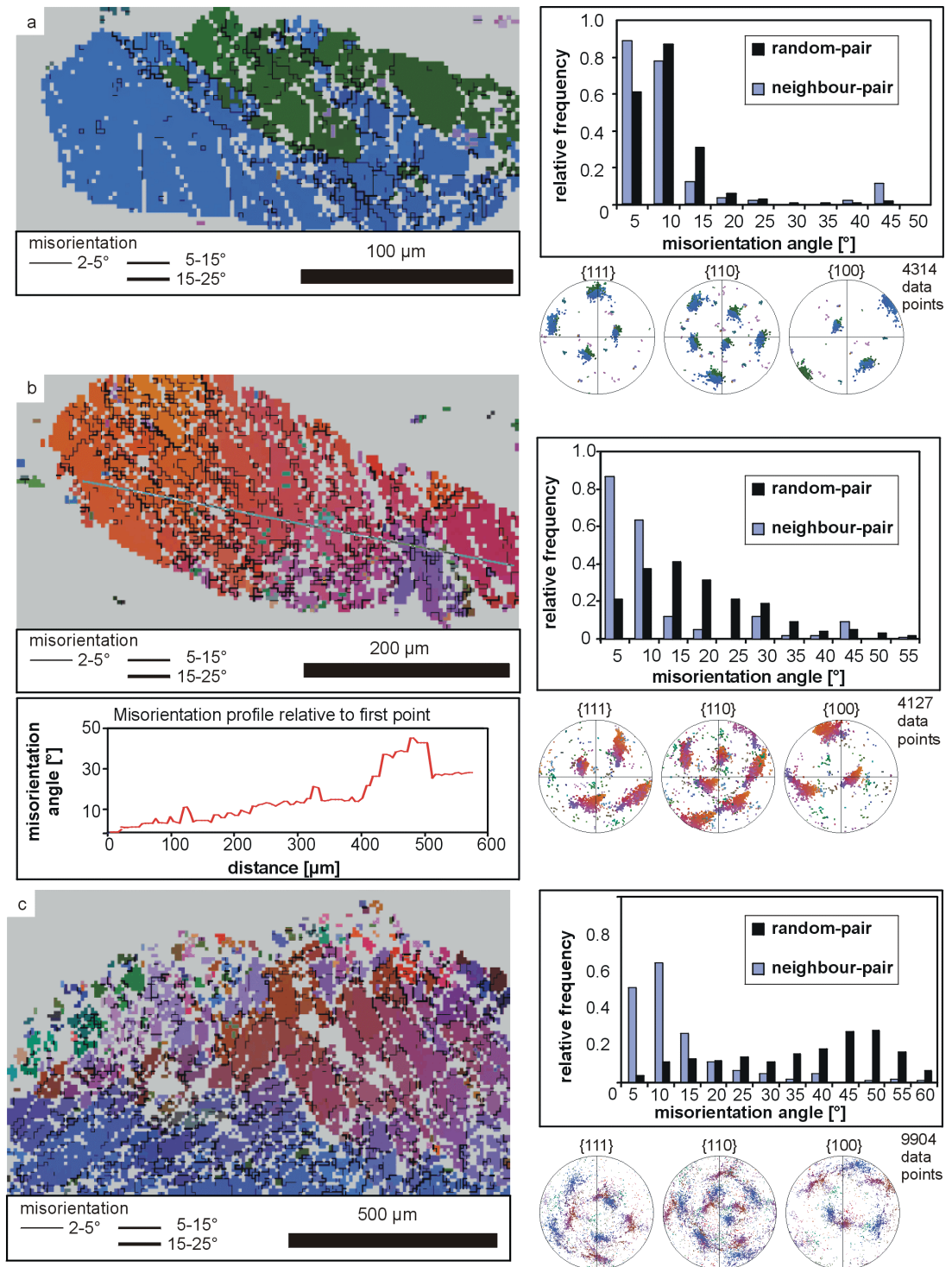
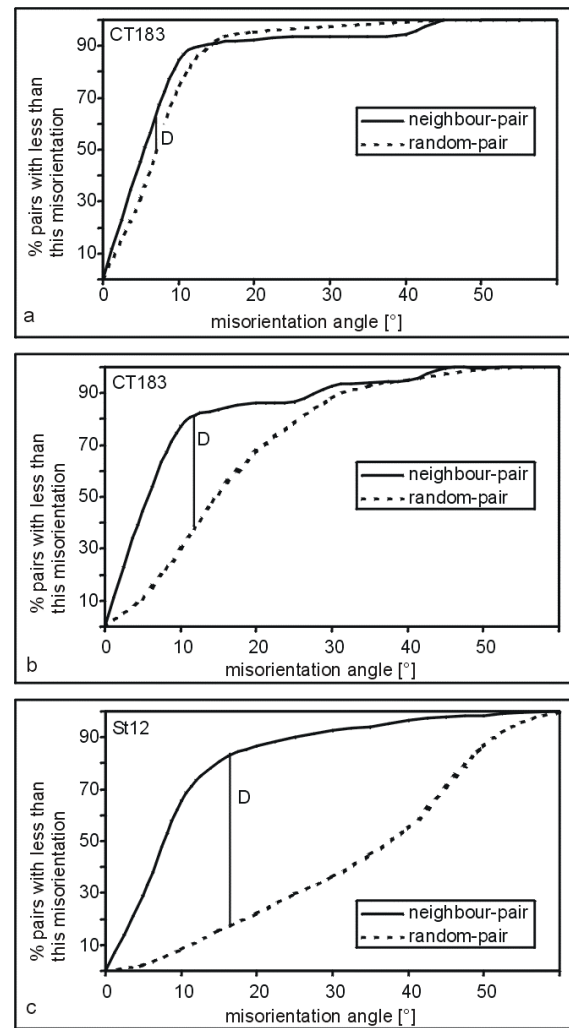


Fig. 6.8a: EBSD-map of fragmented and slightly disintegrated garnet in sample CT183 (compare Fig. 6.2c). Right: Histogram of the relative frequency of misorientation angles and stereographic plot of the crystallographic planes. **Fig. 6.8b:** EBSD-map of fragmented and disintegrated garnet in mylonite sample CT183. Bottom: Misorientation profile along the line in the EBSD-map. Right: histogram of the relative frequency of misorientation angles and stereographic plot of the crystallographic planes. **Fig. 6.8c:** EBSD-map of fragmented and strongly disintegrated garnet in mylonite sample St12 (compare Fig. 6.4b). Right: Histogram of the relative frequency of misorientation angles and stereographic plot of the crystallographic planes.

Fig. 6.9: Cumulative frequency diagrams showing neighbour-pair and random-pair misorientation distribution and illustrating the Kolomogrov-Smirnov test for significant differences (Wheeler et al., 2001). **Fig. 6.9a:** Lowest difference D in misorientation distribution in slightly disintegrated garnet from sample CT183, compare EBSD-map Fig. 6.8a. **Fig. 6.9b:** Difference D in misorientation distribution in moderately disintegrated garnet from sample CT183, compare EBSD-map Fig. 6.8b. **Fig. 6.9c:** Highest difference D in misorientation distribution in strongly disintegrated garnet from sample ST12, compare EBSD-map Fig. 6.8c.



Some undeformed garnet crystals display low angle grain boundaries (LAGB) with a small misorientation of $\leq 3^\circ$ (Fig. 6.11a, c). In a partly fragmented garnet crystal (Fig. 6.11a), a LAGB with a misorientation angle of $< 2^\circ$ grades into a microcrack with a crystallographic misorientation of up to 14° . The rotation axis for the misorientation across the LAGB is inclined to the fracture normal with an angle of about 60° , whereas the rotation axis for the crystallographic misorientation along the fracture is oriented at an angle of $85\text{--}89^\circ$, suggesting a twist geometry of displacement. There is no relation between the compositional zoning of the garnet and the domains of different crystallographic orientations (compare Figs. 6.4c and 6.11a).

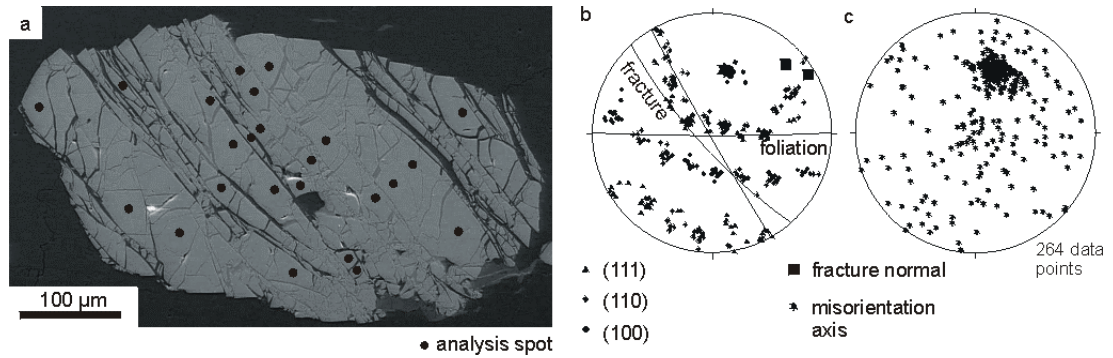


Fig. 6.10a: SE-image of a fragmented garnet with sites of manual EBSD measurements. **Fig. 6.10b:** Stereographic plot of the fracture planes, misorientation axes and crystallographic orientation of the garnet in (a). **Fig. 6.10c:** Stereographic plot of misorientation axes (calculated from EBSD measurements with the computer program StereoNett 2.0, Duyster, 1996), with the maximum density defining the dispersion axis.

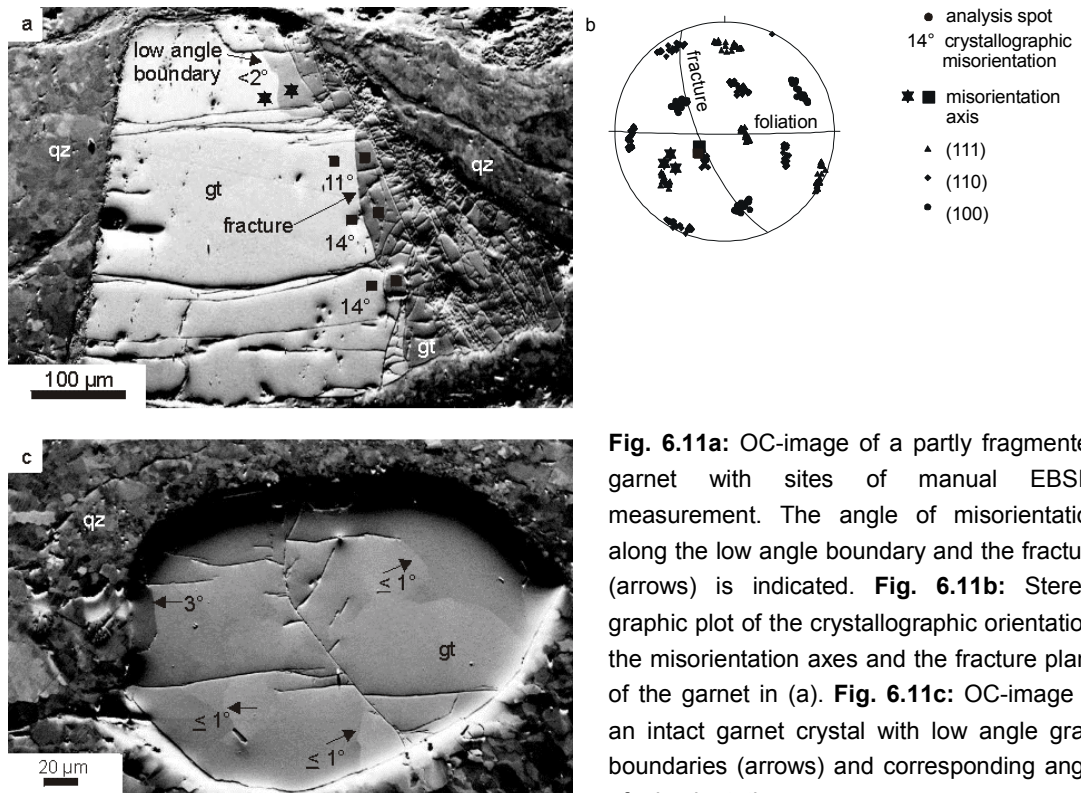


Fig. 6.11a: OC-image of a partly fragmented garnet with sites of manual EBSD-measurement. The angle of misorientation along the low angle boundary and the fracture (arrows) is indicated. **Fig. 6.11b:** Stereographic plot of the crystallographic orientation, the misorientation axes and the fracture plane of the garnet in (a). **Fig. 6.11c:** OC-image of an intact garnet crystal with low angle grain boundaries (arrows) and corresponding angle of misorientation.

6.4. Discussion

6.4.1. Implications of the microstructural record

Both intact garnet crystals and fragmented garnet that remained undistorted (Fig. 6.3) reveal a low aspect ratio. This indicates that the high aspect ratio of the distorted garnet was caused by frictional sliding along cracks. Fragmentation appears not to be restricted to crystals with a specific aspect ratio or to any evident local matrix property. Furthermore, fragmented garnet crystals that remained undistorted (Fig. 6.3) show that fragmentation was not

necessarily followed by translation of the fragments along the cracks. Thus, the displacement along the fracture plane is not directly related to the initial stage of fragmentation. This is consistent with the rather uniform displacement along the cracks, as seen in Figs. 6.2a-d, 6.3, and 6.10a, indicating that the cracks already existed when translation by frictional sliding took place.

As intact garnet crystals and individual fragments show no, or only very small internal variation in crystallographic orientation of $<3^\circ$ (Fig. 6.11a, c), the observed misorientation between the fragments, is likely to have developed after fracturing of an original single crystal with at best only a few low angle grain boundaries. The progressive increase of the magnitude of cumulative misorientation across a disintegrated grain (Fig. 6.8b) and the positive correlation between the degree of disintegration and the contrast between random-pair and neighbour-pair misorientation distributions (Figs. 6.8 and 6.9), suggest that the high misorientations are due to rotation of the fragments.

The observation of LAGBs in intact garnet and within large fragments (Fig. 6.11a,b), suggests that some of the fractures may have followed pre-existing LAGBs. Garnet substructures with a crystallographic misorientation of $<3^\circ$ were attributed to deformation by dislocation creep by Prior et al. (2000). However, formation of LAGBs as growth irregularities or during growth of porphyroblasts by agglomeration (Spiess et al., 2001) cannot be ruled out. The compositional maps, however, show no evidence for development by multiple nucleation, as concentric growth zoning is dominant and is even still discernible in some strongly fragmented and distorted garnets (Figs. 6.4b and 6.8c).

6.4.2. Conditions at initial fragmentation

Brittle failure of stiff inclusions in a ductile matrix depends on the stress transfer from the matrix to the inclusion (e.g. White et al., 1980; Boullier, 1980). One of the favoured theoretical models is the fibre loading mechanism (e.g. Ji and Zhao, 1994; Zhao and Ji, 1997), which has been applied to the development of tensile fractures in garnet in anisotropic metamorphic rocks during exhumation (Ji et al. 1997). Their model shows that the garnets become disintegrated through progressive mid-point fracturing, with cracks at right angles to the long axis of the inclusion. This model can explain the formation of sets of parallel, straight, fractures at a low angle to the maximum principal stress direction. However, progressive mid-point fracturing in a slowly creeping matrix is difficult to reconcile with the microstructural record of garnet described in this study. First, it would be expected that displacement along the cracks should reflect the relative age of the fractures, with larger displacements along the earlier generations. As seen in Figs. 6.2a-d, 6.3, and 6.10a both the fracture-parallel displacement and the fracture normal displacement in the case of opened

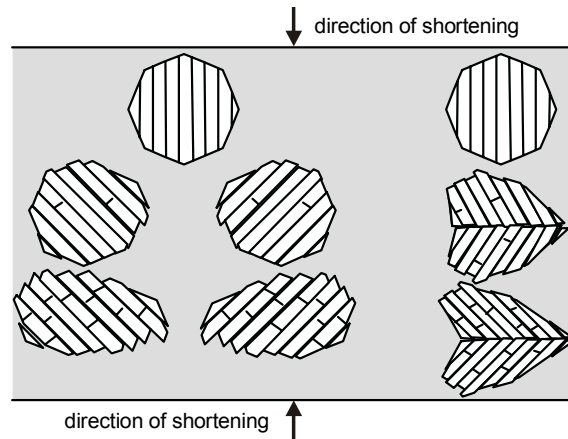


Fig. 6.12: Scheme visualising the inferred progressive cataclastic deformation of garnet crystals, planes and buckling of fragments (see text).

cracks is rather uniform, indicating a uniform age of the cracks and a common subsequent history. Second, given the small size of the fragments, the preservation of large intact garnet crystals nearby would probably require an extremely heterogeneous stress field, if progressive mid-point fracturing in a flowing matrix is assumed.

Multiple tensile, shear, and extensional shear fracturing of stiff inclusions hosted in a ductile matrix was addressed in experiments and modelled by Mandal et al. (2001). These authors show that the aspect ratio and the orientation of the inclusions control the internal principal tensile and compressive stresses and, thus, control the mode of failure. They also found that the stress inside an inclusion is homogenous and that the magnitude of the maximum principal compressive stress is inversely proportional to the ellipticity of the inclusion, so that shear fracturing is favoured for a low aspect ratio. At a given confining pressure and bulk strain rate inclusions with an axial ratio below a critical value do not fracture at all and remain intact.

Following the results of Mandal et al. (2001), the original low aspect ratio of the garnets in this study would suggest failure by shear fractures. However, the F1 fracture sets in garnet of sample CT183 show a uniform inclination to the foliation, even in undistorted garnet (Fig. 6.3). Furthermore, conjugate crack systems are not observed, as would be expected for shear fracture. In the highly distorted garnet of the mylonite sample St12 the apparent conjugate systems observed could have developed during rotation by progressive deformation (Fig. 6.12), with coalescence of F2 cracks. If fragmentation was by formation of tensile cracks, with the fracture planes oriented parallel to the maximum principal stress σ_1 direction, the orientation of σ_1 at the instant of crack formation could have been oblique to the foliation, or the cracks may have been reoriented by uniform rotation of the fragments in simple shear.

Shear bands and sets of deformation lamellae in the quartz matrix, that parallel the fractures in garnet (Fig. 6.1c) may represent healed cracks. A correlation of these features with either the stage of garnet fragmentation or that of subsequent displacement is not possible, as the microstructural record is obliterated due to plastic flow and recrystallisation of the quartz matrix. However, a pervasive cataclastic disintegration of the rock cannot be ruled out.

Despite of the uncertainty regarding the mode of formation of the F1 fractures, a quasi-instantaneous fragmentation is proposed, with all F1 cracks formed nearly simultaneously, followed by distortion of the aggregate in the creeping quartz matrix. A well defined yield stress for the fragmentation of the garnet is probably the reason why some crystals remained intact at sites where the critical value was not attained due to minor heterogeneities in the stress field.

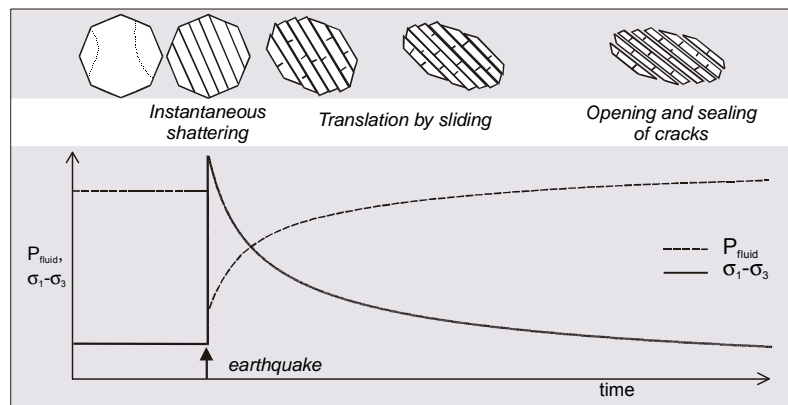
6.4.3. Tectonic environment and inferred boundary conditions

Garnet is a high strength mineral phase, well known through its occasional use as an abrasive. For non-silicon garnet, brittle strength has been investigated in material science using microindentation and fracturing techniques. These experiments suggest a very high theoretical cohesive strength (extensional) of 49 GPa, which is comparable to that of corundum (e.g. Pardavi-Horváth, 1984; Reimanis et al., 1994). Thus, brittle deformation of natural garnet is expected to be restricted to extraordinary conditions with very high stresses and stress rates. For instance, Austrheim et al. (1994, 1996) attributed garnet fragmentation combined with the occurrence of pseudotachylites to seismic activity in the lower crust. Degenhardt et al. (1994) also describe localised cataclastic comminution of garnet in granite gneisses of the Roter Kamm impact crater, Namibia.

It has been proposed that the microstructural record of the rocks of the Sesia Zone described in this chapter was acquired when they had attained a position in the uppermost plastosphere, just beneath the brittle-plastic transition (Küster and Stöckhert, 1999), during a period of major seismic activity in the overlying schizosphere. In this case, instantaneous stress redistribution during major earthquakes causes synseismic loading and short term postseismic creep in the uppermost plastosphere, with a strain-rate dependent transient downward displacement of the brittle-plastic transition. Mechanical twinning of clinopyroxene indicates that the rocks were exposed to very high stresses (possibly > 0.5 GPa; see Chapter 6), implying near-laboratory strain rates and markedly sublithostatic pore fluid pressure (Küster and Stöckhert, 1999).

Quasi-instantaneous shattering of the garnet crystals – fragmentation by F1 cracks - is proposed to have taken place (Fig. 6.13) at the stage of synseismic loading. Subsequently, during decay of the synseismically created stresses, the fragments were displaced by frictional sliding along the fractures (Fig. 6.13). At this stage, deformation of garnet was controlled by rapidly decelerating dislocation creep in the surrounding quartz matrix.

Fig. 6.13: Proposed model relating cataclastic deformation of garnet to synseismic loading and postseismic creep, see text for discussion.



The very high stresses in the early stage of fragmentation are not compatible with a notable pore fluid pressure. Therefore the rocks must have been either essentially dry, which appears unlikely in view of the fluid inclusions along healed cracks described by Küster and Stöckhert (1999), or the pore fluid pressure has dropped due to dilatation and a transient high permeability related to fractures synseismically propagating down to depth where deformation usually processes by slow and pressure-insensitive fully plastic creep. The opening of the cracks in garnet at a very late stage of deformation, with open space being filled by quartz and feldspar precipitated from the pore fluid (Fig. 6.13), suggests that the pore fluid pressure regained a near-lithostatic value in the final stage of postseismic creep. Little strain has been accumulated at this late stage, as shown by the small crack-normal displacement, while fracture-parallel sliding had dominated during the major part of postseismic creep.

6.5. Conclusions

The record of garnet is consistent with the processes of synseismic loading related to major seismic activity in the overlying schizosphere, and stress relaxation combined with reconstitution of a near-lithostatic pore fluid pressure during postseismic creep in the uppermost plastosphere, reconciling with seismic activity.

The inferred microstructural evolution of garnet, schematically depicted in Fig. 6.13, can thus be subdivided into three stages.

- 1) Quasi-instantaneous shattering of the garnet crystals during synseismic loading to high peak-stresses, with pore fluid pressure dropping to markedly sub-lithostatic values, preventing an opening and sealing of the microcracks.
- 2) Progressive displacement of the garnet fragments by frictional sliding along the fractures, controlled by rapidly decelerating dislocation creep in the surrounding quartz matrix, reflecting the main stage of postseismic creep and stress relaxation.
- 3) Late stage deformation driven by residual stresses, with garnet fragments becoming separated by a crack-normal component of displacement. At this stage pore fluid pressure must have attained near-lithostatic values, permitting opening of the cracks and sealing by quartz and feldspar precipitated from the pore fluid. The strain accumulated at this final stage of postseismic creep is only small.

Clearly, fundamental questions concerning the load transfer between a weak matrix and a stiff inclusion, and the mode of failure at the stage of fragmentation, are unresolved and deserve further consideration. Nevertheless, the microstructural record of exhumed, mid-crustal rocks can provide valuable insight into processes and boundary conditions relevant to present-day earthquakes.

7. Plasticity and creep of quartz*

7.1. Introduction

Plastic flow of quartz, which is one of the main constituents of the continental crust, is presumed to control the strength of the uppermost plastosphere with plastic flow of feldspar taking over at greater depth and higher temperatures (e.g. Tullis and Yund, 1987; Hirth and Tullis, 1989; Tullis, 1990). Both, the deformation mechanisms and the resulting microstructures depend on the temperature and stress conditions that quartz is exposed to. The quartz microstructural record in exhumed metamorphic rocks can provide important information on the tectonic conditions prevailing at the BPT-zone during exhumation (see Chapter 1.2).

The highly heterogeneous quartz microstructures in small scale shear zones in micaschists and quartz veins reveal a large variety of conspicuous and rather uncommon features. Sub-basal deformation lamellae and arrays of elongate subgrains on the TEM-scale indicate an early stage of glide-controlled deformation at high stresses. Distributed brittle failure is indicated by healed microcracks. Very fine-grained recrystallised aggregates with a pronounced crystallographic preferred orientation reflect intense plastic flow by dislocation creep. Locally, a foam microstructure indicates a final stage of static grain growth at low differential stress. The results of an analysis of these quartz microstructures by optical microscopy, scanning (SEM) and transmission electron microscopy (TEM) are presented in this chapter, and discussed in terms of loading and relaxation history.

7.2. Sampling

The late stage plastic deformation is concentrated into centimetre to decimetre wide shear zones (see Chapter 4), which are widespread in the eclogitic micaschist of the lower Aosta valley, the Val Chuisella, and at Mt. Mucrone (Fig. 7.1).

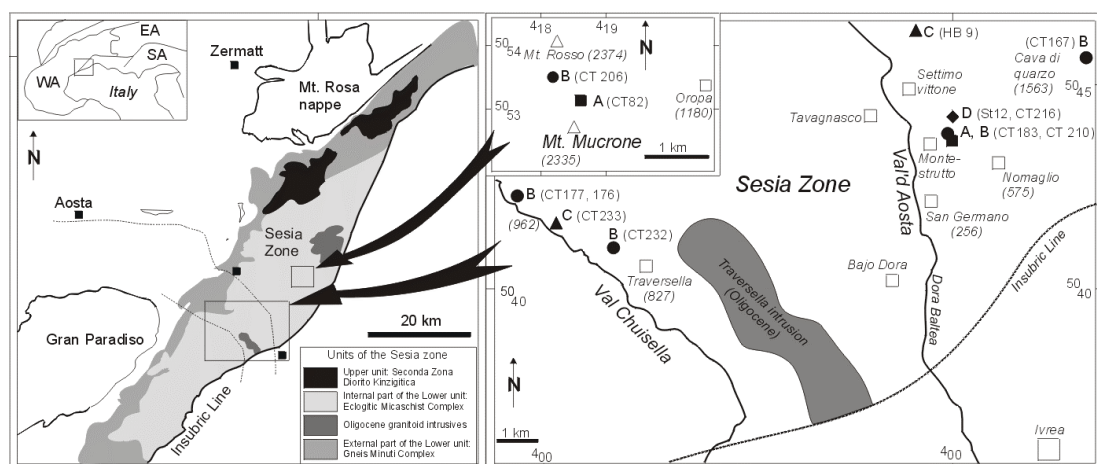


Fig. 7.1: Sketch map of the tectonic units of the Sesia Zone and study areas. The localities of the different types of quartz microstructures are labelled as A: filled square, B: filled circle, C: filled triangle and D: filled rhomb.

*The results presented in this chapter are prepared to be published in:

Trepmann C.A., Stöckhert B. (submitted to *J. Struct. Geol.*). Quartz microstructures developed during non-steady state plastic flow at rapidly decaying stress and strain rate.

Outside these shear zones, the record of quartz is less specific due to limited strain, with intense plastic deformation and recrystallisation restricted to sites of stress concentration between rigid grains of other minerals. Sampling was focussed on small scale shear zones in quartz-rich domains or quartz veins. The location of the samples in the lower Aosta valley, Val Chuisella and at Mt. Mucrone is shown in Fig. 7.1, with the sample numbers and type of quartz microstructure, as referred to in this study, indicated.

7.3. The microstructural record of quartz in the shear zones

According to the proportion of recrystallised grains the quartz microstructures within the shear zones can be loosely grouped into four types, here referred to as type A to D. Type A microstructure is characterised by strong plastic deformation, but very limited recrystallisation, while type D microstructure is characterised by complete recrystallisation. Microstructures of the different types are found to occur adjacent to each other, showing no systematic distribution pattern in the investigated area (Fig. 7.1). In this section, first the overall characteristics of the type A to D microstructures are described.

7.3.1. Type A microstructure

Type A microstructures have been found at localities in the lower Aosta valley (sample CT183; coordinates 409.416E, 5043.518N, see Fig. 7.1) and at Mt. Mucrone (sample CT82; coordinates 418.486E, 5053.212N, see Fig. 7.1). For detailed analysis sample CT 183 was chosen.

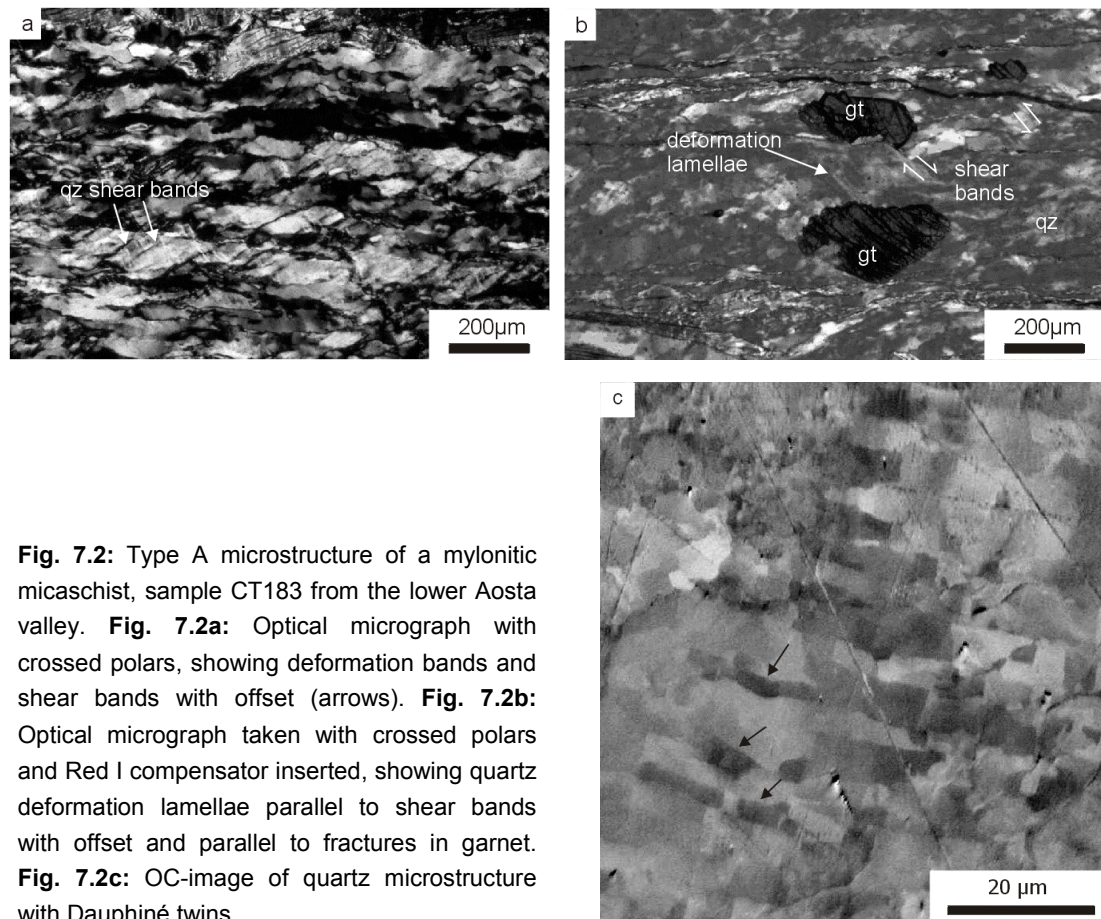


Fig. 7.2: Type A microstructure of a mylonitic micaschist, sample CT183 from the lower Aosta valley. **Fig. 7.2a:** Optical micrograph with crossed polars, showing deformation bands and shear bands with offset (arrows). **Fig. 7.2b:** Optical micrograph taken with crossed polars and Red I compensator inserted, showing quartz deformation lamellae parallel to shear bands with offset and parallel to fractures in garnet. **Fig. 7.2c:** OC-image of quartz microstructure with Dauphiné twins.

The type A quartz microstructure comprises barely recrystallised aggregates with a variable grain size of 10 to 100 μm and irregular shape (Fig. 7.2a-c). Sub-basal deformation lamellae (e.g. Avé Lallement and Carter, 1971), with the orientation identified by U-stage, are developed in some larger quartz crystals (Fig. 7.2b). Discrete shear bands with minor offset are common (Fig. 7.2a) and can be oriented parallel to deformation lamellae in quartz and fractures in garnet (Fig. 7.2b). Alternating dark and bright areas in OC-images (Fig. 7.2c) reveal the occurrence of Dauphiné twins, as confirmed by EBSD-measurements.

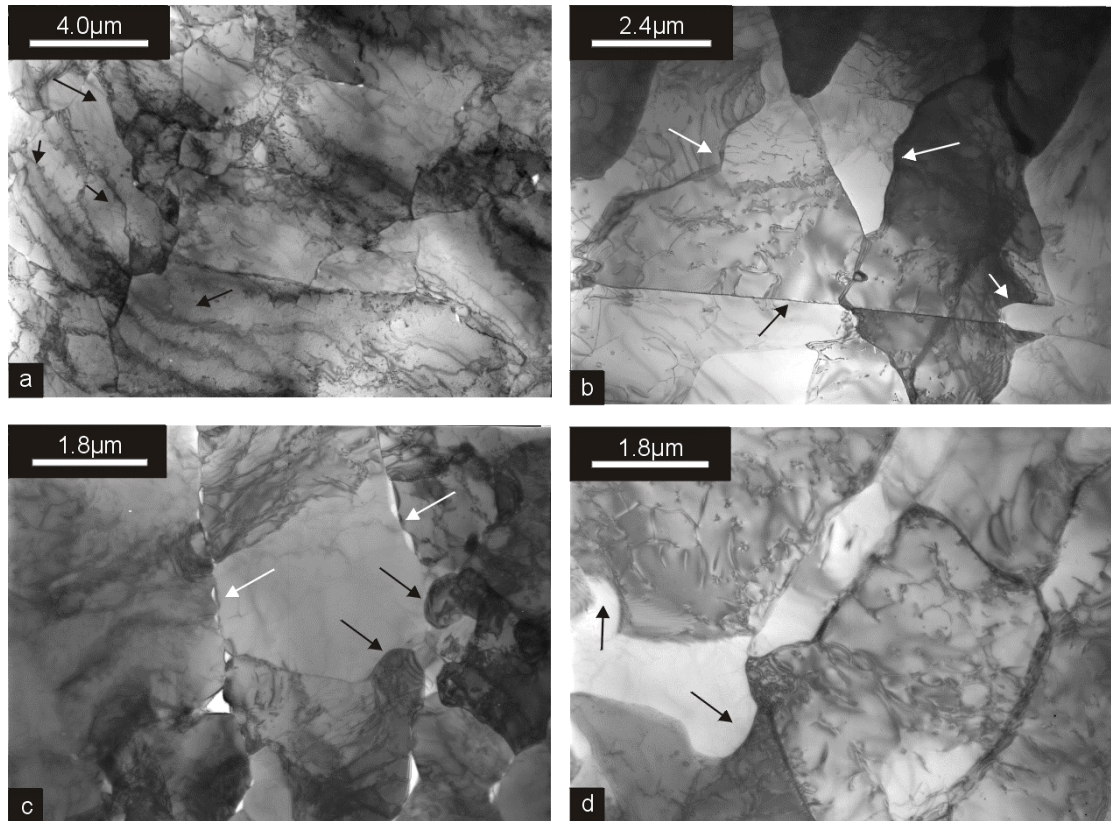


Fig. 7.3: TEM bright-field micrographs of the type A quartz microstructure from sample CT183. **Fig. 7.3a:** Overview of inhomogeneous subgrain-structure and dislocation arrangement with curved irregular low angle grain boundaries bounding elongate subgrains (arrows). **Fig. 7.3b:** Straight low angle grain boundaries decorated with fluid inclusions (black arrow) and strongly curved grain boundaries (white arrows). **Fig. 7.3c:** Parallel, straight grain boundaries decorated with fluid inclusions (white arrows) and bulging grain boundaries (black arrows). **Fig. 7.3d:** Bulging grain boundaries (arrows).

The highly heterogeneous type A quartz microstructure reveals a similarly heterogeneous submicroscopic structure in the TEM (Fig. 7.3), with curved dislocation walls or poorly ordered low angle grain boundaries (Fig. 7.3a) defining elongate subgrains of irregular shape. Similar submicroscopic features are commonly associated with optical-scale deformation lamellae in naturally deformed quartz and in experimentally deformed metal alloys (Drury, 1993). Another conspicuous submicroscopic feature is the occurrence of straight low angle grain boundaries, frequently decorated with fluid inclusions (Fig. 7.3b, c), which probably represent healed microcracks as they cut grain boundaries (Fig. 7.3b). Strongly curved, bulging high angle grain boundaries with a wavelength of about 0.5 μm (Fig. 7.3b to d) of larger quartz grains are indicative of strain-induced grain boundary migration. The free dislocation density varies within one order of magnitude between about $5 \cdot 10^{13} \text{m}^{-2}$ and $2 \cdot 10^{14} \text{m}^{-2}$. In general, large grains reveal a higher free dislocation density compared to small recrystallised

grains (Fig. 7.3d). Fluid inclusions of about 0.1 to 0.2 μm in diameter are mostly concentrated along grain boundaries, both low and high angle (Fig. 7.3a).

7.3.2. Type B microstructure

The type B microstructure appears to be the most widespread type, being found in five localities in the lower Aosta valley (sample CT210; coordinates 409. 416°, 5043. 518N; sample CT167; coordinates 413.114°, 5045.720N), in the Val Chuisella (samples CT176 and CT177; coordinates 398.877°, 5042.129N; sample CT232; coordinates 401. 490E, 5040. 885N) and at Mt. Mucrone (sample CT206; coordinates 418.354E, 5053.285N).

Characteristic for type B microstructures are quartz ribbons surrounded by recrystallised quartz grains (Fig. 7.4). The quartz ribbons measure up to 20 mm in length and 4 mm in width. The aspect ratio is variable, frequently exceeding a value of 10.

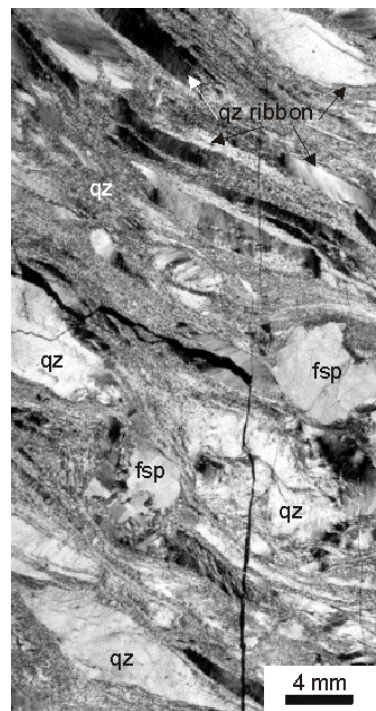


Fig. 7.4: Type B quartz microstructure showing large quartz ribbons surrounded by recrystallised quartz grains and few feldspar porphyroclasts. Thin section scanned with crossed polars (sample CT210).

The most conspicuous feature within these ribbons are deformation lamellae (Fig. 7.5a). They are visible in both plane- polarised light and with crossed polars as parallel to sub-parallel, closely-spaced planar or slightly undulating features, with an apparently slightly different refractive index or crystallographic orientation compared to the host grain. The spacing of the deformation lamellae is about $4.5 \pm 2 \mu\text{m}$. A sub-basal orientation, with an angle of about $10\text{-}30^\circ$ to the basal plane was determined by U-stage (Fig. 7.6). Sub-basal deformation lamellae conspicuous in the optical microscope are barely visible in OC-images (compare Fig. 7.7a, b). An EBSD-orientation map (Fig. 7.7c) of a quartz ribbon with deformation lamellae and the associated misorientation profile (Fig. 7.7d) reveal that the misorientation between the lamellae and the host grain is small, generally not exceeding 2° ; this is close to the uncertainty of about 1° for EBSD-measurements (e.g. Lloyd, 1995). Deformation bands roughly parallel to the c-axis are discernible at a high angle to the sub-basal lamellae (Fig. 7.5a, b). Locally quartz ribbons resemble kinkbands (Fig. 7.5b).

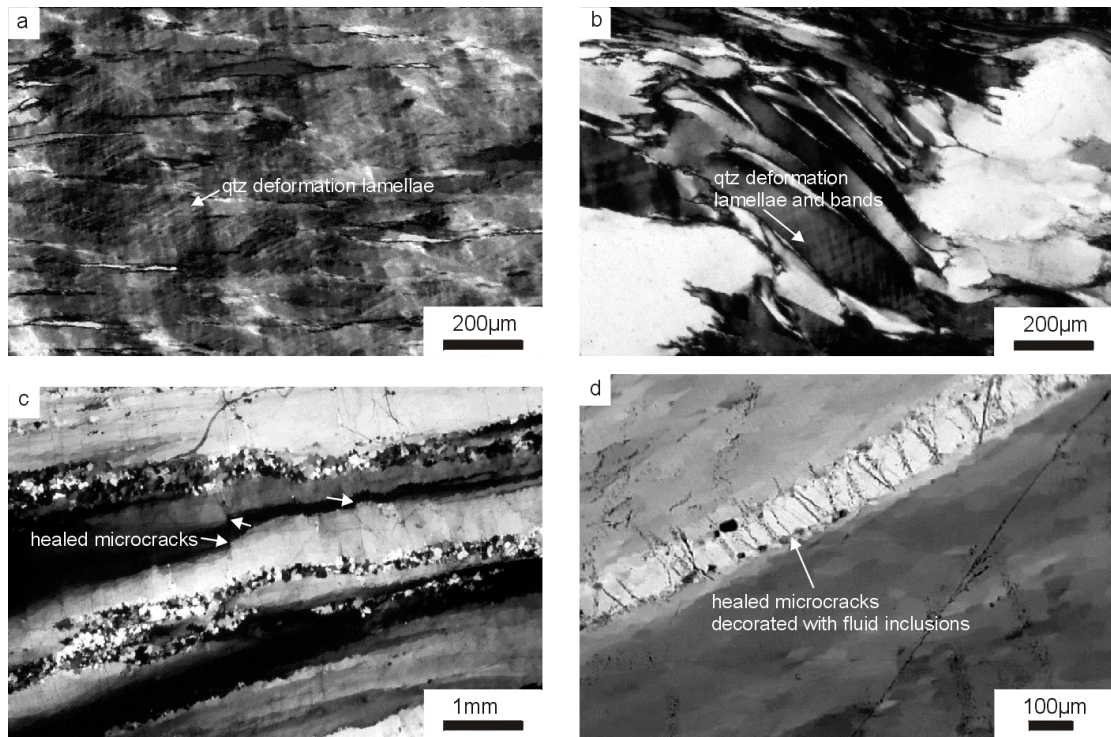


Fig. 7.5: Optical micrographs showing the type B quartz microstructure, all taken with crossed polars. **Fig. 7.5a:** Microstructure showing extensive development of deformation lamellae in quartz crystals, sample CT177 from Val Chuisella (micrograph taken with Red I compensator inserted). **Fig. 7.5b:** Heterogeneous quartz microstructure with kink band-like, parallel quartz ribbons showing deformation lamellae and bands, sample CT176 from Val Chuisella. **Fig. 7.5c:** Parallel, healed microcracks with offset, sample CT232 from Val Chuisella. **Fig. 7.5d:** Parallel fluid inclusion trails restricted to a subgrain within a large quartz ribbon, sample CT210.

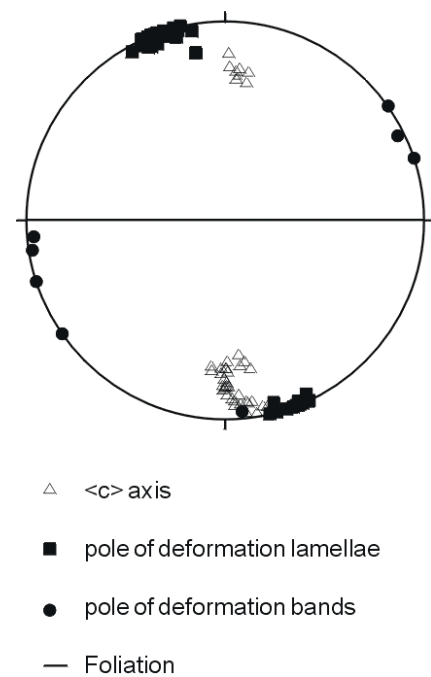


Fig. 7.6: Stereographic projection of the orientation of deformation lamellae and deformation bands in sample CT177, measured with U-stage. The orientation of c -axis measured by the EBSD-technique.

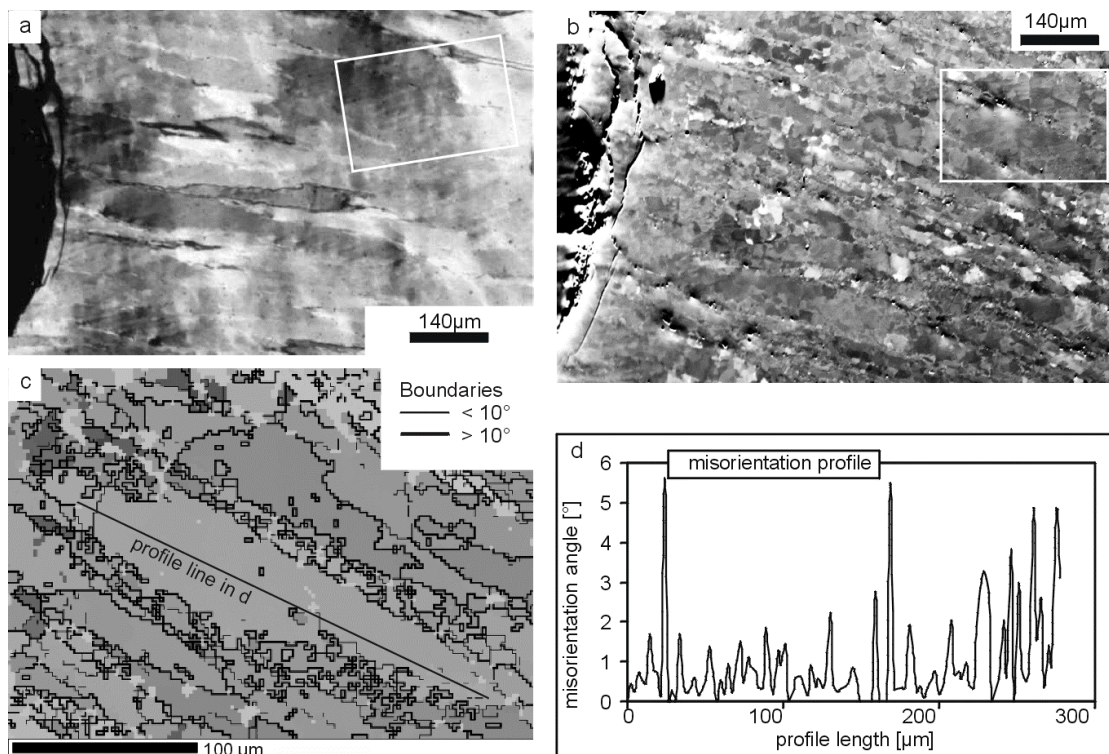


Fig. 7.7a: Optical micrograph taken with crossed polars, showing quartz grains with sub-basal deformation lamellae, sample CT177; the white rectangle marks the position of the EBSD-map in (c). **Fig. 7.7b:** OC-image of the region shown in (a). **Fig. 7.7c:** EBSD-map of a region shown in (a) and (b) by a white rectangle with profile line. Thick black lines mark high angle ($>10^\circ$) and thin black lines mark low angle ($2\text{--}10^\circ$) boundaries. **Fig. 7.7d:** Misorientation profile along line shown in (c).

In places, mutually parallel fluid inclusion trails transect the quartz ribbons at a high angle to their long axis, commonly revealing a small shear offset (Fig. 7.5c). These trails are interpreted to represent healed microcracks. Figure 7.5d shows that these cracks can be restricted to a single subgrain within a quartz ribbon, where they are approximately parallel to the basal plane. This restriction indicates that brittle failure was controlled by the crystallographic orientation relative to the imposed stress field (e.g. Vollbrecht et al., 1999).

TEM investigation of sample CT177, characterised by the common occurrence of sub-basal deformation lamellae on the optical scale (Figs. 7.5a and 7.7a,b) reveals very small recrystallised grains, with a diameter down to $<2\mu\text{m}$. The high angle grain boundaries are simply curved (Fig. 7.8a, c). These recrystallised grains appear to be nearly free of dislocations. Otherwise, most dislocations are geometrically necessary and arranged into well ordered low angle grain boundaries with tilt and twist geometry (Fig. 7.8c). The free dislocation density within larger grains is about 2 to $9 \cdot 10^{12}\text{m}^{-2}$ (Fig. 7.8d). Only few subgrains (Fig. 7.8b) are elongate, as commonly observed in type A microstructures. Also, straight low angle grain boundaries decorated with fluid inclusions, probably representing healed cracks, are only rarely observed (Fig. 7.8d). Some intragranular fluid inclusions occur in larger grains, where they are commonly associated with dislocations (Fig. 7.8d). Lens-shaped fluid inclusions decorate low and high angle grain boundaries (Fig. 7.8d).

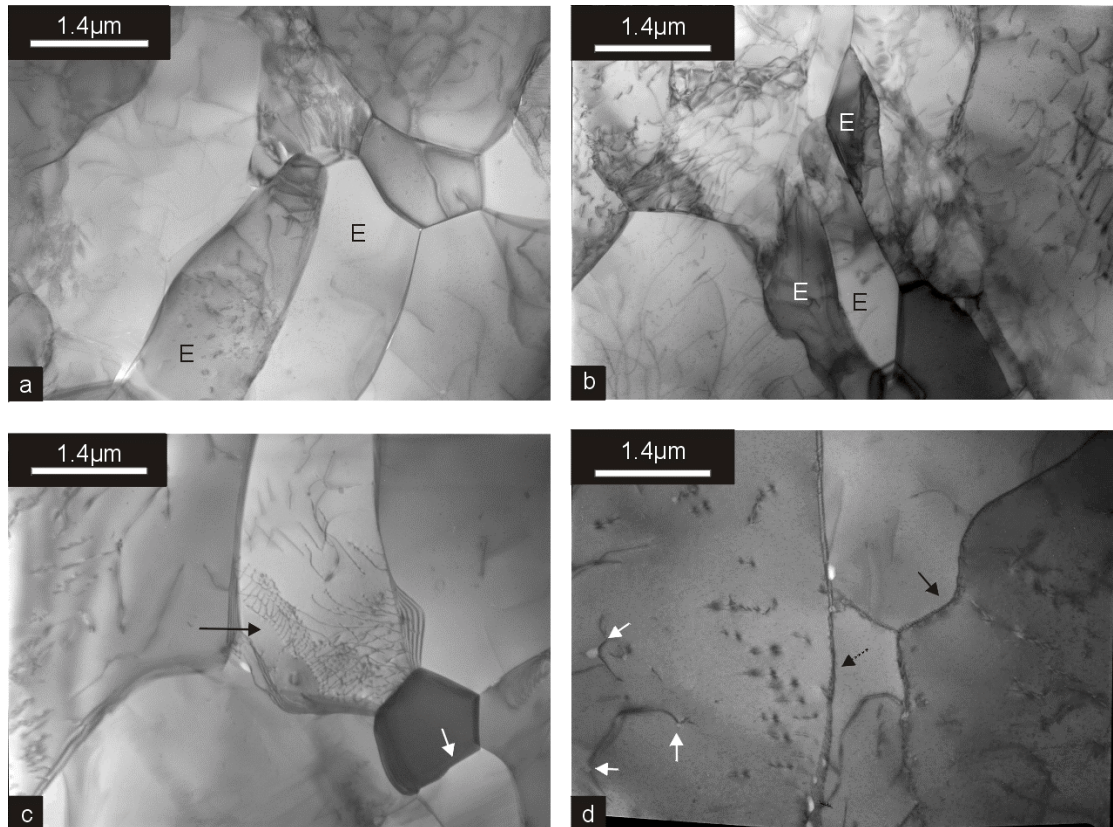


Fig. 7.8: TEM bright-field micrographs of the type B quartz microstructure, sample CT177. **Fig. 7.8a:** Elongate grains (E) with simply curved boundaries and low dislocation density. **Fig. 7.8b:** Elongate subgrains (E). **Fig. 7.8c:** Small dislocation-free grain with slightly curved boundaries (white arrow) and larger grain with a low angle grain boundary with twist geometry (black arrow). **Fig. 7.8d:** Grain with a strongly-curved grain boundary (black arrow) and a straight low angle grain boundary decorated with fluid inclusions (dashed line arrow). Bent dislocations with dipoles pinned at fluid inclusions are marked by a white arrow.

The occurrence of well ordered low angle grain boundaries and small new grains nearly devoid of dislocations (Fig. 7.8a, c) are indicative of recovery and recrystallisation (e.g. White, 1977). Although deformation lamellae are conspicuous on the optical scale, submicroscopic features that could be unequivocally correlated with the lamellae are not identified by TEM.

7.3.3. Type C microstructure

The type C microstructure is observed in samples from the Val Chuisella (sample CT233; coordinates 398.616E, 5042.385N) and from the lower Aosta valley (sample HB9; coordinates 409.100E, 5045.789N). Sample CT233 has been chosen for detailed investigation.

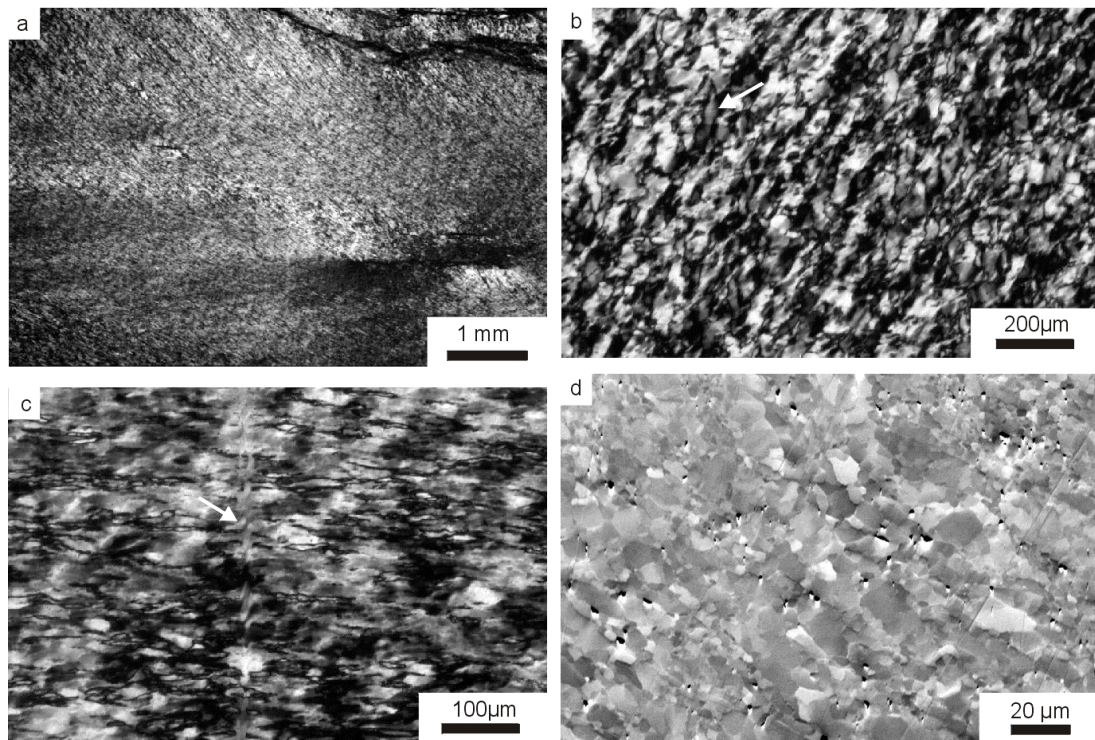
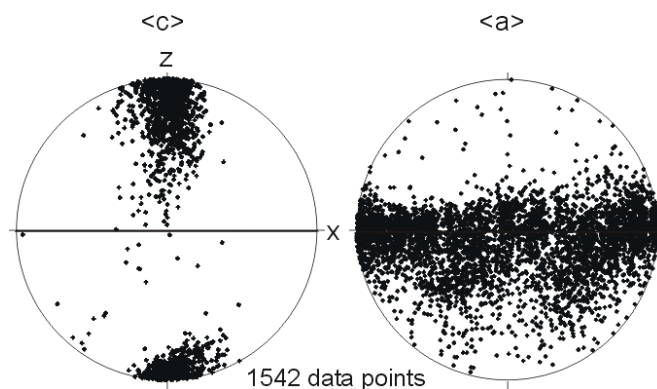


Fig. 7.9: Optical micrographs taken with crossed polars showing the type C microstructure, sample CT233 from Val Chuisella. **Fig. 7.9a:** Microstructure with marked locally varying SPO around a calcite porphyroblast. **Fig. 7.9b:** Quartz recrystallised grains. A few deformation lamellae (arrow) are hardly discernible. **Fig. 7.9c:** Small-scale quartz vein (arrow) perpendicular to foliation in recrystallised quartz aggregate. **Fig. 7.9d:** OC-image of recrystallised quartz aggregate showing an irregular (sub-)grain structure.

The type C quartz microstructure is highly heterogeneous, with aggregates of recrystallised grains with variable grain size (Fig. 7.9). The smallest observed grain size varies between 5 μm and 20 μm (Fig. 7.9d). Within larger grains, with a size between 20 and 50 μm , only very few deformation lamellae are discernible (Fig. 7.9b). The quartz grains are irregular in shape (Fig. 7.9a-d), with a marked shape preferred orientation (SPO), reflecting a heterogeneous strain field (Fig. 7.9a). Also, a distinct crystallographically preferred orientation (CPO) is developed (Fig. 7.10). The CPO reveals a point maximum of the c-axes perpendicular to the foliation plane and a maximum of the $\langle a \rangle$ axes in the foliation plane, indicating basal $\langle a \rangle$ glide.

Fig. 7.10: Pole figures showing the orientation of quartz $\langle c \rangle$ and $\langle a \rangle$ axis of recrystallised grains, sample CT233, investigated by automatic EBSD-measurements. The orientation of $\langle c \rangle$ axis reveal a point maximum around the highest compression direction and the $\langle a \rangle$ axis a maximum within the foliation plane.



Small-scale quartz veins perpendicular to the foliation (Fig. 7.9c) are obvious in the recrystallised quartz aggregates. The quartz crystals in these veins show subgrains and an identical or similar crystallographic orientation to adjacent grains in the matrix.

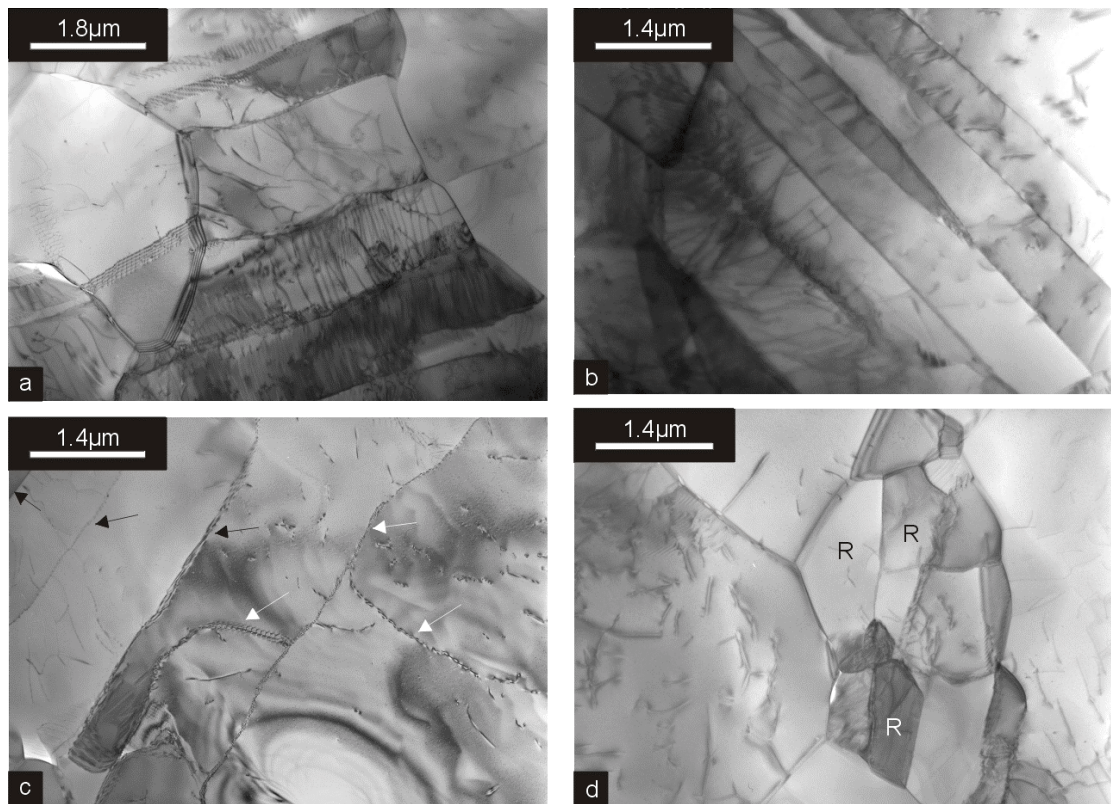


Fig. 7.11: TEM bright-field micrographs of recrystallised quartz aggregates of the type C microstructure, sample CT233. **Fig. 7.11a:** Straight parallel subgrains. **Fig. 7.11b:** Straight parallel low angle grain boundaries bounding elongate subgrains with a width of less than 1 μm . **Fig. 7.11c:** Straight parallel (black arrows) and simply curved low angle grain boundaries (white arrows). **Fig. 7.11d:** Arrangement of small recrystallised grains (R).

Most conspicuous at the submicroscopic scale in the TEM are elongate subgrains (Fig. 7.11a-c) with a width of approximately 0.5 to 1.6 μm and a length of about 4 to 7 μm . They show no specific orientation in a single sample (compare Fig. 7.11a-c). Recovery and recrystallisation are indicated by the arrangement of geometrically necessary dislocations in well-ordered low angle grain boundaries (Fig. 7.11c) and by small (down to $<2\mu\text{m}$) new-formed grains that are almost devoid of dislocations (Fig. 7.11d). Elsewhere, the free dislocation density is about 2 to $8 \cdot 10^{12} \text{m}^{-2}$.

7.3.4. Type D microstructure

Type D microstructures have been identified exclusively in the lower Aosta valley (sample St12; coordinates 409 E, 5043 N; sample CT 216; coordinates 409.555E, 5043.528N). Sample St 12 was chosen for detailed investigation.

The type D quartz microstructure is a homogeneous fine-grained aggregate with a pronounced CPO. The grains are equant, with an average grain size of 7 μm . The grain boundaries are straight to simply curved (Figs. 7.12a to c).

The CPO (Fig. 7.13) shows mostly a distinct point maximum of the $\langle c \rangle$ axes in the shortening (Z-) direction, while the maximum of the orientation of the $\langle a \rangle$ axes lies in the foliation (XY-) plane. This CPO implies basal slip in the $\langle a \rangle$ direction. Locally, the texture reveals a girdle of the $\langle c \rangle$ axes oriented about normal to the stretching (X-) lineation, suggesting that at these sites $\langle a \rangle$ slip on the rhombohedral and prism planes was activated as well. Similar to the type C microstructures, μm -wide quartz veins oriented perpendicular to the foliation are observed in places (Fig. 7.12a).

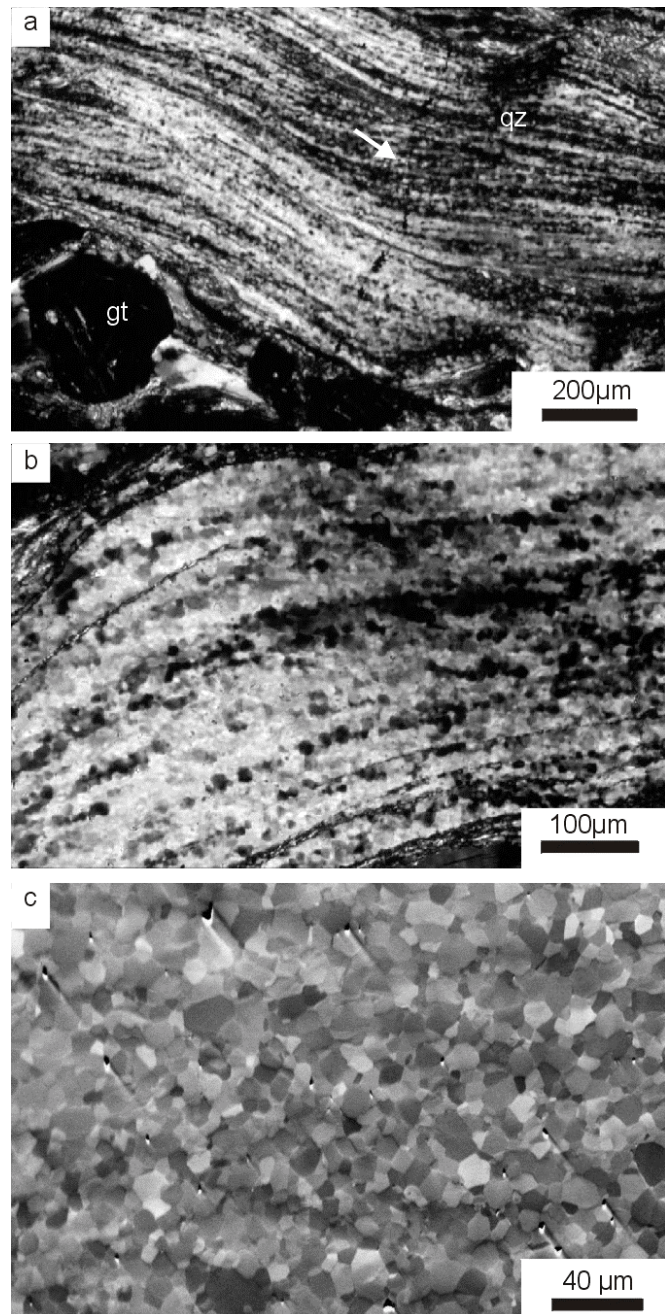


Fig. 7.12: Type D microstructure (sample St12). **Fig. 7.12a-b:** Optical micrographs (crossed polars) showing fine-grained recrystallised quartz aggregate with strong CPO; note quartz vein perpendicular to foliation (arrow) in (a). **Fig. 7.12c:** OC-image showing quartz foam structure characterised by isometric grains revealing simply curved boundaries and typical near- 120° angles between boundaries at the grain edges.

On the TEM scale, the recrystallised grain size is found to be smaller than that discernible on the optical scale, with a typical grain diameter of about 2 to 5 μm . This discrepancy may be caused by the pronounced CPO, that masks certain grain boundaries due to vanishing contrast for respective positions of the rotating stage when viewed in the polarising microscope. Also, a typical foam structure with straight or simply curved grain boundaries meeting at near- 120° angles at the grain edges (Fig. 7.14a) is conspicuous in the TEM. In other places, low angle grain boundaries (Fig. 7.14b to d), which in part delineate strongly elongate subgrains (Fig. 7.14c), and dislocation tangles are observed. The free dislocation density is in the range of about 2 to $8 \cdot 10^{12} \text{m}^{-2}$. Fluid inclusions (Fig. 7.14c, d) occur along both low angle and high angle grain boundaries. Intragranular fluid inclusions were not observed.

Fig. 7.13: Quartz pole figures of $\langle c \rangle$ and $\langle a \rangle$ orientations, investigated by automatically EBSD-measurements. **Fig. 7.13a:** The $\langle c \rangle$ axis orientation reveals a point maximum around the highest compression direction. The $\langle a \rangle$ axis orientations form a maximum within the foliation plane. **Fig. 7.13b:** The orientation of the $\langle c \rangle$ axis shows a girdle maximum in the yz plane. The $\langle a \rangle$ axis reveal an ill-defined point maximum around the smallest compression direction x.

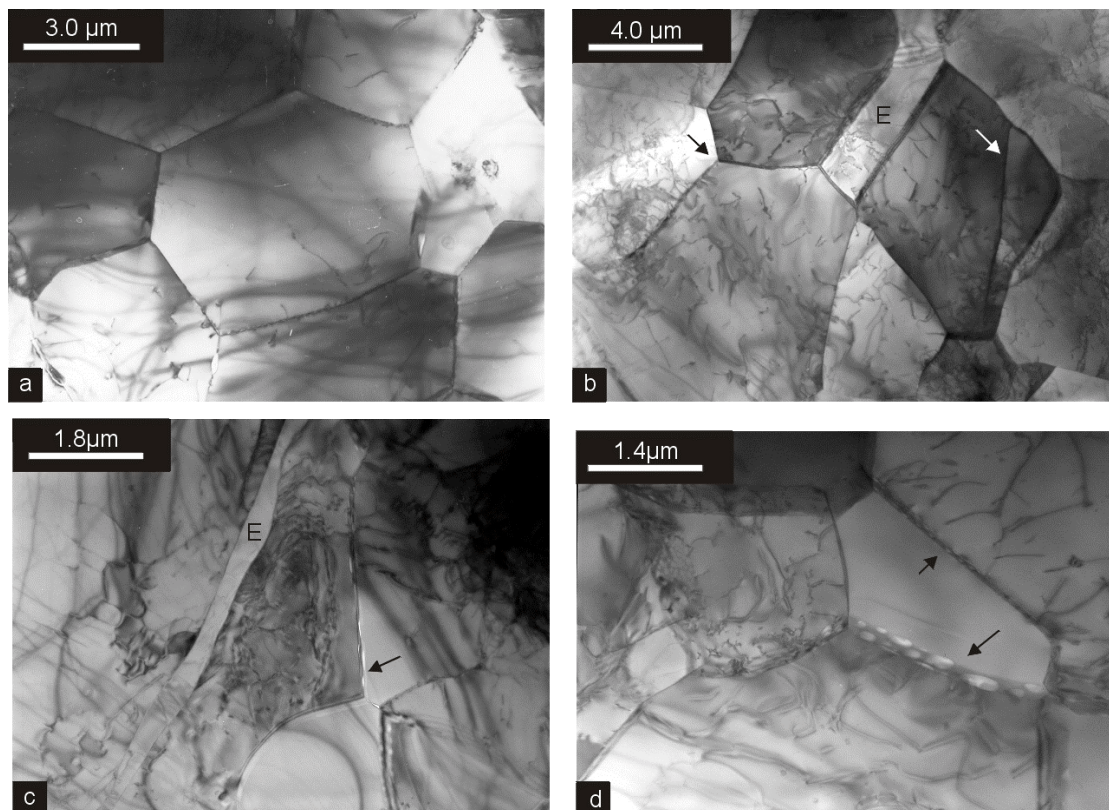
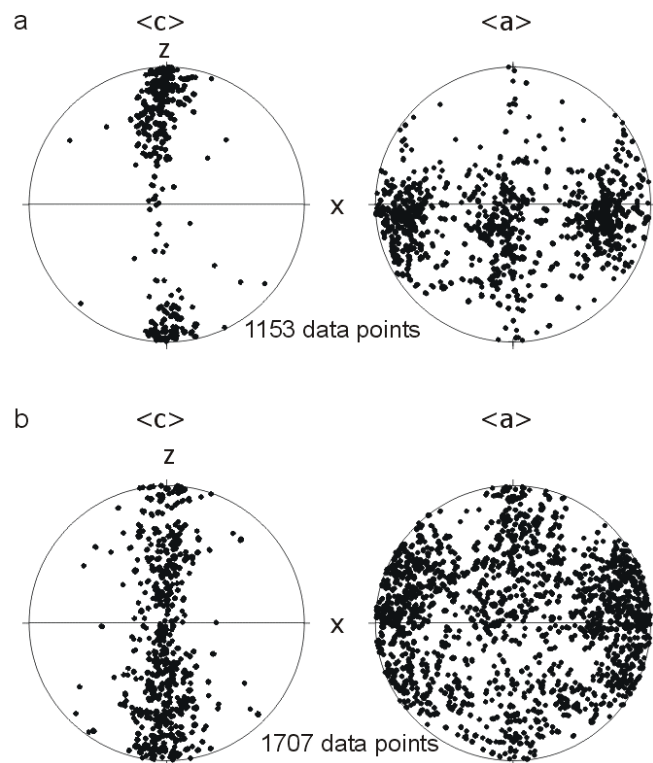


Fig. 7.14: TEM bright-field micrographs of recrystallised quartz aggregates of sample St12. **Fig. 7.14a:** Typical foam structure characterised by recrystallised grains with planar boundaries and 120° angles between the boundaries at grain edges. **Fig. 7.14b:** Recrystallised grains with typical 120° angles between the boundaries at grain edges (black arrow), a low angle grain boundary (white arrow) and an elongate grain with straight, parallel boundaries (E). **Fig. 7.14c:** Grain boundary decorated with fluid inclusions (arrow) and a very narrow, elongate subgrain (E). **Fig. 7.14d:** Grain boundaries decorated with fluid inclusions (arrows).

7.3.5. Type and concentration of water and water-related defects

FTIR-microspectrometric analyses were performed on selected quartz samples with different microstructures to obtain information on the type and concentration of molecular water and water-related defects. At room temperature, the FTIR spectra reveal a broad absorption band extending from around 3700 cm^{-1} , through a maximum at about 3400 cm^{-1} , to around 3100 cm^{-1} . This broad band absorption represents aggregated molecular water (Paterson, 1989). In low-temperature spectra, recorded at about 100 K, a marked peak near 3200 cm^{-1} corresponds to the absorption band of ice (Paterson, 1989), indicating molecular water in freezable fluid inclusions. Water-related point defects that commonly appear as sharp peaks in the low-temperature FTIR-spectra are not discernible. The marked ice-band in the low-temperature FTIR-spectra indicates that molecular water in submicroscopic fluid inclusions is the dominant OH-species. The TEM images suggest that the fluid inclusions are concentrated along grain boundaries, with only a few occurring as intragranular fluid inclusions (Figs. 7.3c, 7.8d and 7.14d). The bulk water content of the quartz aggregates was calculated from the absorption spectra, measured at temperatures of about 100 K, using the method of Paterson (1982). The FTIR-spectra of completely recrystallised type D quartz aggregates indicate the highest water content with 2500 to 4000 ppm H/Si. The quartz grains from the type A and type B microstructures showing deformation lamellae contain less than 2500 ppm H/Si. Barely deformed quartz grains of type B microstructures reveal the lowest water content of less than 1000 ppm H/Si.

7.4. Discussion

The fact that microstructures preserved in natural deformed rocks compare well to those produced in laboratory experiments is generally taken to indicate identical deformation regimes (e.g. Hirth and Tullis, 1992; 1994; Hirth et al., 2001) and thus to allow extrapolation of experimental flow laws to natural conditions. However, Stöckhert et al. (1999) emphasised that this comparison must be performed very carefully, taking into account the cumulative strain and deformation history of natural rocks and the low preservation potential of certain microstructures during the prolonged natural thermal history in comparison to quenched laboratory samples. In the study by Stöckhert et al. (1999), successive overprinting of microstructures due to ongoing deformation during progressive cooling was related to temperature history. In contrast, in the present study, the effect of short term stress and strain rate variations at constant temperature is emphasised. In the following, first the various microstructural indicators for the different deformation regimes passed by the samples, then some consequences for the application of paleopiezometers, and finally the overprinting relations and the preservation potential of the microstructures considering the inferred stress history are discussed.

7.4.1. Microstructures indicative of microcracking

Healed microcracks indicating a stage of brittle deformation of quartz are discernible in all types of microstructures. Some are decorated with fluid inclusions visible in the optical microscope (Fig. 7.5c,d). Küster and Stöckhert (1999) proposed that truncation of these planar

arrays of fluid inclusions by mobile high angle grain boundaries can be taken as an indication of brittle failure at temperatures sufficient to allow subsequent deformation by dislocation creep. Experimental studies have shown that at these temperatures crack healing in quartz can be taken as instantaneous on geological time scales (Smith and Evans, 1984). Furthermore, the planar low angle grain boundaries decorated with fluid inclusions (Fig. 7.3b, c), which are observed by TEM in type A microstructures, may represent healed microcracks. The same holds true for discrete shear bands (Fig. 7.2a, b) with apparent offset in type A microstructures.

In contrast, evidence for microcracking in type C and D microstructures is largely restricted to the transgranular quartz-filled veinlets with a thickness of a few μm , mainly oriented perpendicular to the foliation in largely recrystallised quartz aggregates (Figs. 7.9c and 7.12a). The crosscutting relation, and the fact that the quartz crystals grown in the vein have adopted the CPO of the matrix, indicate that the veinlets formed after significant deformation of the quartz matrix by dislocation creep. Notably, the vein quartz has also undergone minor deformation by dislocation creep. This indicates that the brittle failure leading to formation of these veinlets took place at a late stage of deformation, when an increased pore fluid pressure allowed the formation of dilatant cracks. Independent evidence for an increase of pore fluid pressure during progressive deformation, approaching a near-lithostatic value at a final stage of creep, comes from the opening of cracks in cataclastically deformed garnet in rocks with type C and D microstructure, as discussed in Chapter 6.

The early-formed small scale microcracks, visible on the optical and in particular on the TEM scale in type A and B microstructures, were probably also formed in rocks now featuring type C and D microstructures, but have since been obliterated by subsequent recovery and recrystallisation. As such, type A and B microstructures, with limited recrystallisation, bear the record of an early stage of brittle deformation with a very high crack density, which was accompanied and followed by plastic flow. This stage of pervasive brittle failure is proposed to be related to synseismic loading, with dilatancy and increased permeability causing the quasi-instantaneous drop of pore fluid pressure (Küster and Stöckhert, 1999), which is prerequisite for crystal plastic flow at high differential stress.

7.4.2. Microstructures indicative of low-temperature plasticity

Notwithstanding the fact that the nature of sub-basal deformation lamellae, in particular on the TEM scale, remains a matter of debate (e.g. Christie and Ardell, 1974; Drury, 1993; McLaren et al. 1970; McLaren and Hobbs, 1972; White, 1973, 1975), Drury and Humphreys (1987) and Drury (1993) proposed that sub-basal deformation lamellae in quartz are indicative of glide-controlled deformation in the low-temperature plasticity field, being comparable to similar lamellae in metal alloys, which are only formed in that regime (McLaren et al., 1972; McLaren, 1991; Drury, 1993; Drury and Humphreys, 1986, 1987). Drury (1993) thus pointed out that the formation of deformation lamellae can possibly be taken as an indication for power law breakdown (e.g. Tsenn and Carter, 1987).

Previous TEM investigations have revealed that quite a number of different submicroscopic structures are associated with the optical-scale lamellae. In most cases the lamellae appear to be defined by arrays of elongate subgrains (McLaren and Hobbs, 1972; White, 1973; Blenkinsop and Drury, 1988; Drury, 1993), but can also be related to bands of variable dislocation density, or to planar arrays of fluid inclusions indicating microcracking (Christie and

Ardell, 1974; White, 1973, 1975; White and Treagus, 1975; Drury, 1993). As their submicroscopic structure reveals substantial recovery (White, 1973; Christie and Ardell, 1974; Drury, 1993), sub-basal lamellae cannot be taken as unmodified discrete slip bands. Instead, Drury (1993) proposed that during glide-controlled deformation, geometrically necessary dislocations are generated in a certain plane, with those of like sign repelling each other after accumulation of some strain. The dislocations are then proposed to leave the original glide plane by cross slip or climb and to combine with dislocations from other glide planes. This process could eventually lead to an array of elongate subgrains.

In the small scale shear zones investigated in this study, sub-basal deformation lamellae are most common in the type B microstructures (Figs. 7.5a and 7.7a). They are locally developed in the type A microstructures (Fig. 7.2b), and occasionally discernible in the type C microstructures (Fig. 7.9b). Regions with optically visible deformation lamellae in the type A microstructures show dislocation walls and poorly ordered low angle grain boundaries on the TEM scale (Fig. 7.3a). Although deformation lamellae on the optical scale are even more prevalent in the type B microstructures, no obviously correlated microstructure is discernible on the TEM-scale. This indicates that recovery has obliterated the original TEM-scale structure of the deformation lamellae, leaving an array of elongate subgrains with well-ordered low-angle grain boundaries, and elongate recrystallised grains (Fig. 7.8a, b), both with a diameter of less than a few micrometres. Extremely elongate subgrains are observed in type C microstructures (Fig. 7.11a to c), and locally even in type D microstructures (Fig. 7.14c). These TEM-scale microstructures are very similar to those described by McLaren and Hobbs (1972) from naturally deformed quartz from the Mt. Isa fault zone, north Queensland, Australia, the submicroscopic structures are attributed to non-steady state creep with strain hardening.

Notwithstanding the uncertain origin of deformation lamellae as slip bands or microcracks, the TEM-scale microstructures indicate extensive recovery after their formation, obliterating their original nature. On the scale accessible by the polarising microscope, however, they can still be discerned as arrays of planar features. If it is true that deformation lamellae are indicative of plastic deformation at high-stress (Drury 1993), the present finding is consistent with the stress history inferred from independent evidence. Deformation lamellae have formed during short term plastic, and eventually brittle, deformation related to synseismic loading, and were subsequently modified by recovery, which was effective at the prevailing temperatures of 300 to 350°C. This scenario could explain the wide variability of the reported submicroscopic structures related to deformation lamellae in natural quartz, which may in all cases indicate fluctuations in stress, with stages of short term high stress plastic deformation, at temperatures sufficient for recovery. Such conditions may be typically met in the uppermost plastosphere near the lower tip of seismically active crustal scale faults. The ambient temperatures and the subsequent cooling history then determine the degree of recovery and obliteration of the original microstructures, and thus the wide variability of the TEM-scale features observed in quartz with deformation lamellae.

Rapid deformation of quartz in the low-temperature plasticity regime is expected to lead to strain hardening, with a very high strength reached after a few percent of strain (e.g. Hobbs, 1968). The corresponding high free dislocation densities are not observed, however, but have obviously been reduced to moderate values on the order of 10^{12} to 10^{13} m^{-2} during recovery. However, a very high original density of geometrically necessary dislocations, which are now arranged in low angle grain boundaries, is indicated by the small subgrain size.

Dauphiné twins can originate as stress-induced deformation twins (Tullis, 1970; Barber and Wenk, 1991). Other possibilities comprise displacive transformation of β - to α -quartz (Heaney and Veblen, 1991; Markgraaff, 1986; Tullis, 1970) and low-temperature growth (Markgraaff, 1986), both being ruled out in the present case. Recent studies using the EBSD/SEM technique have shown that mechanical Dauphiné twins are a common feature in quartz from naturally deformed rocks in a wide range of geological environments, from diagenetic to amphibolite facies conditions (e.g. Lloyd, et al. 1992; Lloyd, 2000; Heidelbach et al., 2000; Neumann, 2000). As such, the Dauphiné twins - though probably stress-induced - are considered as unspecific microstructures, which do not provide further insight into the deformation history in the present context.

7.4.3. Microstructures indicative of recovery and recrystallisation

The arrangement of geometrically necessary dislocations into well ordered low-angle grain boundaries, observed in all microstructural types (e.g. Figs. 7.3b, 7.8c, 7.11 a-c), indicates effective recovery, leaving free dislocation densities on the order of 10^{12} to 10^{13} m^{-2} . Such dislocation densities correspond to the level commonly observed in quartz from metamorphic rocks (e.g. McLaren and Hobbs, 1972; White, 1976; Dresen et al., 1997; Stöckhert et al., 1999) and is well below that predicted for the high peak stresses in this study. Thus, the TEM-scale microstructure could principally be interpreted to result from recovery after early plastic deformation at high stress or to represent a late stage of creep after significant stress relaxation. Though a clear distinction is not feasible, the small subgrain size reflecting an extraordinarily high concentration of geometrically necessary dislocations is supposed to result from the early stage of glide-controlled deformation at very high differential stress. After formation by climb-controlled recovery in an early stage, the subgrains remained a stable microstructural feature, eventually becoming erased by recrystallisation during progressive deformation in type C and D microstructures. In contrast to the subgrains, the free dislocation density does not record the early deformation history.

Recrystallisation is commonly characterised as either rotation recrystallisation or migration recrystallisation (e.g. Guillopé and Poirier, 1979; Poirier, 1985). Also, recrystallisation that proceeds after or during deformation is referred to as static or dynamic respectively (e.g. Nicolas and Poirier, 1976; Gottstein and Mecking, 1985; Urai et al., 1986). Obviously, both classifications may be not truly appropriate in the present context. Widespread evidence of migration recrystallisation is found on both optical and TEM-scale, where high-angle grain boundaries are sutured (Fig. 7.3c, d), or small grains appear to replace deformed larger grains in a core and mantle type structure (Fig. 7.5c). Initial rotation recrystallisation can be inferred from the pronounced CPO observed in type D microstructures (Fig. 7.13), with a continuous transition from subgrains bound by low-angle grain boundaries to recrystallised grains bound by high-angle grain boundaries. This transition results from the increase of misorientation due to geometrically necessary dislocations being progressively incorporated into the boundary. Grain boundary mobility depends on misorientation (e.g. Cotterill and Mould, 1976; Urai et al., 1986; Stöckhert and Duyster, 1999), rendering migration recrystallisation effective as soon as misorientation causes the boundary structure to change from an ordered dislocation wall into a disordered true high-angle grain boundary. For type C and D microstructures subgrain formation is proposed to grade into rotation recrystallisation, eventually followed by migration recrystallisation. In contrast, in the type A and B microstructures migration recrystallisation is observed to occur predominantly at pre-existing high angle grain

boundaries, along small-scale shear bands, and at deformation lamellae. This indicates that in type A and B microstructures grain boundary migration is restricted to sites of pre-existing interfaces with a high degree of misorientation, or to sites of enhanced deformation due to local stress concentration.

Laboratory experiments have shown that quartz undergoes extreme strain hardening at high stress and strain rates (e.g. Hobbs, 1968). Transferred to the natural situation discussed here, this means that strain accumulated in the initial stage of glide controlled deformation may be very limited. In contrast, the microstructures of the investigated shear zones indicate a considerable finite strain (Küster and Stöckhert, 1999; Chapter 4), indicating that recovery and recrystallisation counteracted the increase of dislocation density during deformation. Thus, the frozen microstructures observed on the optical and TEM scale are interpreted to reflect dynamic recovery and recrystallisation during progressive deformation by dislocation creep in the course of stress relaxation. This interpretation is supported by the similarity of the natural microstructures to those found in laboratory experiments on dislocation creep of quartz by Hirth and Tullis (1992). Type A microstructures correspond to those developed in dislocation creep regime 1, and the fine-grained type C and D recrystallised aggregates with pronounced CPO correspond to the dislocation creep regime 3 of Hirth and Tullis (1992). It should be noted, however, that the natural record does not reflect a steady state situation in terms of stress and strain rate.

Notwithstanding the overprint of the early microstructures by subsequent deformation in the dislocation creep regime, some characteristic features, such as the deformation lamellae discernible on the optical scale and the very small elongate subgrains visible by TEM, can be attributed to the early stage of high-stress deformation. These specific features are ubiquitous in the type A microstructure and largely or completely missing in the type D microstructure, indicating that they were erased by migration recrystallisation, in particular where high strain was accumulated in the stage of deformation by dislocation creep.

7.4.4. Crystallographic preferred orientation

The pronounced crystallographic preferred orientation (CPO) associated with type C and D microstructures is related to the large amount of finite strain accumulated during deformation in the dislocation creep regime (e.g. Price, 1985). The CPO patterns reveal that basal $\langle a \rangle$ glide was the dominant slip system (Figs. 7.9 and 7.12), as expected for low to intermediate flow stress and greenschist-facies conditions (e.g. Hobbs, 1985; Schmid and Casey, 1986). In certain domains within type D microstructures, the CPO suggests that prism and rhombohedral $\langle a \rangle$ slip were also activated (Fig. 7.13), possibly due to local stress concentrations (Hobbs, 1985; Handy, 1990). In view of the highly inhomogeneous strain field on a larger scale, geometrical softening originating from the development of a pronounced CPO may have contributed to progressive localisation of deformation into the shear zones.

7.4.5. Microstructures indicative of grain growth

The type D microstructure reveals a characteristic foam structure on both the microscopic (Fig. 7.12c) and submicroscopic (Fig. 7.14a) scale. This foam structure is characterised by isometric grains with a diameter of a few micrometres, bound by planar or simply curved high angle grain boundaries meeting at near-120° angles along the grain edges, and a low free

dislocation density. Such foam microstructures are indicative of static grain growth, driven by the reduction of interfacial free energy (e.g. Cotterill and Mould, 1976; Evans et al., 2001). Grain growth requires temperatures sufficient for grain boundary migration, and a very low differential stress precluding concomitant deformation by dislocation creep (Stöckhert et al., 1997; Stöckhert and Duyster, 1999). Interfacial free energy is very low compared to elastic strain energy associated with an even moderate concentration of dislocations, and thus cannot control grain shape in materials undergoing deformation by dislocation creep. The observed foam structure thus indicates a final stage of annealing at very low differential stress, with temperatures still in the range of 300-350 °C, which is sufficient for grain growth in quartz (Stöckhert and Duyster, 1999). The observed grain size in type D microstructures with foam structure can thus be taken as an upper bound (Hacker et al. 1990, 1992) to the synkinematically recrystallised grain size during deformation by dislocation creep.

7.4.6. Paleopiezometers

The flow stress during steady state dislocation creep can be inferred from microstructural features (e.g. Poirier, 1985). Paleopiezometers based on recrystallised grain size, subgrain size, free dislocation density, and the spacing of deformation lamellae have been formulated and widely applied to natural rocks (e.g. Twiss, 1977, 1986; Ball and White, 1978; White, 1979a, b; Kohlstedt and Weathers, 1980; Christie and Ord, 1980; Koch and Christie, 1981; Etheridge and Wilkie, 1981; Ord and Christie, 1984), assuming that the steady state microstructures are not significantly modified during the later geological history. This basic prerequisite may not be met in general. Another source of uncertainty is inherent in the experimental calibration (e.g. Mercier, et al., 1977; Christie et al., 1980; Gleason and Tullis, 1993).

Clearly, two of the basic prerequisites for the application of the above paleopiezometers are not met in the material investigated in the present study. First, deformation of quartz took place not by steady state dislocation creep, but was markedly non-steady state, and second, extensive modification of the original microstructures during annealing is indicated by the TEM-scale observations. Therefore, first the stresses that may be indicated by the paleopiezometers are discussed, assuming that the increments during progressive development of the respective microstructures are sufficient to presume a near-steady state. In this case the paleopiezometers may provide an estimate of the flow stress at each respective stage. Then the preservation potential during subsequent modification by recovery, recrystallisation and grain growth are discussed.

Paleopiezometry based on deformation lamellae

Sub-basal deformation lamellae in quartz have been used as an empirical paleopiezometer. Their occurrence can be taken as an indication of high stress, as experimental studies have shown the lamellae to originate along planes where the shear stress amounts to about 100 to 200 MPa (e.g. Heard and Carter, 1968; Hirth and Tullis, 1992). Drury (1993) and Drury and Humphreys (1987) proposed that extensive development of deformation lamellae requires stresses above about 125-175 MPa. Koch and Christie (1981) have established an empirical relationship between the apparent spacing of the deformation lamellae in an optical microscope and stress magnitude, raising the possibility of using the lamellae as a paleopiezometer (Ord and Christie, 1984; McLaren, 1991). This relationship is of the form

$$\sigma_1 - \sigma_3 = c \cdot s^{-p} \quad (7.1)$$

where $\sigma_1 - \sigma_3$ is the differential flow stress in GPa; $c = 3.65 \text{ GPa } \mu\text{m}^p$; $p = 2.18$ for quartz (Koch and Christie, 1981) and s is the optically determined mean lamellar spacing in μm .

The optically derived mean spacing of deformation lamellae in this study is found to be within the range of 2.5 to 7 μm , for which the relation proposed by Koch and Christie (1981) indicates a differential stress of 0.1 to 0.5 GPa. Despite the shortcomings in theory and calibration of this paleopiezometer, the indicated maximum stresses of 0.5 GPa appear to be realistic as they correspond to the differential stress level derived from the orientation distribution of mechanically twinned jadeite crystals in adjacent metagranites (Chapter 5).

Paleopiezometry based on subgrain size

The theoretically derived relationship between subgrain size and flow stress (Twiss, 1977) has the form

$$\sigma_1 - \sigma_3 = B \cdot d^{-m} \quad (7.2)$$

where $\sigma_1 - \sigma_3$ is the steady-state differential stress in MPa, $B = 210 \text{ MPa } \mu\text{m}^m$, $m = 1$ and d is the subgrain size in μm . Experimental studies relating subgrain size to flow stress in experimentally deformed quartzite are not available.

The subgrain size is much smaller than the thickness of the thin section and thus cannot be resolved in the optical microscope. On the TEM-scale, subgrains are abundant (Figs. 7.3, 7.8, 7.11 and 7.14). Locally they are strongly elongate (Fig. 7.11 a-b) with a width $w = 0.5$ to 1.5 μm and a length $l = 4$ to 7 μm , similar in all investigated samples. The subgrain size is taken as $d = (w \cdot l)^{1/2}$. Rare isometric subgrains typically reveal a diameter $d = 0.5$ to 2 μm ; they may represent cross sections through mostly lath-shaped subgrains. Using the Twiss (1977) relation, the obtained subgrain sizes indicate a magnitude of flow stress of about 0.1 to 0.4 GPa.

Paleopiezometry based on recrystallised grain size

Relationships between flow stress and recrystallised grain size for quartzites have been proposed by Mercier et al. (1977), Twiss (1977), Christie et al. (1980), and Ord and Christie (1984). The theoretically derived calibration of Twiss (1977) is supported by experimental results obtained by Gleason and Tullis (1993). The relation proposed by Twiss (1977) has the form

$$\sigma_1 - \sigma_3 = A \cdot D^{-m} \quad (7.3)$$

where $\sigma_1 - \sigma_3$ denotes the differential stress in MPa, $A = 603 \text{ MPa } \mu\text{m}^m$, $m = 0.68$, and D is the recrystallised grain size in μm .

An average grain size, given as the diameter of a circle with equal area, in completely recrystallised quartz aggregates in the type D microstructure is about 5 to 10 μm , when determined from OC-images (Fig. 7.12c). In some TEM images an even smaller recrystallised grain size of 2 to 5 μm is discernible. Using the Twiss (1977) relation, the differential stresses range between about 0.1 and 0.4 GPa.

Paleopiezometry based on dislocation density

The relationship between the free dislocation density in quartz and the flow stress is given by the relation

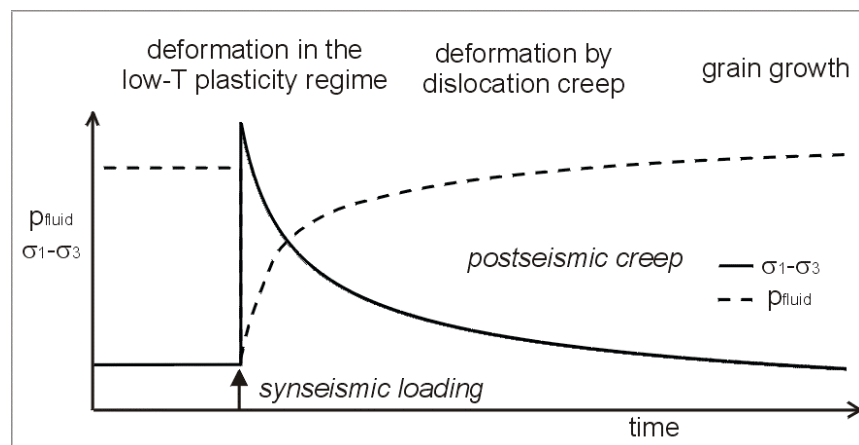
$$\sigma_1 - \sigma_3 = C \cdot N^p \quad (7.4)$$

where $\sigma_1 - \sigma_3$ is the steady-state differential stress in MPa; N is the dislocation density in cm^{-2} . $C = 1.64 \cdot 10^{-4}$, and $p = 0.66$ (McCormick, 1977; Ord and Christie, 1984). The experimentally derived relationship of McCormick (1977), supported by natural deformed quartzites (Ord and Christie, 1984), is preferred in this study. The differential stresses indicated by the observed free dislocation densities of $5 \cdot 10^{12}$ to $2 \cdot 10^{13} \text{ m}^{-2}$ are between 0.1 and 0.2 GPa.

7.4.7. Progressive evolution of the quartz microfabrics during post-seismic stress relaxation

The initial stage of glide-controlled deformation in the low-temperature plasticity regime, indicated by the widespread deformation lamellae, associated with brittle failure, indicated by healed microcracks, is proposed to be the result of synseismic loading (Fig. 7.15) during a large earthquake in the overlying schizosphere (Küster and Stöckhert, 1999; Chapter 1). During this stage, the peak differential stress has reached at least 0.5 GPa (Chapter 5). In view of the time scales inherent in the displacement along fault zones during earthquakes, imposed strain rates may have exceeded those typically applied in laboratory experiments. Under similar conditions, plastic deformation of quartz in the laboratory is characterised by extensive strain hardening (e.g. Hobbs, 1968), leading to a transient strength of several GPa after accumulation of a few percent of strain. Strain hardening may then allow fragmentation of embedded high-strength minerals as garnet (Chapter 6) and eventually lead to brittle failure of quartz.

Fig. 7.15: Proposed model for quartz deformation related to synseismic loading and postseismic creep.



After the earthquake, the displacement-induced stresses in the uppermost plastosphere are expected to decay, with the crust behaving as a Maxwell body (e.g. Ranalli, 1995) of unspecified length scale. The initial conditions during stress relaxation are provided by the peak stresses, which are limited by the ultimate strength of plastically deforming and hardening crust. The microstructures observed in the present study indicate that dislocation creep of quartz may be an important mechanism of stress relaxation. For the given temperatures of

about 300 to 350 °C, and an initial stress of about 0.5 GPa, experimentally derived flow laws can be used to derive strain rates. In this study the following power law for dislocation creep of synthetic quartzite is preferred

$$d\varepsilon/dt = A \exp(-Q/RT) \sigma^n \quad (7.5)$$

with the parameters $A = 6.5 \cdot 10^{-8} \text{MPa}^{-n} \text{s}$; $Q = 135 \pm 15 \text{ kJmol}^{-1}$; $n = 3.1$ proposed by Paterson and Luan (1990), as the extrapolation of this flow law to low natural strain rates on the order of 10^{-14} s^{-1} appears to be consistent with the microstructural record of natural rocks (Stöckhert et al., 1999; Hirth et al., 2001). Neglecting the proposed H_2O fugacity term (Evans and Kohlstedt, 1995; Hirth et al. 2001) appears to be justified in the present context for two reasons: First, the confining pressure of 0.3 GPa in the experiments by Paterson and Luan (1990) is close to the lithostatic pressure at the continental brittle-plastic transition for an average geotherm. Second, and more important, the fluctuations in pore fluid pressure discussed by Küster and Stöckhert (1999) (see Chapter 1 and 8) preclude the unequivocal definition of a H_2O fugacity for this natural situation.

The strain rates predicted by the flow law of Paterson and Luan (1990) for an initial peak stress of 0.5 GPa at 300 to 350 °C are on the order of 10^{-11} to 10^{-10} s^{-1} (Fig. 7.16). It should be noted, however, that 0.5 GPa is about the stress level where the power law is expected to break down (e.g. Tsenn and Carter, 1987). Also, excess dislocation densities introduced during short term plastic deformation need to be reduced by recovery before the predicted strain rates, based on a steady state microstructure, can be achieved. Depending on the rate of recovery, this may even lead to an initial increase of strain rate during stress relaxation. In the further course of stress relaxation the strain rates predicted by the power law decay rapidly, reaching the order of 10^{-13} s^{-1} at a stress level of about 0.1 GPa. Very low differential stress levels were reached in those rocks, where a final stage of grain growth driven by interfacial free energy is recorded.

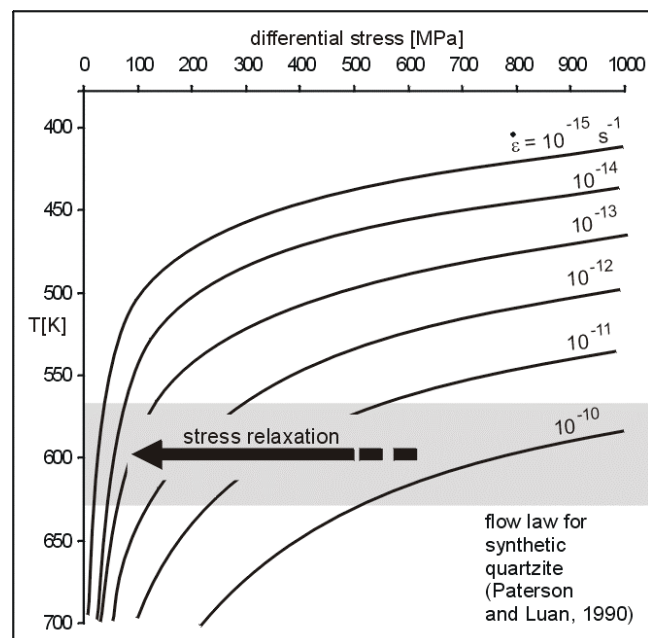


Fig. 7.16: T- σ diagram for the creep strength of quartz for different indicated strain rates. The quartz flow law is a power law derived by Paterson and Luan (1990). The estimated range of temperature and differential stress is given by the hatched field. See text for discussion.

The microstructural record of quartz investigated in this study is extremely heterogeneous, but it is throughout consistent with the above scenario, implying instantaneous loading causing plastic and brittle deformation at very high stresses, followed by dislocation creep and

finally low stress annealing. The heterogeneity is supposed to be partly due to small differences in temperature, which may amount to several tens of degrees C, simply related to paleodepth. However, there appears to be no systematic distribution of microstructural types within the investigated area, as revealed by the labelled sample locations in Fig. 7.1. This rules out temperature as the only reason of heterogeneity. Crustal inhomogeneity, with a wide variety of different rock types and pre-existing meso-scale structures can also cause a heterogeneous stress field on various length scales (Chapter 5). As strain rate is highly sensitive to stress for power law creep, and even more so for low-temperature plasticity, even small stress gradients may cause significant strain gradients, and thus contrasts in the microstructural record. Also to be considered is that strain accumulated in the early stage of synseismic loading in the low-temperature plasticity regime may be limited by strain hardening, as indicated the results of laboratory experiments on quartz (e.g. Hobbs, 1968). Localisation of deformation into shear zones then becomes pronounced during stress relaxation, when quartz is flowing in the dislocation creep regime, with progressive obliteration of the earlier record acquired in the low-temperature plasticity regime. The differences between the microstructural types A, B, C, and D may roughly correlate with an increasing amount of strain accumulated in the dislocation creep regime.

Another factor relevant for the formation of the different microstructural types could be the relative importance of recovery versus recrystallisation. Given identical temperature and stress history, small differences in the availability of water could have influenced the mobility of high angle grain boundaries (e.g. Urai, 1983; Urai et al. 1986). Notably, the highest bulk water content of 2500 to 4000 ppm H/Si has been found by FTIR microspectrometry in sample St 12 (type D microstructure), with a microstructural record indicating pronounced recrystallisation and final grain growth. The high angle grain boundaries are decorated with submicroscopic fluid inclusions. In contrast, the water content of quartz aggregates showing type A and B microstructures is mostly less than 1000 ppm H/Si, only exceptionally reaching 2500 ppm. A higher water content thus may cause recrystallisation to predominate over recovery, more effectively eliminating the high dislocation density introduced in the early stage of deformation in the low temperature plasticity regime compared to recovery, and thus facilitating flow in the dislocation creep stage.

Microcracking prior to or during plastic deformation might have increased the water content locally, consistent with healed microcracks decorated by fluid inclusions at the optical microscopic (Fig. 7.5c, d) and TEM scale (Fig. 7.3b, c). Introduction of this water from an external source (e.g. den Brok and Spiers, 1991) is indicated by the fact that the water content of quartz crystallised at high pressure metamorphism, and devoid of effects of the late stage deformation on the optical scale, is generally below the limit of detection, i.e. below 200 ppm H/Si (Meinecke, 1993). The water introduced in the early stage of distributed brittle failure and trapped in healed microcracks was possibly redistributed during subsequent deformation by dislocation creep, when the fluid inclusions were swept and drained by migrating high angle grain boundaries (Urai, 1983; Urai et al., 1986), with the fluid enhancing grain boundary mobility and thus making recrystallisation particularly effective.

In the present case study, the resulting quartz microstructures thus appear to be primarily controlled by (1) local stress history and (2) the relative rates of recovery and recrystallisation. The latter can be influenced by the availability of water, that was inhomogeneously introduced along cracks during the early stage of synseismic loading and then redistributed along migrating high angle grain boundaries (e.g. Urai, 1983; Urai et al., 1986) during the subsequent stage of dislocation creep. This concept contrasts with the commonly proposed

correlation between the microstructural record of quartz and even small differences in temperature (e.g. Voll, 1976; Dunlap et al., 1997; Stöckhert et al., 1999; Hirth et al., 2001). Though the studied area provides a particularly conspicuous example, with very high peak stresses achieved in a possibly single large earthquake, the basic principle is considered to be valid in general. However, in many cases the record of loading and relaxation may be blurred by successive cycles superimposed upon each other, corresponding to the size-frequency distribution of earthquakes (e.g. Scholz, 1990), during progressive cooling. In the case of smaller earthquakes with short recurrence times compared to cooling history, the microstructural record of quartz may be dominated by the effect of temperature.

7.5. Conclusions

The peculiar stress history recorded by the rocks of the Sesia Zone, attributed to synseismic loading and postseismic creep in the uppermost plastosphere, with an extraordinarily high magnitude of peak stresses followed by stress relaxation and reconstitution of a near-lithostatic pore fluid pressure, as inferred from the microstructures of other minerals, is also reflected by the microstructural record of quartz. This record is governed by (1) short term deformation at very high stresses in the low-temperature plasticity field during synseismic loading, with limited finite strain due to strain hardening, followed by (2) dislocation creep at decreasing stresses and strain rates during stress relaxation, with dynamic recovery and recrystallisation, and finally (3) quasi static recovery and – after reduction of dislocation density to very low values - grain growth driven by interfacial free energy.

The microstructural record is thus the result of a sequence of processes that are superimposed on each other at nearly uniform temperature, but decaying differential stresses. Thus, flow was markedly non-steady state. At stage (1), strain rates may have even exceeded typical laboratory strain rates for a very short time, whereas dislocation creep at the given temperatures and peak stresses may have started, depending on the rate of recovery, with strain rates on the order of 10^{-10} s^{-1} for the indicated peak stresses. The strain rates then decayed during stress relaxation.

The observed large variety of quartz microstructures is principally consistent with this sequence of processes. The record acquired in the successive stages is not uniform, however. The differences in the microstructures are attributed to small differences in temperature (as a function of paleodepth), in the initially accumulated plastic strain (as a function of position with respect to the fault tip), and in the degree of strain localisation during stress relaxation (possibly depending on mesoscopic inhomogeneity and structure). Also, the relative importance of recovery and recrystallisation may be influenced by the non-uniform availability of water, enhancing grain boundary mobility. In view of the markedly non-steady state deformation history the usual paleopiezometers are of limited value, as their theory and experimental calibration require steady state dislocation creep.

In the present case study, the microfabrics of quartz acquired in the brittle-plastic transition zone are stress-controlled rather than simply a result of successive overprinting at decreasing temperature. Thus, they provide insight into the processes of short term deformation of the uppermost plastosphere related to earthquakes, with information on peak stresses and stress history otherwise not accessible. Such results may be significant for the understanding of the earthquake cycle, for the inversion of related geodetic data, and for the modelling of syn- and postseismic deformation.

8. Branching quartz veins

8.1. Introduction

During major earthquakes fractures can propagate downward into the uppermost plastosphere (e.g. Sibson, 1980; Scholz, 1988; Yeats, 1997; see Chapter 1.2). Related fluid flow is episodic and dominated by dilatancy and transient fracture permeability (e.g. McCaig, 1988; Peltzer et al., 1996; Bosl and Nur, 2000; Husen and Kissling, 2001). Fluid influx into the open cracks can induce localised reduction of the pore fluid pressure, enhancing precipitation of quartz along fractures (O'Hara, 1990).

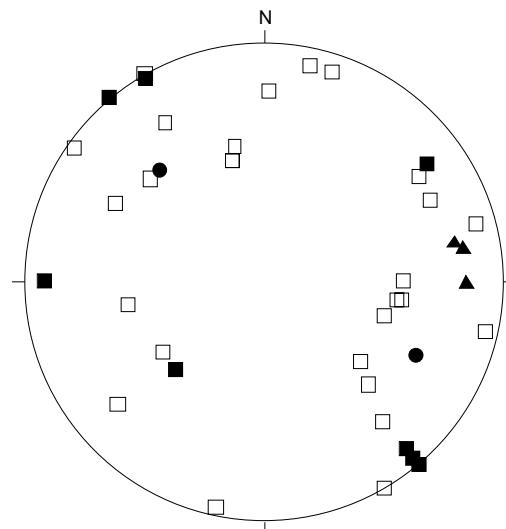
Discordant quartz veins developed from fractures are widespread in the Sesia Zone. Many are branching and form networks. Branching fractures are indicative of rapid crack propagation (e.g. Atkinson, 1987; Lawn, 1993) and thus suspected to develop during earthquakes. This chapter is concerned with the micro- and mesoscopic structure of the branching quartz veins and their relation to seismic activity.

8.2. Mesoscopic structures

Discordant, branching quartz veins are oriented at a large angle to the main foliation of the eclogitic gneisses and micaschist (Fig. 7.8.2a, b). Some quartz veins can reach a considerable width of several metres and are mined in quarries (e.g. cava di quarzo, NE of Nomaglio in the lower Aosta valley). The orientation of the discordant quartz veins is variable, with a dip angle between 50 and 90° (Fig. 7.8.1).

Fig. 8.1: Orientation of discordant quartz veins.

- poles of discordant quartz veins from the lower Aosta valley.
- poles of discordant quartz veins from Val Chuisella.
- ▲ poles of discordant quartz veins from Mt. Mucrone.
- poles of discordant quartz veins from Bard.



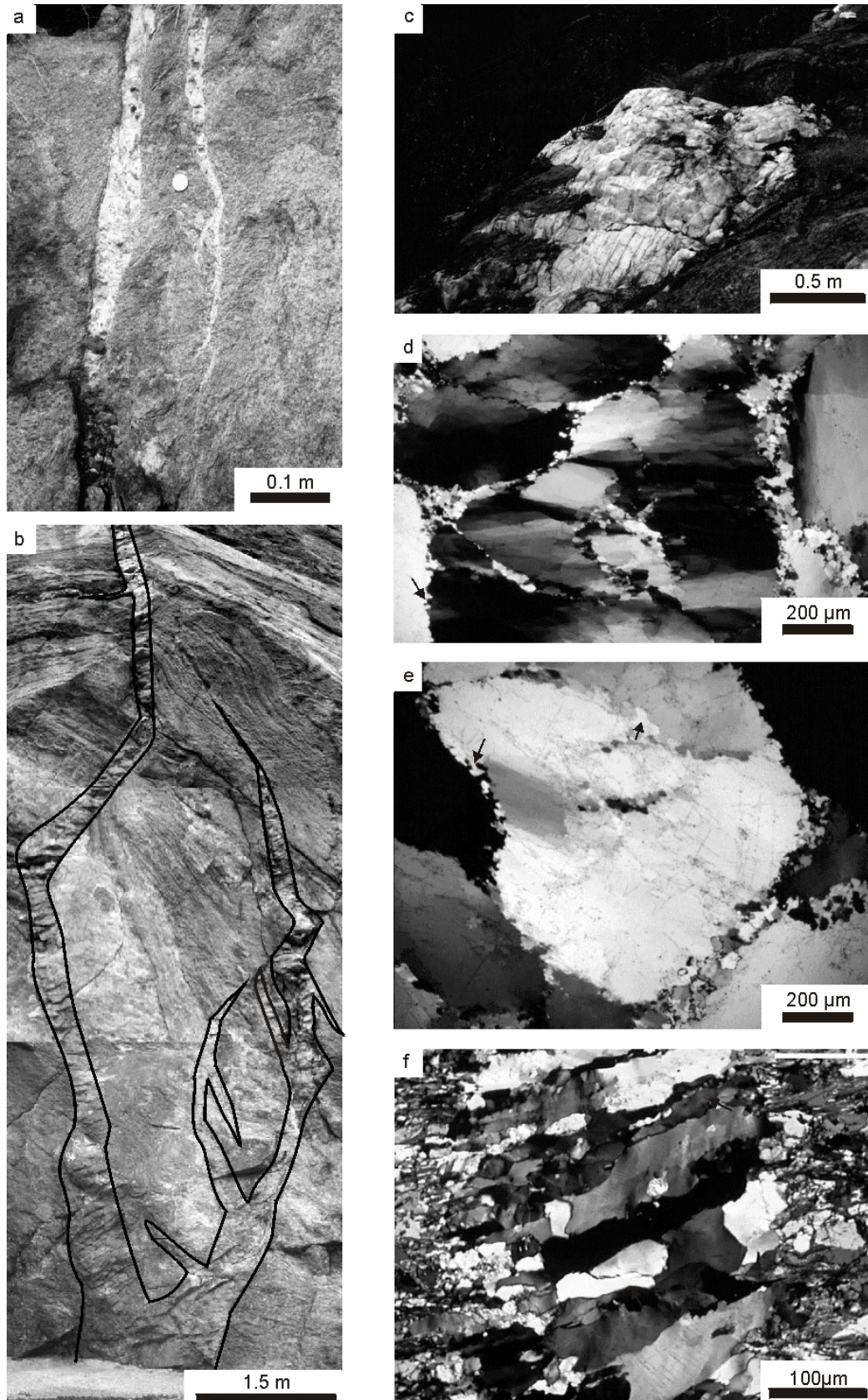


Fig. 8.2a, b, c: Branching, discordant quartz veins. **Fig. 8.2d, e:** Optical micrograph taken with crossed polars of quartz microstructure from the branching quartz vein (sample CT191 and CT192) in 8.2b, showing undulous extinction, subgrains and sutured high-angle boundaries (arrows). **Fig. 8.2f:** Optical micrograph taken with crossed polars of a small discordant quartz vein (sample CT143) perpendicular to the foliation of the host micaschist. The quartz in the vein reveals undulatory extinction, sutured high angle boundaries, deformation lamellae, and deformation bands.

8.3. Microstructures

The quartz microstructure in these veins indicates plastic deformation. The quartz crystals reveal elongated subgrains parallel to the c-axis (Fig. 8.2d), implying that basal $\langle a \rangle$ glide was an activated slip system. The high-angle grain boundaries are sutured with a wavelength of about 20–30 μm (Fig. 8.2d, e). New grains with a similar diameter as the amplitudes of the sutures occur at the rim of large grains, forming a core and rim structure. These observations suggest that strain-induced grain boundary migration was activated. In a small quartz vein perpendicular to the foliation of the host micaschist, deformation lamellae and deformation bands in quartz can be observed (Fig. 8.2f).

The microstructure of the discordant, branching quartz veins suggests that subsequent to fracturing plastic deformation by dislocation creep took place.

8.4. Discussion and conclusions

The quartz veins discordant with the Alpine foliation suggest development from open fissures by brittle failure. The branching of these veins is proposed to reflect unstable and high velocity fracture propagation (e.g. Atkinson, 1987; Lawn, 1993). Rapid crack propagation can be expected during seismic rupture.

Fluid influx into the open fractures may have led to a localised drop in pore fluid pressure. The solubility of silica reveals a positive dependence on pressure (e.g. Manning, 1994). Therefore, the reduction in pore fluid pressure may have caused the precipitation of quartz along the fractures.

The precipitated quartz was progressively deformed by dislocation creep, as indicated by the microstructures, with the original microstructures largely obliterated. Therefore temperatures must have been high enough to allow dislocation creep of quartz, i.e. higher than 300°C, as indicated by experimental flow laws (e.g. Paterson and Luan, 1990) and by the microstructural record of naturally deformed rocks (e.g. Stöckhert et al., 1999; Hirth et al., 2001). Assuming a simple thermal history, the occurrence of fractures sealed with plastically deformed and recrystallised quartz is indicative of brittle failure at temperatures above 300°C. It cannot be ruled out, however, that the rocks underwent a complex thermal history. At the same time, there is no evidence for this assumption. It seems to be most favourable, that the discordant quartz veins have developed due to the downward propagation of cracks into a crustal level at temperatures between 300–350°C during seismic rupture, with the branching being consistent with a high rate of synseismic loading.

These discordant, branching quartz veins are proposed to represent a synseismically induced fracture system in the uppermost plastosphere, due to the penetration of fractures into the transitional regime according to the Sibson-Scholz conceptual fault model (see Chapter 4.1). Such a fracture system is suspected to cause a transient change of seismic scattering properties around the source region of earthquakes as observed by Baisch (2000) and Baisch and Bokelmann (2001) (see Chapter 1.2).

9. General discussion and conclusions

9.1. Introduction

The objective of this thesis was an assessment of criteria for synseismic loading and post-seismic creep in the uppermost plastosphere by investigating the microstructural record of exhumed rocks from the Sesia Zone. The purpose of this final chapter is to draw general conclusions based on the findings presented in the preceding chapters.

9.2. Microstructural criteria for syn- and postseismic deformation

The microstructures are rather peculiar: Jadeite crystals reveal mechanical twinning (Chapter 5). The microstructural record of quartz (Chapter 7) is highly heterogeneous. Sub-basal deformation lamellae, arrays of elongate subgrains on the TEM-scale and healed microcracks indicate an early stage of glide-controlled deformation at high stresses accompanied by distributed brittle failure. Very fine-grained recrystallised aggregates with a pronounced crystallographic preferred orientation reflect intense plastic flow by dislocation creep. Locally, a foam microstructure indicates a final stage of static grain growth at low differential stress. The high-strength mineral garnet embedded in a quartz matrix underwent complex cataclastic deformation by initial extensive fragmentation (Chapter 6). Subsequent displacement of the fragments by sliding along the cracks is caused by the flow of the surrounding quartz matrix. Garnet fragments were finally slightly pulled apart with quartz and feldspar precipitated from the fluid phase in the open cracks.

Plastic flow under such extraordinary high differential stresses requires a high effective confining pressure - after the Goetze criterion which empirically predicts plastic flow for the effective confining pressure exceeding the differential stress - and therefore presumes sublithostatic pore fluid values. However, at the crustal level below the BST, pore fluid pressure (p_f) is generally presumed to be close to the mean stress with $p_f \approx (\sigma_1 + \sigma_2 + \sigma_3)/3$, hence it is thought to be approximately lithostatic. Lithostatic pressure in the lower Aosta valley was evaluated by Küster and Stöckhert (1999) from the composition of newly formed phengites and the densities of stretched early-formed fluid inclusions to be about 400-500 MPa at temperatures of about 300-350°C. However, these authors also report that a sublithostatic pore fluid pressure is implied by low density fluid inclusions ($p_f \approx 150-300$ MPa at 300-350°C) along healed fractures in quartz. These findings indicate pore fluid pressure fluctuations.

Branching veins sealed with plastically deformed and recrystallised quartz (Chapter 8) are proposed to reflect fissures propagating downward into the uppermost plastosphere. Fluid influx into these fractures may have caused a transient drop of the pore fluid pressure, allowing creep in the plastic regime at the high stress conditions suggested by the microstructural record. Restoration of a near-lithostatic pore fluid pressure in the final stage of postseismic creep is reflected by slight opening and sealing of the cracks in garnet (Chapter 6).

Indications of the simultaneous or intermittent occurrence of brittle and plastic deformation are also obvious on the microscopic scale by the generation of pseudotachylytic zones concomitant with plastic deformation of quartz (Chapter 4) and recrystallised veins at a high angle to the foliation of mylonites (Chapter 4 and 7), as well as on the submicroscopic scale by straight, parallel low angle grain boundaries in quartz decorated with fluid inclusions (Chapter 7). A locally pervasive cataclastic disintegration of some rocks cannot be ruled out

in some places. Shear bands and sets of deformation lamellae in the quartz matrix of some mylonitic micaschist are observed to be oriented parallel to fractures adjacent in garnet (Fig. 6.1c and Fig. 7.2b) and thus may represent healed continuous, transgranular cracks.

In summary, the investigated microstructures are proposed to record syn- and postseismic deformation in the uppermost plastosphere (Fig. 9.1), with:

- (1) fractures propagating downward causing a drop of pore fluid pressure
- (2) high peak stresses exceeding 0.5 GPa during synseismic loading;
 - mechanical twinning of jadeite, initial fragmentation of garnet and glide-controlled deformation of quartz in the low-temperature plasticity regime, took place
- (3) stress relaxation primarily controlled by dislocation creep of quartz;
 - flow of the quartz matrix caused displacement of garnet fragments by sliding along the fractures
- (4) eventual restoration of a near-lithostatic pore fluid pressure;
 - at this stage slight opening and sealing of the cracks in garnet and minor static grain growth of quartz took place.

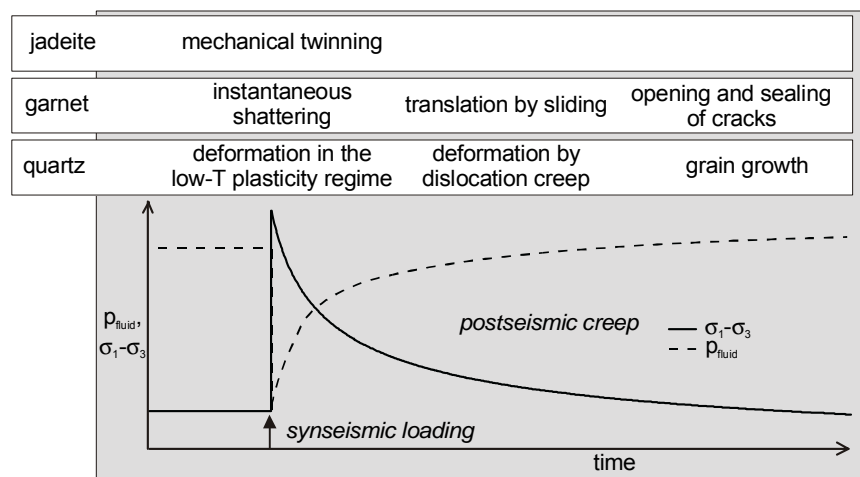


Fig. 9.1: Proposed model relating the microstructural record of rocks from the Sesia Zone to synseismic loading and postseismic creep.

9.3. Time and length scales during deformation

The area, where microstructural criteria for this syn- and postseismic deformation are recorded, is distributed over at least 300 km² in the Sesia Zone. However, the mesoscopic structures reflect a highly inhomogeneous strain field due to a high degree of localisation. Strain is concentrated in centimetre- to metre-scale zones (mylonites, ultramylonites, pseudotachylytes) and is remarkably low in the intervening rocks (Chapter 4). Also, the microstructural record from the mechanically twinned jadeite (Chapter 5) suggests an inhomogeneous and complex strain field.

High strain rates are predicted from flow laws for the dislocation creep of quartz at the inferred conditions of 0.5 GPa and temperatures in the range of 300–350°C (see Chapter 7, Fig. 7.16). At initial stages of stress relaxation they are probably at least on the order of 10¹⁰ s⁻¹. Küster and Stöckhert (1999) argued, that the small strain accumulated in most of the

rocks together with the predicted high strain rates for the differential stress and the given temperatures suggests that the deformation proceeded within very short time spans: For a strain rate of 10^{-10} s^{-1} , a strain of 30% would accumulate in only 100 years and in $10^4 - 10^3$ years at strain rates of 10^{-12} to 10^{-11} s^{-1} .

High differential stress and strain rate together with the short duration of deformation can explain the inhomogeneous strain field and localisation, as complex natural structures and heterogeneities can cause local stress concentration and may lead to strong variation of the accumulated strain. This can be due to many factors including small temperature gradients and the various rock properties (e.g. grain size, mineral constituents, water content), as well as the crystallographic orientation and the orientation of the pre-existing foliation with respect to the imposed stresses.

Altogether, the high differential stress and the rather low accumulated strain indicate a short duration of deformation with a very high rate of loading to peak stresses and a high relaxation rate.

9.4. Tectonic boundary conditions

The investigated late stage high-stress deformation is assumed to have taken place before 35 Ma (see Chapter 3). Küster and Stöckhert (1999) presumed an active thrust regime, as the Alps were in a stage of convergence at that time (e.g. Coward and Dietrich, 1989). The apparent high differential stress during deformation recorded by the investigated microstructures also imply an active thrust regime. That is, because a thrust regime assumes higher maxima stresses in the lithosphere, compared to a normal and a strike-slip regime (see Chapter 1.2.1, Fig. 1.2). However, short-term deformation with rapid loading and relaxation precludes that it was driven directly by a far-field tectonic stress. The stress field related to the mode of loading in the uppermost plastosphere is proposed to reveal a large heterogeneity and complexity. Therefore, the distribution of mechanically twinned jadeite, indicating a nearly vertical orientation of the major principal stress, σ_1 (see Chapter 5, Fig. 5.6), cannot be expected to be consistent with a far-field tectonic stress. Additionally, a rotation of the rocks after mechanical twinning, possibly during uplift, cannot be ruled out.

9.5. Earthquake recurrence

Large-scale earthquake rupturing is considered to be related to multiple cycles of stress and elastic strain energy accumulation, with intermittent, abrupt stress and energy release accompanying each major rupture event (e.g. Sibson, 1986), involving complex deformation processes and perturbation in the Earth's crust (see Chapter 1.2). Seismic motions along major fault zones are constrained to the schizosphere (e.g. Sibson, 1977; Tse and Rice, 1986; Scholz, 1988, 1990). Rapid, episodic, but aseismic, creep is predicted to occur in the uppermost plastosphere, whereas at greater depths, continuous creep is suspected and is only modestly perturbed by major earthquakes in the overlying schizosphere (Tse and Rice, 1986; Sibson, 1986). These creep processes at great depth are considered to reload the seismogenic zone (Cohen, 1981; Tse and Rice, 1986), causing the recurrence of seismic rupture. Plastic flow beneath the BPT may even act to release the initial loading (Tse and Rice, 1986; Yeats, 1997). The period of the loading cycle, the earthquake recurrence, is the time between subsequent rupturing on a given segment of fault (Scholz, 1990). The possibili-

ties to study the recurrence of major earthquakes are limited because for many areas of the world, one complete seismic cycle has not yet been documented (Scholz, 1990) and can be expected to be on the order of several hundreds or thousands of years.

The investigated microstructures reveal postseismic creep in the uppermost plastosphere within a geological short time on the order of 10^2 - 10^4 years. The finite accumulated strain observed in the rocks could well be accumulated in several shorter increments, due to episodic creep following multiple seismic events. However, due to cumulative strain and the low preservation potential of certain microstructures, structural features developed in one particular cycle are liable to be overprinted or obliterated by deformation during subsequent cycles. For this reason multiple seismic events are difficult to recognise. The different types of quartz microstructures, the alternating activation of plastic and brittle mechanisms, and the generation of pseudotachylytic zones at Mt. Mucrone may be related to different or multiple seismic cycles, although other explanation are also conceivable (Chapter 7 and 4). Thus, it cannot be ruled out that the deformation, which is recorded by the investigated microstructures, is related to more than one seismic cycle, but it is not evident from the microstructural record.

9.6. Conclusions

The microstructures of the exhumed metamorphic rocks from the Sesia Zone give evidence of highly non steady-state deformation with fluctuations in stress and pore fluid pressure, consistent with synseismic loading and postseismic creep in the uppermost plastosphere.

This example reveals

- (1) that the stresses in the uppermost plastosphere can transiently exceed 0.5 GPa with strain rates on the order of 10^{-10} s⁻¹,
- (2) that the microstructures of exhumed, metamorphic rocks can detect regions of seismic activity in the geological past and
- (3) that they provide insight into the processes within the uppermost plastosphere during and after major earthquakes.

10. References

- Angelier J., Mechler P. (1977) Sur une methode graphique de recherche des contraintes principales également utilisable en tectonique et en sésimologie: la methode de dièdres droits. *Bull. Soc. Geol. France* 19: 1309-1318.
- Atkinson B.K. (1987) *Fracture Mechanics of Rock*. Academic Press.
- Austrheim H., Boundy T.M. (1994) Pseudotachylytes generated during seismic faulting and eclogitization of the deep crust. *Science* 265: 82-83.
- Austrheim H., Erambert M., Boundy T.M. (1996) Garnets record in deep crustal earthquakes. *Earth Planet. Sci. Lett.* 193: 223-238.
- Avé Lallement H.G. (1978) Experimental deformation of diopside and websterite. *Tectonophysics* 48: 1-27.
- Avé Lallement H.G., Carter N.L. (1971) Pressure dependence of quartz deformation lamellae orientations. *Am. J. Sc.* 270: 218-235.
- Avigad D. (1996) Pre-collisional ductile extension in the internal western Alps (Sesia zone, Italy). *Earth Planet. Sci. Lett.* 137: 175-188.
- Baisch S. (2000) Zur Messung zeitlicher Veränderungen seismischer Wellenausbreitungseigenschaften in der oberen Erdkruste. *Ber. Inst. Geol. Min. Geophys. Ruhr-Univ. Bochum Reihe A Nr. 57*.
- Baisch S., Bokelmann G.H.R. (2001) Seismic waveform attributes before and after the Loma Prieta earthquake: Scattering change near the earthquake and temporal recovery. *J. Geophys. Res.* 106: 16323-16337.
- Ball S., White S. (1978) On the deformation of quartzite. *Phys. Chem. Minerals* 3: 163-172.
- Barber D.J., Wenk H.R. (1991) Dauphiné twinning in deformed quartzites: implications of an in situ TEM study of the α - β phase transformation. *Phys. Chem. Min.* 17: 492-502.
- Belfield W.C., Twiss R.J. (1981) Brittle- semi-brittle- ductile transitions in Heavitree quartzite. *EOS Trans. Am. Geophys. Un.* 62: 1029.
- Blenkinsop T.G., Drury M.R. (1988) Stress estimates and fault history from quartz microstructures. *J. Struct. Geol.* 10: 673-684.
- Bosl W.J., Nur A. (2000) Crustal fluids and earthquakes. *Geophys. Monogr.* 120: 267-284.
- Boullier A.M. (1980) A preliminary study on the behaviour of brittle minerals in a ductile matrix: example of zircon and feldspars. *J. Struct. Geol.* 2: 211-217.
- Brace W.F., Kohlstedt D.L. (1980) Limits on lithospheric stress imposed by laboratory experiments. *J. Geophys. Res.* 85: 6248-6252.
- Brockenbrough J.R., Suresh S., Wienecke H.A. (1991) Deformation of metal-matrix composites with continuous fibres: geometrical effects of fibre distribution and shape. *Acta. metall. mater.* 39: 735-752.
- Burkhard M. (1993) Calcite twins, their geometry, appearance and significance as stress-strain markers and indicators of tectonic regime. *J. Struct. Geol.* 15: 351-368.
- Byerlee J.D. (1978) Friction of rocks. *Pure Appl. Geophys.* 116: 615-626.
- Carter N.L., Raleigh C.B. (1969) Principal stress directions from plastic flow in crystals. *Geol. Soc. Am. Bul.* 80: 1231-1264.
- Chen W.-P., Molnar P. (1983) Focal depths of intracontinental and intraplate earthquakes and their implications for the thermal and mechanical properties of the lithosphere. *J. Geophys. Res.* 88: 4183-4214.

- Christie J.M., Ardell A.J. (1974) Substructures of Deformation Lamellae in Quartz. *Geology* 2: 405-408.
- Christie J.M., Ord A. (1980) Flow stress from microstructures of mylonites: example and current assessment. *J. Geophys. Res.* 85: 6253-6262.
- Christie J.M., Ord A., Koch P.S. (1980) Relationship between recrystallized grain size and flow stress in experimentally deformed quartzite. *EOS Trans. Am. Geophys. Un.* 61: 377.
- Clyne T.W., Withers P.J. (1993) An Introduction to Metal Matrix Composites. Cambridge University Press.
- Cohen S.C. (1981) Postseismic rebound due to creep of the lower lithosphere and asthenosphere. *Geophys. Res. Lett.* 8: 4933-496.
- Compagnoni R. (1977) The Sesia-Lanzo Zone: high pressure-low temperature metamorphism in the austroalpine continental margin. *Rend. Soc. It. Mineral. Petrogr.* 33: 335-374.
- Compagnoni R., Dal Piaz G.V., Hunziker J.C., Gosso G., Lombardo B., Williams P.F. (1977) The Sesia-Lanzo Zone, a slice of continental crust with alpine high pressure-low temperature assemblages in the western Italian Alps. *Rend. Soc. It. Mineral. Petrogr.* 33: 281-334.
- Compagnoni R., Maffeo B. (1973) Jadeite-bearing metagranites I. s. and related rocks in the Mount Mucrone Area (Sesia-Lanzo Zone, Western Italian Alps). *Schweiz. Mineral. Petrogr. Mitt.* 53: 355-378.
- Cotterill P., Mould P.R. (1976) Recrystallization and Grain Growth in Metals. Surrey University Press, London.
- Coward M., Dietrich D. (1989) Alpine tectonics – an overview. In: Coward M.P., Dietrich D., Park R.G. (eds.), *Alpine Tectonics*. Geol. Soc. London, Spec. Publ. 45: 1-29.
- Daquan Y., Yucheng C., Xuezheng L., Jie L. (2000) Microscopic textures in rocks deformed by chemical explosion and experimental stick-slip as a guide to conditions of paleoseismicity. *J. Asian Earth Sciences* 18: 33-39.
- Degenhardt J.J., Buchanan P.C., Reid A.M., Miller R. McG. (1994) Breccia veins and dykes associated with Roter Kamm Crater, Namibia. *Geological Society of America, Special Paper* 293: 197-208.
- DeMets C. (1997) Afterslip no longer an afterthought. *Nature* 386: 549.
- Den Brok S.W.J., Spiers C.J. (1991) Experimental evidence for water weakening of quartzite by microcracking plus solution-precipitation creep. *J. Geol. Soc. Lon.* 148: 541-548.
- Dresen G., Duyster J., Stöckhert B., Wirth R., Zulauf G. (1997) Quartz dislocation microstructure between 7000 m and 9100 m depth from the Continental Deep Drilling Program KTB. *J. Geophys. Res.* 102: 18,443-18,452.
- Drury M.R. (1993) Deformation lamellae in metals and minerals. In: Boland J.N., Fitzgerald J.D. (eds.), *Defects and processes in the solid state: geoscience applications - The McLaren volume, Developments in Petrology*, 14. Elsevier 195-212.
- Drury M.R., Humphreys F.J. (1986) The development of microstructures in Al-5% Mg during high temperature deformation. *Acta metall.* 34: 2259-2271.
- Drury M.R., Humphreys F.J. (1987) Deformation lamellae as indicator of stress level. *EOS Trans. Am. Geophys. Un.* 44: 1471.
- Dunlap W. J., Hirth G., Teyssier C. (1997) Thermomechanical evolution of a ductile duplex. *Tectonics* 16: 983-1000.
- Duyster J. (1996) StereoNett 2.0, University of Bochum.
- Engelder T. (1993) *Stress regimes in the lithosphere*. Princeton University Press.
- Etheridge M.A., Wilkie J.C. (1981) An Assessment of dynamically recrystallized grain size as a paleopiezometer in quartz-bearing mylonite zones. *Tectonophysics* 78: 475-508.

- Evans B., Kohlstedt D.L. (1995) Rheology of rocks. In: Ahrens T.J. (ed.), *Rock physics and phase relations - A handbook of physical constants*. Ref. Shelf, Am. Geophys. Un. vol. 3 148-165.
- Evans B., Renner J., Hirth G. (2001) A few remarks on the kinetics of static grain growth in rocks. *Int. J. Earth Sciences* 90: 88-103.
- Gleason G.C., Tullis J. (1993) Improving flow laws and piezometers for quartz and feldspar aggregates. *Geophys. Res. Lett.* 20: 2111-2114.
- Godard G., van Roermund H.L.M. (1995) Deformation-induced clinopyroxene fabrics from eclogites. *J. Struct. Geol.* 17: 1425-1443
- Goetze C., Evans B. (1979) Stress and temperature in the bending lithosphere as constrained by experimental rock mechanics. *Geophys. J.R. astron. Soc.* 59: 463-478.
- Gottstein G., Mecking H. (1985) Recrystallization. In: Wenk, H.R. (Ed.), *Preferred orientation in deformed metals and rocks – an introduction to modern texture analysis*. Academic Press, New York, pp. 183-218.
- Grawinkel A., Stöckhert B. (1997) Hydrostatic pore fluid pressure to 9 km depth – Fluid inclusion evidence from the KTB deep drill hole. *Geophys. Res. Lett.* 24: 3273-3276.
- Guillopé M., Poirier J.P. (1979) Dynamic recrystallization during creep of single-crystalline halite: an experimental study. *J. Geophys. Res. (B)*, 84: 5557-5567.
- Hacker B.R., Kirby S.H. (1993) High-pressure deformation of calcite marble and its transformation to aragonite under non-hydrostatic conditions. *J. Struct. Geol.* 15: 1207-1222.
- Hacker B.R., Yin A., Christie J.M., Davis G.A. (1992) Stress magnitude, strain rate, and rheology of extended middle continental crust inferred from quartz grain sizes in the Whipple Mountains, California. *Tectonics* 11: 36-46.
- Hacker B.R., Yin A., Christie, J.M. (1990) Differential stress, strain rate and temperature of mylonitization in the Ruby Mountains, Nevada: Implications for the rate and duration of uplift. *J. Geophys. Res.* 95: 8569-8580.
- Handy M.R. (1990) The solid state flow of polymineralic rocks. *J. Geophys. Res.* 95: 8647-8662.
- Heaney P.J., Veblen D.R. (1991) Observation and kinetic analysis of a memory effect at the α - β quartz transition. *Am. Mineral.* 76: 1459-1466.
- Heard H.C., Carter N.L. (1968) Experimentally induced "natural" intragranular flow in quartz and quartzite. *Am. J. Sc.* 266: 1-42.
- Heidelberg F., Kunze K., Wenk H.R. (2000) Texture analysis of a recrystallized quartzite using electron diffraction in the scanning electron microscope. *J. Struct. Geol.* 22: 91-104.
- Heki K., Miyazaki S.-I., Tsuji H. (1997) Silent fault slip following an interplate thrust earthquake at the Japan Trench. *Nature* 386: 595-598.
- Hickman S.H. (1991) Stress in the lithosphere and the strength of active faults. *Rev. of Geophys.* 29 (Suppl.): 759-775.
- Hirth G., Teyssier C., Dunlap W.J. (2001) An evaluation of quartzite flow laws based on comparisons between experimentally and naturally deformed rocks. *Int. J. Earth Sciences* 90: 77-87.
- Hirth G., Tullis J. (1989) The effects of pressure and porosity on the micromechanics of the brittle-ductile transition in quartzite. *J. Geophys. Res.* 94: 17825-17838.
- Hirth G., Tullis J. (1992) Dislocation creep regimes in quartz aggregates. *J. Struct. Geol.* 14: 145-159.
- Hirth G., Tullis J. (1994) The brittle-plastic transition in experimentally deformed quartz aggregates. *J. Geophys. Res.* 99: 11,731-11,748.
- Hobbs B.E. (1985) The geological significance of microfabric analysis. In: Wenk H.-R. (ed.), *Preferred orientation in deformed metals and rocks: An introduction to modern texture analysis*. Academic Press 463-484.

- Hobbs B.E. (1968) Recrystallization of single crystals of quartz. *Tectonophysics* 6: 353-401.
- Huenges E., Erzinger J., Kück J. (1997) The permeable crust: Geohydraulic properties down to 9101 m depth. *J. Geophys. Res.* 102: 18255-18265.
- Hurford A.J., Hunziker J.C., Stöckhert B. (1991) Constraints on the late thermotectonic evolution of the Western Alps: evidence for episodic rapid uplift. *Tectonics* 10: 758-769.
- Husen S., Kissling E. (2001) Postseismic fluid flow after the large subduction earthquake of Antofagasta, Chile. *Geology* 29: 847-850.
- Inger S., Ramsbotham W., Cliff R.A., Rex D.C. (1996) Metamorphic evolution of the Sesia-Lanzo-Zone, Western Alps: Time constraints from multi-system geochronology. *Contrib. Mineral. Petrol.* 126: 152-168.
- Ivins E.R. (1996) Transient creep of a composite lower crust 2. A polymineralic basis for rapidly evolving postseismic deformation modes. *J. Geophys. Res.* 101: 28005-28028.
- Ji S., Zhao P. (1994) Strength of two-phase rocks: a model based on fiber-loading theory. *J. Struct. Geol.* 16: 253-262.
- Ji S., Zhao P., Saruwatari K. (1997) Fracturing of garnet crystals in anisotropic metamorphic rocks during uplift. *J. Struct. Geol.* 19: 603-620.
- Kenkmann T., Dresen G. (1998) Stress gradients around porphyroclasts: paleopiezometric estimates and numerical modelling. *J. Struct. Geol.* 20: 163-173.
- Kirby S.H., Christie J.M. (1977) Mechanical Twinning in Diopside $\text{Ca}(\text{Mg,Fe})\text{Si}_2\text{O}_6$: Structural mechanism associated crystal defects. *Phys. Chem. Mineral.* 1: 137-163.
- Koch N., Masch L. (1992) Formation of Alpine mylonites and pseudotachylytes at the base of the Silvretta nappe, Eastern Alps. *Tectonophysics* 204: 289-306.
- Koch P.S., Christie J.M. (1981) Spacing of deformation lamellae as a paleopiezometer. *EOS Trans. Am. Geophys. Un.* 62: 1030.
- Kohlstedt D., Evans B., Mackwell S.J. (1995) Strength of the lithosphere: Constraints imposed laboratory experiments. *J. Geophys. Res.* B9: 17587-17602.
- Kohlstedt D.L., Weathers M.S. (1980) Deformation-induced microstructures, paleopiezometers, and differential stresses in deeply eroded fault zones. *J. Geophys. Res.* 85: 6269-6285.
- Kollé J.J., Blacic J.D. (1982) Deformation of single-crystal clinopyroxenes: 1 Mechanical twinning in diopside and hedenbergite. *J. Geophys. Res.* 87: 4019-4034.
- Kranz R. L. (1983) Microcracks in rocks: a review. *Tectonophysics* 100: 449-480.
- Kronenberg A.K., Wolf G.H. (1990) Fourier transform infrared spectroscopy determinations of intragranular water content in quartz-bearing rocks: implications for hydrolytic weakening in the laboratory and within the earth. *Tectonophysics* 172: 255-271.
- Küster M., Stöckhert B. (1999) High differential stress and sublithostatic pore fluid pressure in the ductile regime – microstructural evidence for short term post-seismic creep in the Sesia Zone, Western Alps. *Tectonophysics* 303: 263-277.
- Lawn B.R. (1993) *Fracture of Brittle Solids*. Cambridge University Press 2nd edition.
- Li V.C., Rice J.R. (1987) Crustal Deformation in Great California Earthquake Cycles. *J. Geophys. Res.* 92: 11533-11551.
- Liermann H.-P., Isachsen C., Altenberger U., Oberhänsli R. (2002) Behavior of zircon during high-pressure, low-temperature metamorphism: Case study from the Internal Unit of the Sesia Zone (Western Italian Alps). *Eur. J. Mineral.* 14: 61-71.
- Lloyd G.E. (1985) Review of instrumentation, techniques and applications of SEM in mineralogy. In: White J.C. (ed.), *Applications of Electron Microscopy in the Earth Sciences*. Mineral. Assoc. Can.

- Short Course 11: 151-188.
- Lloyd G.E. (1987) Atomic number and crystallographic contrast images with the SEM: a review of backscattered electron techniques. *Min. Mag.* 51: 3-19.
- Lloyd G.E. (2000) Grain boundary contact effects during faulting of quartzite: an SEM/EBSD analysis. *J. Struct. Geol.* 22: 1675-1693.
- Lloyd G.E., Freeman B. (1991) SEM electron channelling analysis of dynamic recrystallization in a quartz grain. *J. Struct. Geol.* 13: 945-953.
- Lloyd G.E., Knipe R.J. (1992) Deformation mechanisms accommodating faulting of quartzite under upper crustal conditions. *J. Struct. Geol.* 14: 127-143.
- Lloyd G.E., Law R.D., Mainprice D., Wheeler J. (1992) Microstructural and crystal fabric evolution during shear zone formation. *J. Struct. Geol.* 14: 1079-1100.
- Mainprice D.H., Paterson M.S. (1984) Experimental studies of the role of water in the plasticity of quartzites. *J. Geophys. Res.* 89: 4257-4269.
- Mandal N., Chakraborty C., Samanta S.K. (2001) Controls on the failure mode of brittle inclusions hosted in a ductile matrix. *J. Struct. Geol.* 23: 51-66.
- Manning C.E. (1994) The solubility of quartz in H₂O in the lower crust and upper-mantle. *Geochim. Cosmochim. Acta* 58: 4831-4839.
- Markgraaff J. (1986) Elastic behavior of quartz during stress induced dauphiné twinning. *Phys. Chem. Mineral.* 13: 102-112.
- Marshall D.J. (1988) Catodoluminescens of geological materials. Unwin Hyman.
- Martin B., Röller K. (1989). DAFI 1.2, University of Bochum.
- Mawer C.K., Williams P.F. (1985) Crystalline rocks as possible paleoseismicity indicators. *Geology* 13: 100-102.
- McCaig A. (1988) Deep fluid circulation in fault zones. *Geology* 16: 867-870.
- McCormick J.W. (1977) Transmission electron microscopy of experimentally deformed synthetic quartz. PhD thesis, University of California.
- McLaren A.C. (1991) Transmission electron microscopy of minerals and rocks. Cambridge University Press.
- McLaren A.C., Hobbs B.E. (1972) Transmission electron microscope investigation of some naturally deformed quartzites. *Geophys. Monogr.* 16: 55-66.
- McLaren A.C., Turner R.G., Boland J.N. (1970) Dislocation structure of the deformation lamellae in synthetic quartz; a study by electron and optical microscopy. *Contrib. Mineral. Petr.* 29: 101-115.
- McNulty B.A. (1995) Pseudotachylite generated in the semi-brittle and brittle regimes, Bench Canyon shear zone, central Sierra Nevada. *J. Struct. Geol.* 17: 1507-1521.
- Meinecke J. (1993) Spezifikation und Verteilung von Wasser in gesteinsbildendem Quarz in Beziehung zu Kristallisationsbedingungen, Druck-, Temperatur- und Verformungsgeschichte. PhD thesis, University of Bochum.
- Mercier J.-C.C., Anderson D.A., Carter N.L. (1977) Stress in the lithosphere: inferences from steady-state flow of rocks. *J. Pure Appl. Geophys.* 115: 199-226.
- Neumann B. (2000) Texture development of recrystallised quartz polycrystals unravelled by orientation and misorientation characteristics. *J. Struct. Geol.* 22: 1695-1711.
- Neuser R. (1995) A new high-intensity cathodoluminescence microscopy and its application to weakly luminescing minerals. *Bochumer Geologisch-Geotechnische Arbeiten* 44: 116-118.
- O'Hara K. (1990) Brittle-plastic deformation in mylonites: An example from the Meadow Fork thrust,

- western Blue Ridge province, southern Appalachians. *Geol. Soc. Am. Bull.* 102: 1706-1713.
- Oberhänsli R., Hunziker J.C., Martinotti G., Stern W.B. (1985) Geochemistry, geochronology and petrology of Monte Mucrone: An example of eo-alpine eclogitization of permian granitoids in the Sesia-Lanzo Zone, Western Alps. *Italy. Chem. Geol.* 52: 165-184.
- Ord A., Christie J.M. (1984) Flow stresses from microstructures in mylonitic quartzites of the Moine Thrust zone, Assynt area, Scotland. *J. Struct. Geol.* 6: 639-654.
- Pardavi-Horváth, M. (1984) Microhardness and brittle fracture of garnet single crystals. *J. Mater. Sci.* 19: 1159-1170.
- Passchier C.W. (1982) Pseudotachylyte and the development of ultramylonite bands in the Saint Barthélemy Massif, French Pyrenes. *J. Struct. Geol.* 4: 69-79.
- Paterson M.S. (1982) the determination of hydroxyl by infrared absorption in quartz, silicate glasses and similar materials. *Bull. Mineral.* 105: 20-29.
- Paterson M.S. (1989) The interaction of water with quartz and its influence in dislocation flow – an overview. In: Karato S.-I. and Toriumi M., (eds.), *Rheology of Solids and of the Earth*. Oxford University Press 107-142.
- Paterson M.S., Luan F.C. (1990) Quartzite rheology under geological conditions. In: Knipe R.J., Rutter E.H. (eds.), *Deformation mechanisms, rheology and tectonics*. Geol. Soc. London, Spec. Publ. 54: 299-307.
- Peltzer G., Rosen P., Rogez F., Hundnut K. (1996) Postseismic rebound in Fault-Step-Overs caused by pore fluid pressure. *Science* 273: 1202-1204.
- Pognante U. (1989) Lawsonite, blueschist and eclogite formation in the southern Sesia Zone (Western Alps, Italy). *Eur. J. Mineral.* 1: 89-104.
- Poirier J.-P. (1985) *Creep of crystals – High temperature deformation processes in metals, ceramics and minerals*. Cambridge University press.
- Pollitz F.F., Wicks C., Thatcher W. (2001) Mantle flow beneath a continental strike-slip fault: postseismic deformation after the 1999 Hector Mine earthquake. *Science* 293: 1814-1818.
- Price G.P. (1985) Preferred orientations in quartzites. In: Wenk, H.R. (Ed.), *Preferred orientation in deformed metals and rocks – an introduction to modern texture analysis*. Academic Press, New York, pp. 385-406.
- Prior D.J. (1993) Sub-critical fracture and associated retrogression of garnet during mylonitic deformation. *Contrib. Mineral. Petrol.* 113: 545-556.
- Prior D.J., Trimby P.W., Weber D.U., Dingley D. (1996) Orientation contrast imaging of microstructures in rocks using foreshatter detectors in the scanning electron microscope. *Min. Mag.* 60: 859-869.
- Prior D.J., Wheeler J., Brenker F., Harte B., Matthews M. (2000) Crystal plasticity of natural garnet: New microstructural evidence. *Geology* 28: 1003-1006.
- Prior J.P., Bolyle A.P., Brenker F., Cheadle M.C., Day A., Lopez G., Peruzzo L., Potts G.J., Reddy S., Spiess R., Timms N.E., Trimby P., Wheeler J., Zetterström L. (1999) The application of electron backscatter diffraction and orientation contrast imaging in the SEM to textural problems in rocks. *Am. Mineral.* 84: 1741-1759.
- Raleigh C.B., Talbot J.L. (1967) Mechanical twinning in naturally and experimentally deformed diopside. *Am. J. Sci.* 265: 151-165.
- Ranalli G. (1995) *Rheology of the earth*. Chapman and Hall, 2nd edition.
- Reimanis I.E., Petrovic J.J., Mitchell T.E. (1994) The fracture behaviour of single –crystal Y3Al5O12. *Journal of Non-Crystalline Solids* 177: 67-73.

- Rice J.R., Gu J.C. (1983) Earthquake aftereffects and triggered seismic phenomena. *Pageoph.* 121: 187-219.
- Richter F. (1984) Deformation und Metamorphose in der alpinen Subduktionszone: Die Sesia-Lanzo-Zone im unteren Val d'Aosta, Norditalien. PhD thesis, University of Bonn.
- Rowe K.J., Rutter E.H. (1990) Palaeostress estimation using calcite twinning: experimental calibration and application to nature. *J. Struct. Geol.* 12: 1-17.
- Rubatto D., Gebauer D., Compagnoni R. (1999) Dating of eclogite-facies zircons: the age of Alpine metamorphism in the Sesia-Lanzo Zone (Western Alps). *Earth Planet. Sci. Lett.* 167: 141-158.
- Sabadini R., Yuen A., Boschi E. (1984) The effects of postseismic motions on the moment of inertia of a stratified viscoelastic earth with an asthenosphere. *Geophys. J. R. Astron. Soc.* 79: 727-745.
- Schaff D.P., Beroza G.C., Shaw B.E. (1998) Postseismic response of repeating aftershocks. *J. Geophys. Res. Lett.* 25: 4549-4552.
- Schmid S., Casey M. (1986) Complete fabric analysis of some commonly observed quartz c-axis patterns. *Geophys. Monogr.* 36: 263-286
- Schmid S.M., Aebli H.R., Heller F., Zingg A. (1989) The role of the Periadriatic Line in the tectonic evolution of the Alps. In: Coward M.P., Dietrich D., Park R.G. (eds.), *Alpine Tectonics*. Geol. Soc. London, Spec. Publ. 45: 153-171.
- Schmidt N.H., Olesen N. (1989) Computer-aided determination of crystal-lattice orientation from electron-channeling patterns in the SEM. *Can. Mineral.* 27: 15-22.
- Scholz C.H. (1988) The brittle-plastic transition and the depth of seismic faulting: *Geologische Rundschau* 77: 319-328.
- Scholz C.H. (1990) *The mechanics of earthquakes and faulting*. Cambridge University press.
- Shimamoto T., Kanaori Y., Asai K.-I. (1991) Cathodoluminescence observations on low-temperature mylonites: potential for detection of solution-precipitation microstructures. *J. Struct. Geol.* 13: 967-973.
- Sibson R. H. (1980) Transient discontinuities in ductile shear zones. *J. Struct. Geol.* 2: 165-171.
- Sibson R.H. (1975) Generation of pseudotachylite by ancient seismic faulting. *Geophys. J. R. Stron. Soc.* 43: 775-794.
- Sibson R.H. (1977) Fault rocks and fault mechanisms. *J. Geol. Soc. Lond.* 133: 191-213.
- Sibson R.H. (1984) Roughness at the base of the seismogenic zone: contributing factors. *J. Geophys. Res.* 89: 5791-5799.
- Sibson R.H. (1986) Earthquakes and rock deformation in crustal fault zones. *Ann. Rev. Earth Planet. Sci.* 14: 149-175.
- Sibson, R.H. (1990) Fluids in tectonically active regimes of the continental crust. *Mineralogical Association of Canada* 18: 93-132.
- Smith D.L., Evans B. (1984) Diffusional crack healing in quartz. *J. Geophys. Res.* 89: 4125-4135.
- Solomon S.C., Richardson R.M., Bergman E.A. (1980) Tectonic stress: models and magnitudes. *J. Geophys. Res.* 85: 6086-6092.
- Spang J.S. (1972) Numerical Method for Dynamic Analysis of Calcite Twin Lamellae. *Geol. Soc. Am. Bul.* 83: 467-472.
- Spang J.S. (1974) Numerical dynamic analysis of calcite twin lamellae in the Greenport Center Syncline. *Am. J. Sci.* 274: 1044-1058.

- Spiess R., Peruzzo L., Prior D.J., Wheeler J. (2001) Development of garnet porphyroblasts by multiple nucleation, coalescence and boundary misorientation driven rotations. *J. Metam. Geol.* 19: 269-290.
- Spray J.G. (1987) Artificial generation of pseudotachylyte using friction welding apparatus: simulation of melting on a fault plane. *J. Struct. Geol.* 9: 49-60.
- Spray J.G. (1992) A physical basis for the frictional melting of some rock-forming minerals. *Tectonophysics* 204: 205-221.
- Stel H. (1986) The Effect of Cyclic Operation of Brittle and Ductile Deformation on the Metamorphic Assemblage in Cataclasites and Mylonites. *Pure Appl. Geophys.* 124: 289-307.
- Stöckhert B., Brix M.R., Kleinschrodt R., Huford A.J., Wirth R. (1999) Thermochronometry and microstructures of quartz – a comparison with experimental flow laws and predictions on the temperature of the brittle-plastic-transition. *J. Struct. Geol.* 21: 351-369.
- Stöckhert B., Duyster D. (1999) Discontinuous grain growth in recrystallised vein quartz – implications for grain boundary structure, grain boundary mobility, crystallographic preferred orientation, and stress history. *J. Struct. Geol.* 21: 1477-1490.
- Stöckhert B., Jäger E., Voll G. (1986) K-Ar age determinations on phengites from the internal part of the Sesia Zone, Western Alps, Italy. *Contrib. Mineral. Petrol.* 92: 456-470.
- Stöckhert B., Massonne H.-J.; Nowlan E. U. (1997) Low differential stress during high-pressure metamorphism; the microstructural record of a metapelite from the Eclogite Zone, Tauern Window, Eastern Alps. *Lithos* 41: 103-118.
- Stünitz H., Gerald J.D.F. (1993) Deformation of granitoids at low metamorphic grade. II: Granular flow in albite-rich mylonites. *Tectonophysics* 221: 299-324.
- Swanson M.T. (1992) Fault structure, wear mechanisms and rupture processes in pseudotachylyte generation. *Tectonophysics* 204: 223-242.
- Tharp T.M. (1983) Analogies between the high-temperature deformation of polyphase rocks and the mechanical behavior of porous powder metal. *Tectonophysics* 96: T1-T11.
- Tse S.T., Rice J.R. (1986) Crustal earthquake instability in relation to the depth variation of frictional slip properties. *J. Geophys. Res.* 91: 9452 – 9472.
- Tsenn M.-C., Carter N.-L. (1987) Upper limits of power law creep of rocks. *Tectonophysics*. 136: 1-26.
- Tullis J. (1970) Quartz: Preferred orientation in rocks produced by Dauphiné twinning. *Science* 168: 1342-1344.
- Tullis J. (1990) Experimental studies of deformation mechanisms and microstructures in quartzofeldspathic rocks. In: Barber D., Meridith P. (eds.), *Deformation Processes in Minerals, Ceramics, and Rocks*. Unwin and Hyman. 190-227.
- Tullis J., Yund R.A. (1987) Transition from cataclastic flow to dislocation creep of feldspar: Mechanisms and microstructures. *Geology* 15: 606-609.
- Tullis T.E. (1980) The use of mechanical twinning in minerals as a measure of shear stress magnitudes. *J. Geophys. Res.* 85: 6263-6268.
- Turner F.J. (1953) Nature and dynamic interpretation of deformation in calcite of three marbels. *Amer. J. Sci.* 251: 276-298.
- Twiss R.J. (1977) Theory and applicability of a recrystallized grain size paleopiezometer. *Pageoph.* 115: 227-244.
- Twiss R.J. (1986) Variable sensitivity piezometric equations for dislocation density and subgrain diameter and their relevance to olivine and quartz. *Geophys. Monogr.* 36: 247-261.

- Urai J., Means W.D., Lister, G.S. (1986) Dynamic recrystallization of minerals. In: Hobbs, B.E., Heard, H.C. (Eds.), Mineral and rock deformation: laboratory studies. *Geophys. U. Geophys. Monogr.* 36: 161-200.
- Urai J.L. (1983) Water assisted dynamic recrystallization and weakening in polycrystalline bischofite. *Tectonophysics* 96: 125-157.
- Valentino A.J., Sclar C.B. (1981) Parting in giant garnets as an indicator of late brittle deformation at Gore Mountain, Warren County, N.Y.. *Geophys. Res. Lett.* 8: 883-885.
- van-Daalen M., Heilbronner R., Kunze K. (1999) Orientation analysis of localized shear deformation in quartz fibres at the brittle-ductile transition. *Tectonophysics* 303: 83-107.
- Venturini G. (1995) Geology, geochemistry and geochronology of the inner central Sesia Zone, Western Alps – Italy. *Mémoires de Géologie* No. 25.
- Vergnolle M., Pollitz F.F., Calais E. (2001) GPS results in Mongolia, post-seismic deformation and implications on crust/mantle viscosity in Central Asia. *EOS Trans. AGU* 82(47), *Fall Meet. Suppl.*, Abstract G31A-0130, F267.
- Voll G. (1976) Recrystallization of quartz, biotite and feldspars from Erstfeld to the Leventina nappe, Swiss Alps, and its geological significance. *Schweiz. mineral. petrogr. Mitt.* 56: 641-647.
- Vollbrecht A., Stipp M., Olesen N.O. (1999) Crystallographic orientation of microcracks in quartz and inferred deformation processes: a study on gneisses from the German Continental Deep Drilling Project (KTB). *Tectonophysics* 303: 279-297.
- Wang Z., Ji S. (1999) Deformation of silicate garnets: Brittle-ductile transition and its geological implications. *Can. Min.* 37: 525-541.
- Wendt A.S., D'Arco P., Goffé B., Oberhänsli R. (1993) Radial cracks around a quartz inclusions in almandine: Constraints on the metamorphic history of the Oman mountains. *Earth Planet. Sci. Lett.* 114: 449-461.
- Wenk H.-R. (1970) Submicroscopical Twinning in Lunar and Experimentally Deformed Pyroxenes. *Contrib. Mineral. Petrol.* 26: 315 – 323.
- Wheeler J., Prior D.J., Jiang Z., Spiess R., Trimby P.W. (2001) The petrological significance of misorientations between grains. *Contrib. Mineral. Petrol.* 141: 109-124.
- White J.C. (1996) Transient discontinuities revisited: pseudotachylyte, plastic instability and the influence of flow fluid pressure on deformation processes in the mid-crust. *J Struct. Geol.* 18: 1471-1486.
- White S. (1973a) Deformation lamellae in naturally deformed quartz. *Nat. Phys. Sc.* 245: 26-28.
- White S. (1973b) Dislocations and bubbles in vein quartz. *Nat. Phys. Sc.* 243: 11-14.
- White S. (1973c) Syntectonic recrystallisation and texture development in quartz. *Nature* 244: 276-278.
- White S. (1975) The effects of polyphase deformation on the intracrystalline defect structures of quartz. II. Origin of the defect structures. *N. Jb. Miner. Abh.* 123: 237-252.
- White S. (1977) Geological significance of recovery and recrystallization processes in quartz. *Tectonophysics* 39: 143-170.
- White S. (1979a) Grain and sub-grain size variations across a mylonite zone. *Contrib. Mineral. Petrol.* 70: 193-202.
- White S. (1979b) Paleo-stress estimates in the Moine Thrust Zone, Eriboll, Scotland. *Nature* 280: 222-223.
- White S., Treagus J.E. (1975) The effects of polyphase deformation on the intracrystalline defect structures of quartz. I. The defect structures. *N. Jb. Miner. Abh.* 123: 219-236.

- White S.H., Burrows S.E., Carreras J., Shaw N.D., Humphreys F.J. (1980) On mylonites in ductile shear Zones. *J. Struct. Geol.* 2: 175-187.
- White S.H. (1976) The role of dislocation processes during tectonic deformation with special reference to quartz. In: Strens, R.J. (Ed.), *The physics and chemistry of minerals and rocks*. pp. 75-91.
- Whitney D.L. (1996) Garnets as open systems during regional metamorphism. *Geology* 24: 147-150.
- Whitney D.L., Cooke M.L., Du Frane S.A. (2000) Modeling of radial microcracks at corners of inclusions in garnet using fracture mechanics. *J. Geophys. Res.* 105: 2843-2853.
- Williams P.F., Compagnoni R. (1983) Deformation and metamorphism in the Bard area of the Sesia Lanzo Zone, Western Alps, during subduction and uplift. *J. Metam. Geol.* 1: 117-140.
- Yeats R.S., Sieh K., Allen D.R. (1997) *The Geology of Earthquakes*. Oxford University Press.
- Zhao P., Ji S. (1997) Refinements of shear-lag model and its applications. *Tectonophysics* 279, 37-53.

List of samples

Sample	Geographic co-ordinates	Study area	Rock type
St12	409 E, 5043 N	Lower Aosta valley	Mylonitic micaschist
CT183	409. 416E, 5043. 518N	Lower Aosta valley	Mylonitic micaschist
CT82	418. 486E, 5053. 212N	Mt. Mucrone	Mylonitic garnet gneiss
CT32	409. 816E, 5043. 812N	Lower Aosta valley	Ultramylonite in metagranite
CT134	409. 816E, 5043. 812N	Lower Aosta valley	Ultramylonite in metagranite
CT152	407. 415E, 5044. 531N	Lower Aosta valley	Ultramylonite in metagranite
HB9	409 E, 5043 N	Lower Aosta valley	Ultramylonite in micaschist
CT207	418. 486E, 5053. 212N	Mt. Mucrone	Pseudotachylyte in garnet gneiss
CT208	418. 486E, 5053. 212N	Mt. Mucrone	Pseudotachylyte in garnet gneiss
CT209	418. 486E, 5053. 212N	Mt. Mucrone	Pseudotachylyte in garnet gneiss
CT210	418. 486E, 5053. 212N	Mt. Mucrone	Pseudotachylyte in garnet gneiss
CT8	411. 622E, 5042.308N	Lower Aosta valley	Metagranite
CT25	409. 816E, 5043. 812N	Lower Aosta valley	Metagranite
CT110	409. 816E, 5043. 812N	Lower Aosta valley	Metagranite with ultramylonite
CT20	409. 880E, 5043. 910N	Lower Aosta valley	Jadeite gneiss/metaaplite
CT163	413.114E, 5045. 720N	Lower Aosta valley	Mylonitic quartz vein
CT210	409. 416E, 5043. 518N	Lower Aosta valley	Mylonitic quartz vein
CT216	409. 555E, 5043. 528N	Lower Aosta valley	Mylonitic quartz vein
CT176	398. 877E, 5042. 129N	Val Chuisella	Mylonitic quartz vein
CT177	398. 877E, 5042. 129N	Val Chuisella	Mylonitic quartz vein
CT232	401. 490E, 5040. 885N	Val Chuisella	Mylonitic quartz vein
CT233	398.616E, 5042.385N	Val Chuisella	Mylonitic quartz vein
CT143	409.555E, 5043. 528N	Lower Aosta valley	Discordant quartz vein
CT191	402. 624E, 5050. 708N	Bard	Discordant quartz vein
CT192	402. 624E, 5050. 708N	Bard	Discordant quartz vein

EMP analyses

Feldspar analyses

	mylonite from Mt. Mucrone; CT82						ultramylonite from the lower Aosta valley; CT32			
	anorthoclase		oligoclase		K-feldspar		albite porphy- roclast		albite in matrix	
SiO₂	67.01	67.60	65.31	65.57	64.19	63.78	68.08	67.93	67.50	66.84
Al₂O₃	21.08	20.27	22.49	21.90	18.82	18.40	19.31	19.38	19.15	19.23
FeO	0.01	0.00	0.00	0.09	0.40	0.01	0.04	0.00	0.10	0.10
MgO	0.00	0.00	0.00	0.00	0.00	0.01	0.03	0.00	0.03	0.02
MnO	0.04	0.01	0.04	0.00	0.03	0.00	0.00	0.02	0.05	0.00
TiO₂	0.02	0.02	0.02	0.02	0.04	0.00	0.03	0.03	0.02	0.02
Na₂O	9.84	10.36	9.31	9.79	0.31	0.34	11.43	11.58	11.45	10.95
K₂O	0.13	0.07	0.14	0.21	16.15	16.46	0.08	0.07	0.31	0.91
BaO	0.00	0.00	0.00	0.00	0.00	0.14	0.00	0.11	0.00	0.00
CaO	1.63	0.72	3.00	2.19	0.14	0.00	0.02	0.01	0.06	0.02
Total	99.75	99.04	100.31	99.77	100.08	99.16	99.05	99.14	98.67	98.13
Cation on 8 O basis										
Si	2.93	2.97	2.86	2.88	2.97	2.98	3.00	2.99	2.99	2.99
Al	1.09	1.05	1.16	1.14	1.03	1.01	1.00	1.01	1.00	1.01
Fe	0.00	0.00	0.00	0.00	0.02	0.00	0.00	0.00	0.00	0.00
Mg	0.00	0.00	0.00	0.00	0.00	0.00	0.00	0.00	0.00	0.00
Mn	0.00	0.00	0.00	0.00	0.00	0.00	0.00	0.00	0.00	0.00
Ti	0.00	0.00	0.00	0.00	0.00	0.00	0.00	0.00	0.00	0.00
Na	0.84	0.88	0.79	0.83	0.03	0.03	0.98	0.99	0.98	0.95
K	0.01	0.00	0.01	0.01	0.95	0.98	0.00	0.00	0.02	0.05
Ba	0.00	0.00	0.00	0.00	0.00	0.00	0.00	0.00	0.00	0.00
Ca	0.08	0.03	0.14	0.10	0.01	0.00	0.00	0.00	0.00	0.00
Σ	4.94	4.95	4.96	4.97	5.00	5.02	4.99	5.00	5.01	5.01
Mol per cent										
Ab	90.89	95.90	84.21	87.87	2.84	3.03	99.44	99.54	97.97	94.72
Or	0.81	0.40	0.81	1.25	96.47	96.97	0.44	0.42	1.76	5.17
An	8.31	3.70	14.98	10.89	0.69	0.00	0.11	0.05	0.27	0.11

Table 1: Selected feldspar analyses.

Jadeite analyses

	CT20	CT20	CT20	CT20	CT25	CT25	CT25	CT30	CT30	CT30
SiO₂	58.05	57.96	57.79	57.87	58.30	57.81	57.95	58.37	58.53	58.37
Al₂O₃	22.58	22.15	21.57	21.19	24.51	23.80	23.24	24.35	24.46	24.11
TiO₂	0.08	0.05	0.01	0.09	0.00	0.00	0.03	0.06	0.02	0.00
Fe₂O₃	1.95	2.00	2.58	2.91	1.27	2.73	3.31	1.61	1.44	1.68
MgO	1.01	1.12	1.15	1.31	0.13	0.12	0.19	0.06	0.06	0.07
MnO	0.02	0.01	0.00	0.04	0.04	0.02	0.00	0.06	0.03	0.01
Cr₂O₃	0.02	0.05	0.06	0.00	0.04	0.01	0.03	0.00	0.00	0.00
Na₂O	13.75	13.49	13.33	13.08	14.58	14.41	14.29	14.46	14.53	14.49
K₂O	0.00	0.00	0.00	0.00	0.01	0.01	0.02	0.01	0.07	0.00
CaO	1.99	2.53	2.19	2.59	0.55	0.61	0.79	0.56	0.45	0.62
Total	99.44	99.40	98.70	99.11	99.44	99.53	99.86	99.56	99.59	99.36
Cation on 6 O basis										
Si	1.99	1.99	2.00	1.99	1.98	1.98	1.98	1.98	1.99	1.99
Al	0.01	0.01	0.00	0.01	0.02	0.02	0.02	0.02	0.01	0.01
Σ	2.00	2.00	2.00	2.00	2.00	2.00	2.00	2.00	2.00	2.00
Al	0.90	0.88	0.87	0.86	0.97	0.93	0.91	0.96	0.97	0.96
Ti	0.00	0.00	0.00	0.00	0.00	0.00	0.00	0.00	0.00	0.00
Fe	0.05	0.05	0.07	0.08	0.03	0.07	0.09	0.04	0.04	0.04
Mg	0.05	0.06	0.06	0.07	0.01	0.01	0.01	0.00	0.00	0.00
Mn	0.00	0.00	0.00	0.00	0.00	0.00	0.00	0.00	0.00	0.00
Cr	0.00	0.00	0.00	0.00	0.00	0.00	0.00	0.00	0.00	0.00
Na	0.91	0.90	0.89	0.87	0.96	0.95	0.95	0.95	0.96	0.96
K	0.00	0.00	0.00	0.00	0.00	0.00	0.00	0.00	0.00	0.00
Ca	0.07	0.09	0.08	0.10	0.02	0.02	0.03	0.02	0.02	0.02
Σ	1.99	1.98	1.98	1.97	2.00	2.00	1.99	1.99	1.99	1.99
Atomic percentages										
Na	87.49	85.40	84.78	82.34	94.65	90.52	88.29	93.66	94.54	93.29
Ca	7.41	9.37	8.32	9.86	2.04	2.30	2.98	2.11	1.67	2.31
Fe	5.10	5.22	6.89	7.79	3.31	7.18	8.73	4.23	3.80	4.41

Table 2: Selected jadeite analyses (all Fe as Fe³⁺).

Garnet analyses

	St12	St12	St12	St12	St12	St12	St12	CT183	CT183	CT183
SiO₂	36.86	36.96	37.47	36.79	36.66	36.43	37.00	38.11	38.04	37.46
Al₂O₃	20.85	20.91	20.78	21.12	20.99	21.12	21.05	21.19	21.36	21.22
TiO₂	0.09	0.11	0.10	0.10	0.10	0.12	0.11	0.06	0.07	0.09
FeO	32.98	32.71	28.86	33.16	32.96	32.95	31.48	27.09	27.44	28.20
MgO	0.90	0.91	0.50	0.90	0.92	0.90	0.77	1.51	1.37	1.34
MnO	1.62	1.59	2.19	1.61	1.56	1.57	1.65	1.13	1.20	1.23
CaO	6.86	6.95	8.87	6.49	6.99	6.77	8.09	11.76	11.98	11.10
Total	100.16	100.14	98.77	100.17	100.17	99.87	100.16	100.85	101.46	100.63
Cation on 24 O basis										
Si	5.96	5.97	6.05	5.94	5.93	5.91	5.96	6.00	5.97	5.95
Al	0.04	0.03	0.00	0.06	0.07	0.09	0.04	0.00	0.03	0.05
Σ	6.00	6.00	6.05	6.00	6.00	6.00	6.00	6.00	6.00	6.00
Al	3.93	3.95	3.96	3.97	3.93	3.95	3.95	3.94	3.92	3.92
Ti	0.01	0.01	0.01	0.01	0.01	0.01	0.01	0.01	0.01	0.01
Σ	3.94	3.96	3.97	3.98	3.94	3.96	3.97	3.95	3.94	3.93
Fe	4.40	4.38	3.87	4.46	4.40	4.43	4.21	3.57	3.60	3.74
Mg	0.22	0.22	0.12	0.22	0.22	0.22	0.19	0.35	0.32	0.32
Mn	0.22	0.22	0.30	0.22	0.21	0.22	0.23	0.15	0.16	0.17
Ca	1.19	1.20	1.54	1.12	1.21	1.18	1.40	1.98	2.01	1.89
Σ	6.03	6.02	5.82	6.02	6.04	6.04	6.01	6.06	6.09	6.11
Mol per cent end-members										
Almandine	73.01	72.77	66.42	74.07	72.77	73.34	69.95	58.92	59.08	61.24
Pyrope	3.60	3.63	2.06	3.62	3.67	3.59	3.08	5.84	5.24	5.17
Spessartine	3.67	3.62	5.14	3.65	3.54	3.58	3.75	2.48	2.62	2.71
Grossulare	19.71	19.97	26.38	18.66	20.03	19.49	23.22	32.76	33.05	30.88

Table 3: Selected garnet analyses (all Fe as Fe²⁺).

Acknowledgements

First of all I would like to thank Prof. Dr. Bernhard Stöckhert. His valuable discussions, stimulating ideas, positive thoughts, and motivation are very much appreciated. I am greatly indebted to Dr. Klaus Röller for instruction and help with the TEM. Many thanks are due to Dr. Johannes Duyster for advice with the EBSD measurements and for his readiness to help with crystallographic problems. Dr. Rolf Neuser is thanked for support at the SEM and the CL, Dr. Heinz-Jürgen Bernhardt and Walter Köhler-Schneitker for advice at the EMP, and Miriam Fischer for help with the FTIR-measurements. I am grateful to Dr. Stuart Thomson and Dr. Jeff Lawlis for kindly improving the English.

Work would not have been so pleasant if there were not many friends and colleagues from the "second floor", especially Annette Lenze, Maria del Carmen Martinez, K. Annett Mönicke, Miriam Fischer, Dorothee Dorner, Jens Orzol, Stuart Thomson, Nassima Atmaoui, Alberto Adriasola, and Jens Steffahn. Thanks to you all!

The German Research Foundation (DFG) is gratefully acknowledged for financial support within the scope of the Collaborative Research Centre 526 "Rheology of the Earth – from the upper crust into the subduction zone".

Curriculum vitae

Personal data

Date of birth	• 13 th of June 1970
Place of birth	• Südlohn, NRW, Germany
Nationality	• German

School

1976 - 1980	• Roncalli elementary school, Borken-Weseke
1980 - 1986	• Gymnasium Mariengarden, Borken-Burlo
1986 - 1989	• Gymnasium Remigianum, Borken

Study

10/89 - 07/90	• Elementary study of chemistry, University of Dortmund
10/90 - 12/92	• Elementary study of geology, Friedrich-Wilhelm-University Bonn
01/93 - 12/97	• Main study of geology, Ruhr-University Bochum
10/96	• Diploma mapping: "Grenzbereich zwischen Plattenkalk-Serie und Phyllit-Quarzit-Einheit, Kreta"
11/97	• Diploma thesis: "Intrusionsniveau und Metamorphose oligozäner Gänge in den Pfunderer Berge, Südtirol"
12/97	• Graduation as "Diplom-Geologin", Ruhr-University Bochum

Employment record

01/98 – 07/99	• Graduate assistant at the Ruhr-University Bochum
since 08/99	• Research assistant at the Ruhr-University Bochum